Safety Improvement Techniques for Electric Vehicle Powertrains

by

Tianhao Wu

B.Eng.

A thesis submitted in accordance with the requirements for the award of the degree of *Doctor of Philosophy* of the University of Liverpool

November 2019

I would like to dedicate this thesis to my supervisor and my parents

Declaration

I hereby declare that except where specific references are made to the work of others, the contents of this dissertation are original and have not been submitted in whole or in part for consideration of any other degrees, qualifications, or any other Universities. This dissertation is the result of my own work and includes parts which are the outcome of work done in collaboration with my team members.

Tianhao Wu

Nov. 2019

Acknowledgements

First and foremost, I would like to express my deepest gratitude to my main supervisor, Dr. Yihua Hu, for granting me the precious opportunity to further myself at the highest level. You have encouraged and helped me to progress academically from a fresh graduate to a professional researcher and a mature individual. I have learned so much from you both academically and personally. Thank you for the invaluable comments and advice on my research as well as my life and career. It is a great honour for me to be your PhD student, and I hope I have fulfilled your high expectations and faith through my achievements. Secondly, I would also like to thank my second supervisor Dr. Jiafeng Zhou, for the generous support and academic guidance you have provided me. I will always treasure your support, encouragement and guidance.

I would also like to take this opportunity and thank my parents, especially my mother. You have always been greatly supportive of me. Your continuous help and understanding have made my life full of love, and I am grateful for everything you have done. Additionally, I would like to express my appreciation to my girlfriend. I am very thankful to her for her patience, tolerance, company and warm love. I have to say without your help, I would not have made it this far. Special thanks are also paid to my brilliant and lovely colleagues and friends; in particular to Dr. Sen Song, Dr. Kai Ni, Zuyu Wu, Zhiyi Zhao, Dr. Xinhua Li, Lujia Xie, Sokol Kuka, Chao Gong and Yixuan Zhang for many fruitful discussions and enjoyable moments.

Last but not least, the support from the Electrical Engineering and Electronics Department of the University of Liverpool is gratefully acknowledged.

Table of Contents

Table of Contents ..... **v**
List of Figures ..... **viii**
List of Publications ..... **xiv**
Abstract ..... **xv**
Chapter 1 Introduction **1**
1.1 Motivation 1
1.2 Dissertation Outline 4
1.3 References 6
Chapter 2 Review of EV Categories, Electric Powertrain Components and Safety Issues **7**
2.1 EV Types 7
2.1.1 Battery Electric Vehicle, BEV 8
2.1.2 Hybrid Electric Vehicle, HEV 9
2.1.3 Plug-In Hybrid Electric Vehicle, HEV 13
2.2 Electric Powertrain Components 14
2.2.1 Power Battery 14
2.2.2 DC-DC Converter 18
2.2.3 DC-Bus Capacitor 20
2.2.4 DC-AC Inverter 21
2.2.5 Propulsion Motor 22
2.3 Safety Issues Considering Regulatory Activities 25
2.3.1 Safety in Normal-Use 26
2.3.2 Safety in Post-Crash 29
2.4 Summary 31
2.5 References 31
Chapter 3 Modular Tri-port Converter with Fault-Tolerance Capability for Switched Reluctance Motor based HEVs **38**
3.1 Introduction 38
3.2 Tri-port Converter and Operation Modes 40
3.2.1 Proposed Tri-port Converter 40
3.2.2 Working States of Proposed Converter 42
3.2.3 Battery Bank Charging 44

3.3 Control Strategy for the Proposed Tri-port Converter 44
3.3.1 Two-port Energy Flow Condition 44
3.3.2 Three-port Energy Control Strategy 46
3.4 Fault Tolerance Control with Proposed Multi-port Converter 47
3.4.1 Fault Diagnosis and Fault Tolerance 47
3.4.2 SRM Modelling Under Fault Tolerance Operation 49
3.5 Simulation and Experimental Verifications 52
3.6 Summary 64
3.7 References 64
Chapter 4 Analysis and Suppression Approaches of Uncontrolled Generation for PMSM based Battery EVs 66
4.1 Introduction 66
4.2 Modelling for UCG Analysis 68
4.2.1 Battery model 69
4.2.2 Dynamic IPM Model 69
4.2.3 Steady-state UCG Model Considering Machine 69
4.3 Analysis of UCG 73
4.3.1 Transient Process of UCG 73
4.3.2 Comparison Between Traditional and Novel Steady-State Model 76
4.3.3 Parameter Dependencies of UCG Performance 77
4.4 IPMSM Design/Optimization for UCG Suppression 80
4.4.1 Motor Parameter Optimization Strategy 80
4.4.2 Experimental Verifications 84
4.5 Summary 89
4.6 References 90
Chapter 5 Reliable DC-bus Capacitor Discharge Strategy for PMSM based Battery EVs 94
5.1 Introduction 94
5.2 Design of Position Observer based on SM Theory 96
5.2.1 Traditional Position Observer based on SM Theory 96
5.2.2 Improved SM Observer for Position Estimation 104
5.3 Reliable Winding-based Discharge Algorithm Using Position Estimated by Improved SM Observer 106
5.4 Simulation and Experimental Verifications 107
5.5 Summary 110
5.6 References 110
Chapter 6 High-Reliability Multi-Objective Model Predictive Control Strategy for PMSM based EVs 114

6.1 Introduction 114
6.2 Model for Multi-objective FCS-MPC 116
6.3 Multi-Objective FCS-MPC Algorithm 118
6.3.1 Implementation of Single-Objective FCS-MPC Method 118
6.3.2 Structure of Multi-Objective FCS-MPC Method 119
6.4 Verifications 121
6.4.1 Simulation Results 121
6.4.2 Experimental Results 123
6.5 Summary 126
6.6 References 126
Chapter 7 Conclusions and Future Work 129
7.1 Summary 129
7.2 Future Work 132

List of Figures

Fig. 1-1. Worldwide EV sales and market share between 2013 and 2018. ..... **2**

Fig. 1-2. Number of EVs in the future according to EV30@30 Scenario. **2**

Fig. 2-1. Basic configuration for BEVs. **9**

Fig. 2-2. Series hybrid for HEVs. **11**

Fig. 2-3. Parallel hybrid for HEVs. **12**

Fig. 2-4. Planetary gear unit. **12**

Fig. 2-5. Series-parallel hybrid drivetrain by using a planetary gear unit. **13**

Fig. 2-6. Specific energy of different power batteries. **17**

Fig. 2-7. Characteristic comparison of different power batteries. **17**

Fig. 2-8. Structure of unidirectional DC-DC converters. (a) Non-isolated converter. (b) Isolated converter. **18**

Fig. 2-9. Structure of bidirectional DC-DC converters. (a) Bidirectional Buck/Boost converters. (b) Bidirectional half-bridge converter. (c) Bidirectional Cuk converter. (d) Bidirectional SEPIC converter. **19**

Fig. 2-10. Structure of tri-port converter. **20**

Fig. 2-11. Capacitor in Toyota Prius. (a) Electrolytic capacitor in the first generation. (b) Film capacitor in the second generation. **21**

Fig. 3-1. Desired energy flow modes. **40**

Fig. 3-2. Proposed SRM driving topology. (a) Front-end tree-level converter. (b) Traditional asymmetrical half bridged. (c) Phase winding with a central tapped node. (d) Proposed multi-level and fault tolerance driving topology for SRM. **41**

Fig. 3-3. Modular structure of proposed converter. **42**

Fig. 3-4. Excitation working states. (a) State 1. (b) State 2. (c) State 3. ..... **42**

Fig. 3-5. Demagnetization working states. (a) Freewheeling. (b) Energy recycling. **43**

Fig. 3-6. Working states under standstill condition. (a) G-B state 1. (b) G-B state 2. ..... **43**

Fig. 3-7. Energy supply to generator working states. (a) B-G state 1. (b) B-G state 2. ..... **44**

Fig. 3-8. SRM control strategy under driving mode. **45**

Fig. 3-9. HEV standstill energy exchange control. (a) Control diagram for HEV standstill generator starting. (b) Control diagram for HEV standstill battery charging. **46**

Fig. 3-10. Control strategy for three-port (G-M-B) energy exchange. **46**

Fig. 3-11. Fault tolerance operation. (a) Left part open-circuit fault. (b) Left part fault tolerance under working state 1. (c) Left part fault tolerance working state 2. (d) Right part open-circuit fault. (e) Right part fault under working state 1. (f) Right part fault under working state 2. ..... **48**

Fig. 3-12. SRM control strategy under driving mode. **49**

Fig. 3-13. Simulation results in voltage-PWM control mode. (a) Normal. (b) Power source switching. (c) Open fault. (d) fault-tolerance. 54

Fig. 3-14. Simulation results in current regulation mode. (a) Normal. (b) Power source switching. (c) Open fault. (d) fault-tolerance. 56

Fig. 3-15. Experimental setup. 57

Fig. 3-16. Experimental results in voltage-PWM control mode. (a) Power source exchange. (b) Normal. (c) Open fault. (d) fault-tolerance. 59

Fig. 3-17. Experimental results in current regulation control mode. (a) Power source exchange. (b) Normal. (c) Open fault. (d) fault-tolerance. 61

Fig. 3-18. Experimental results under heavy load. (a) Voltage-PWM control mode. (b) CCC mode. 62

Fig. 3-19. Experiment results of fault-tolerant operation. (a) Acceleration. (b) High-speed operation. (c) Load increasing. 63

Fig. 3-20. Generator charging battery bank. 64

Fig. 4-1. (a) Schematic diagram of a typical EV drive system. (b) Schematic diagram of the drive system during UCG. 67

Fig. 4-2. (a) Electrical circuit model approximating the three-phase rectifier and voltage-source to a three-phase resistive. (b) Electrical circuit model approximating the three-phase rectifier and voltage-source to a battery model. 70

Fig. 4-3. Phasor diagram for an IPMSM operating as a generator. 71

Fig. 4-4. SVPWM in the first sector. 73

Fig. 4-5. Current loop composed of D4，T6，T2 and motor windings. 74

Fig. 4-6. Current loop composed of T_1，T_6，T_2 and motor windings. 75

Fig. 4-7. Current loop composed of T_1，T_2，D_3 and motor windings. 75

Fig. 4-8. DC-link voltage and current versus speed using traditional model. 77

Fig. 4-9. DC-link voltage and current versus speed using proposed model. 77

Fig. 4-10. DC-link current versus speed when *d*-, *q*-axis inductance is variable. 78

Fig. 4-11. DC-link current versus speed under different air-gap magnetic flux. 79

Fig. 4-12. DC-link current versus speed under different winding resistance. 79

Fig. 4-13. DC-link current versus speed under various battery resistances. 80

Fig. 4-14. Procedure for IPMSM redesign/optimization. 81

Fig. 4-15. (a) Type "—" permanent magnet rotor structure. (b) V-type permanent magnet rotor structure. 83

Fig. 4-16. Inductance matrix of the optimized IPMSM. 84

Fig. 4-17. Experimental test bench. 85

Fig. 4-18. Three-phase stator currents, DC-link current and voltage at the speed of 3500 rpm. 85

Fig. 4-19. Three-phase stator currents, DC-link current and voltage at the speed of 3300 rpm. 86

Fig. 4-20. Three-phase stator currents, DC-link current and voltage at the speed of 3000 rpm. 86

Fig. 4-21. Three-phase stator currents, DC-link current and voltage at the speed of 2600 rpm. 87

Fig. 4-22. Three-phase stator currents, DC-link current and voltage at the speed of 2200 rpm. 87

Fig. 4-23. Three-phase stator currents, DC-link current and voltage at the speed of 1900 rpm. 88

Fig. 4-24. Three-phase stator currents, DC-link current and voltage at the speed of 1600 rpm. 89

Fig. 4-25. DC-link current versus speed. 89

Fig. 5-1. Topology of EV PMSM drive system. 95

Fig. 5-2. PMSM model. (a) Model in the three-phase stationary axis reference frame. (b) Model in two-phase stationary reference frame. 97

Fig. 5-3. Physical IPMSM model considering magnetic field generated by permanent magnet in two-phase stationary reference frame. 99

Fig. 5-4. Properties of signum functions. 101

Fig. 5-5. Traditional SM observer structure. 104

Fig. 5-6. Improved SM observer structure. 106

Fig. 5-7. Block diagram of the reliable discharge method using estimated position information. 107

Fig. 5-8. Discharge characteristics of DC-bus capacitor voltage and machine speed. (a) Simulation results. (b) Experimental results. 109

Fig. 5-9. Discharge characteristics of *d*, *q*-axis currents. (a) Simulation results. (b) Experimental results. 109

Fig. 5-10. Experimental results of position estimated by the improved sliding mode controller during discharge process. 110

Fig. 6-1. Structure of an FCS-MPCC-based drive system. 116

Fig. 6-2. Structure of multi-objective FCS-MPC-based controller. 119

Fig. 6-3. Performance of the proposed multi-objective FCS-MPC algorithm. 122

Fig. 6-4. Experimental equipment. 124

Fig. 6-5. Experimental performance of the proposed multi-objective FCS-MPC algorithm. (a) Speed, d-axis current, q-axis current and torque. (b) Phase currents under no-load and load conditions at 100 rad/s. (c) Phase current under load condition at 200rad/s. (d) Phase current under no-load condition at 10 rad/s. 125

Acronyms

ICE	Internal Combustion Engine
EV	Electric Vehicle
HEV	Hybrid Electric Vehicle
CO_2	Carbon Oxide
$MtCO_2$	Million Tons of Carbon Oxide
UK	United Kingdom
PiCG	Plug-in Car Grant
IEA	International Energy Agency
SRM	Switched Reluctance Motor
PMSM	Permanent Magnet Synchronous Motor
IPMSM	Interior Permanent Magnet Synchronous Motor
UCG	Uncontrolled Generation
BEV	Battery electric vehicle
PHEV	Plug-in hybrid electric vehicle
UN	United Nations
M	Motor
SOC	State of charge
DC	DC current
AC	Alternating current
MOS	Metal oxide semiconductor

IGBT Insulated gate bipolar translator

PWM Pulse width modulation

SWPM Sine pulse width modulation

SVPWM Space vector pulse width modulation

BLDCM Brushless direct current motor

PM Permanent magnet

IM Induction motor

SPMSM Surface-mounted permanent magnet synchronous motor

ECWVTA European Community Whole Vehicle Type-Approval

ISO International Organisation for Standardisation

IEC International Electrotechnical Commission

IP Ingress protection

B Battery

G Generator

MOSFET Metal-Oxide -Semiconductor Field Effect Transistor

CCC Current chopping control

PI Proportional integral

UR Uncontrolled rectifier

CPSR Constant-power speed ratio

EMF Electromotive force

IPM Intelligent power module

SM Sliding mode

SMO Sliding mode observer

LPF	Low pass filter
FCS	Finite control set
MPC	Model predictive control
TCO	Targeting control objective
SVN	State variable normalization
DTC	Direct torque control
PMSG	Permanent magnet synchronous generator
MPSC	Model predictive speed control
MPPC	Model predictive power control
MPCC	Model predictive current control
MPTC	Model predictive torque control

List of Publications

First Author Publications

[1] **T. Wu**, W. Li, K. Ni, S. Song and M. Alkahtani, "Modular Tri-Port Converter for Switched Reluctance Motor based Hybrid Electrical Vehicles," in *IEEE Access*, vol. 7, pp. 15989-15998, 2019.

[2] **T. Wu**, W. Li, Y. Hu, C. Gong, S. Kuka and J. Lu, "Parameter Dependency Analysis of Uncontrolled Generation for IPMSMs in Electric Vehicles," *IECON 2018 - 44th Annual Conference of the IEEE Industrial Electronics Society, Lisbon, Portugal*, 2019. (Accepted).

[3] **T. Wu**, C. Gong, J. Gao and J. Lu, "A Winding-based DC-Bus Capacitor Discharge Strategy for PMSM Drive System in EVs Considering Position Sensor Fault," *IECON 2018 - 44th Annual Conference of the IEEE Industrial Electronics Society, Lisbon, Portugal*, 2019. (Accepted).

[4] Y. Han, C. Gong, Y. Hu, L. Yan, H. Wen, Y. Wang and **T. Wu**, "Multi-Objective Finite Control Set Model Predictive Control Using Novel Delay Compensation Technique for PMSM," *IEEE Transactions on Power Electronics*. (Major Revision)

Abstract

An increasing number of Electric Vehicles (EV) are playing an essential role in everyone's life. However, the relevant technologies are still not entirely mature. Notably, the EV safety issues are attracting significant attention from not only the scholars and manufacturers but also the occupants (drivers and passengers) and even the pedestrians. Because the EVs have to be powered by the rechargeable energy systems and propelled by the electricity-consuming power electronics and components, which usually have high voltage and large output power, the corresponding safety problems are very different from those in the conventional Internal Combustion Engine (ICE) vehicles. Important factors that need to be focused on include the electrical safety issues, such as electric shock, electrolyte leakage, reliable powertrain structure and components, high-reliability system control strategies and qualified post-fault and post-crash electrical protection measures, etc.

This thesis has analysed particular safety issues and demonstrated the handling strategies to improve the safety level of different types of EVs. Firstly, the relatively comprehensive review work on EV categories, powertrain components and safety problems considered in the international regulatory activities are completed, illustrating the reasons why EVs are not inherently safe and that there are different varieties of aspects that need to be investigated to ensure a higher EV safety level from the professional perspective. Then, aiming at both the Battery Electric Vehicles (BEV) and Hybrid Electric Vehicles (HEV), more reliable techniques are developed for not just normal working conditions but also post-fault and post-crash cases to improve the vehicle safety. In detail, firstly, tri-port converters characterized by fault-tolerance capability are designed for the Switched Reluctance Machine (SRM) based HEVs. Secondly, the Uncontrolled Generation (UCG) problems in the PMSM based BEVs are analysed, and an effective suppression method is proposed. Thirdly, a winding-based discharge method is innovatively studied to safely and quickly dissipate the residual energy stored in the power electronics after a Permanent Magnet Synchronous Machine (PMSM) based BEV crashes, which contributes to avoid electric shock in emergencies. Finally, aiming at the normally working PMSM based EVs (regardless of HEV and BEV), a novel model predictive control strategy endowed with simple implementation and optimal control procedures is developed to improve the reliability of the software part as well as the system control

performance.

Chapter 1 **Introduction**

1.1 Motivation

In comparison with the traditional gasoline internal combustion engine (ICE) vehicles, electric vehicles (EV) are endowed with numerous competitive advantages, including reducing emissions and being cost-effective. Specifically, pure electric cars have no tailpipe emissions, so they do not need any exhausts installed in the vehicle. As for the hybrid electric vehicles (HEVs), they have significantly lower average emissions than traditional petrol or diesel cars [1]. The statistics show that the EVs in operation worldwide avoided a total emission of 29.4 million tons of carbon oxide ($MtCO_2$) in 2017, significantly improving the air quality, particularly in urban areas and at roadsides with poorer air quality [2]. In terms of saving costs, firstly, electricity is cheaper than petrol or diesel. On a cost per mile basis, a pure EV could cost a third (or less) of what a traditional petrol or diesel car might cost, and as for HEV, it can efficiently combine an electric motor better with an ICE, thereby, reducing the use of fossil fuels. Secondly, the maintenance costs are lower. The propulsion system of a traditional vehicle is usually complex, which contains many components, including exhaust systems, starter motors, fuel injection systems, oil, radiators and gears, etc. While pure EVs solely has three main components — the battery, inverter and motor. Consequently, there are fewer parts requiring maintenance and the servicing is simpler. Finally, governments are actively encouraging drivers to switch to electric cars and vans. The UK Plug-in Car Grant (PiCG) provides a discount of up to £3,500 for eligible electric vehicles and up to £8,000 for vans. This initiative can represent enormous savings for the customers.

Due to these merits, the EV market has experienced exponential growth worldwide. Fig.1-1 illustrates global EV sales and market share between 2013 and 2018 [2]. Also, the EVs will account for a much higher share in the near future. According to “the Global EV Outlook 2018” released by the International Energy Agency (IEA), the number of EVs worldwide reached 3.1 million in 2017, and it will increase by around seventy-five times by 2030 in the EV30@30 Scenario (as in Fig.1-2) [2]. More and more EVs will inevitably flood into our daily lives,

which is drawing considerable attention of not only the manufacturers but also the engineers and scholars.

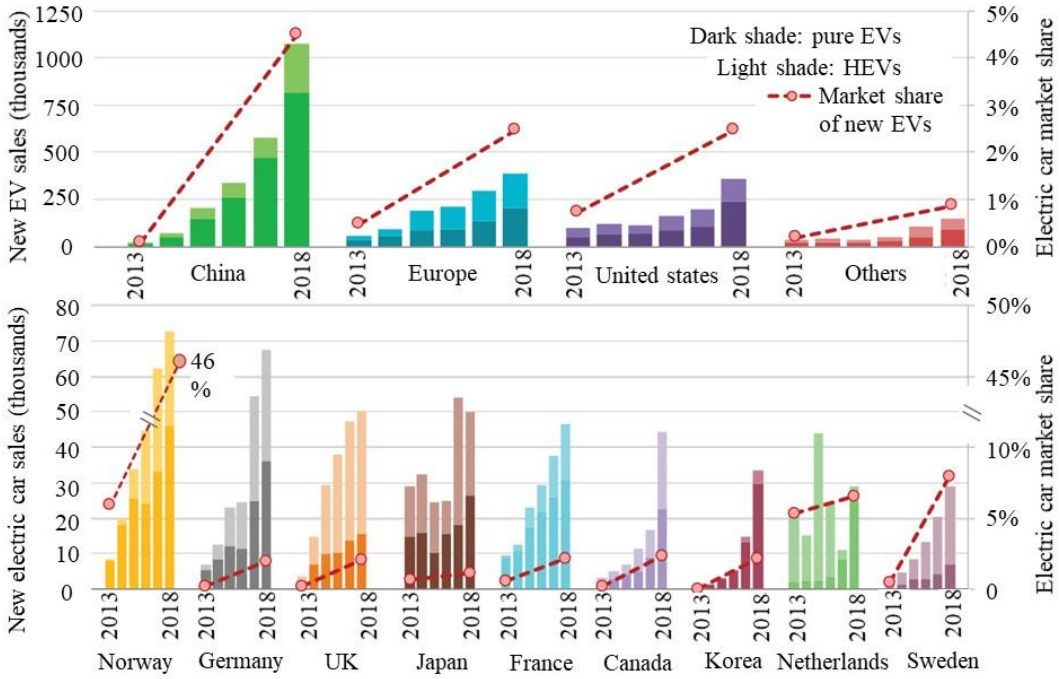

Fig. 1-1. Worldwide EV sales and market share between 2013 and 2018[2].

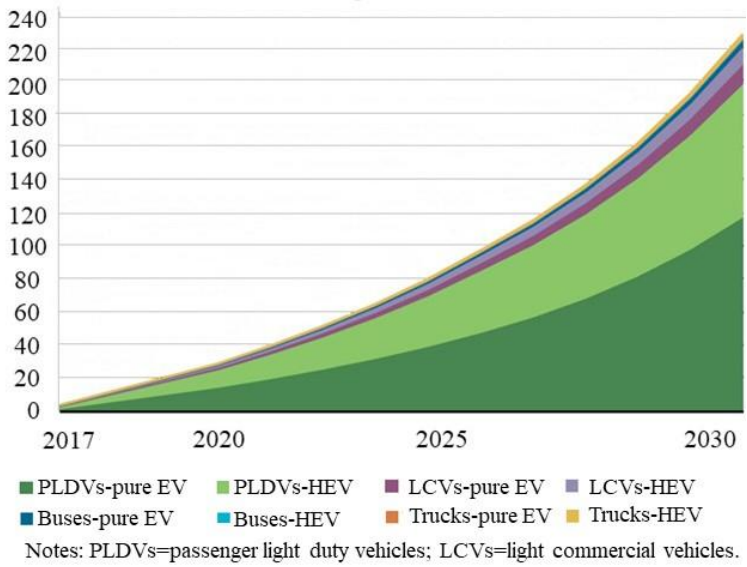

Fig. 1-2. Number of EVs in the future according to EV30@30 Scenario[2].

Since EVs are regarded as the future direction of the automotive industry, it is of great importance to investigate the relevant technologies that are capable of improving the safety and

qualities and performance of the cars, which will further promote the development and the usage of EVs. Recently, it has been reported that a Tesla Model S crashed and caught fire in Florida, USA, killing two teenagers [3]. Additionally, in October 2018 an EV driver on the motorway in China [4] died as a result of being crushed from behind by a lorry following a power shortage. Hundreds of similar accidents reported in recent years arouse the extensive concern of the public on the problem of EV safety. Currently, parts of the hot topics concerning EV safety reflect in their powertrains in the field of electrical engineering, including the reliable energy sources, converters and inverters, electrical machines, high-performance and high-reliability control algorithms, and so on [4]. Although various mature technologies have been widely put into practice in these aspects, the scholars and engineers never stop developing superior alternatives or brand-new techniques to improve the safety level as well as the intrinsic properties of the EVs. On these ground the author aims to conduct a relatively all-sided study on the safety issues in EV powertrains. In allusion to several vital challenges (new converter topology, safety issues and reliable machine control schemes) in typical EV drive trains that are based on particular machines, the author has innovatively developed corresponding solutions, contributing to improving the EV safety level, enriching the powertrain design theory and providing state-of-the-art techniques for engineering applications.

The target of this work is to overcome four problems that are previously seldom considered in EV powertrains, which are as follows:

i. To develop a **converter with the characteristics of tri-port and modular structure characterized by high reliability** to simultaneously combine the generator, battery and motor in one converter for HEVs. In the switched reluctance machine (SRM)-based HEVs, the traditional converters are with dual ports, so they cannot support all the system operating modes. Comparatively speaking, the new converter keeps multiple functions and it can ensure that the energy flow in the system can be flexibly controlled. Moreover, the proposed converter has strong fault tolerance capacity, which can block the fault point to achieve fault tolerance operation so as to improve the system safety and reliability level.
ii. To analyse **the uncontrolled generation (UCG) challenge that exists in the PMSM-based battery EVs and the parameter dependencies of this phenomenon**, paving the way for designing machines to enhance the powertrain safety. UCG occurs when

the IPMSM is controlled by the flux-weakening algorithms to operate over the corner speed, generating high charging current that flows back to the battery. This poses potential threats to the health and life of those electrical components. By analysing the relationship between the UCG performance characteristics and the internal parameters of the systems, the author can obtain the proper parameters that can suppress the charge current during UCG. This will provide guidelines for machine design.

iii. To develop a **winding-based DC-bus capacitor discharge strategy for PMSM-based EVs considering position sensor fault**, which can quickly and safely dissipate the residual energy stored in the electrical components after emergencies. The traditional energy dissipation method after EV crash is to employ external circuits composed of a power resistor and a switch, which will sacrifice the weight and size of the powertrain. Comparatively, the new strategy only relies on the existing components in the system. Moreover, the proposed method has the position sensor fault tolerance ability, promoting the reliability of the new scheme.

iv. To develop a **simple multi-objective finite control set model predictive control (FCS-MPC) strategy for PMSM-based EVs** to achieve high-performance motor speed and current control. By creating a new cost function, the steady-state speed and current ripples can be significantly reduced. Meanwhile, the speed and torque dynamics of the system are marked. This new control scheme is specially designed and well-suited for EVs that placed great demand on the control performance. Since the new algorithm is easy to implement, avoiding redundant executions, the system reliability can be improved so the safety of the powertrain can be enhanced to a reasonable extent.

1.2 Dissertation Outline

This work focusses on comprehensively and innovatively solving the urgent problems in different EV powertrains. The dissertation consists of seven chapters. An outline of the structure is organized organised as follows:

Chapter 1 introduces the motivation of this study and the challenges that need to be solved in this manuscript. Besides, the objectives and the brief introduction of the research contents are illustrated.

Chapter 2 comprehensively reviews the classifications of EVs, components of electric powertrains and safety issues concerning international standards. It aims to point out that there are a variety of EV systems that have different powertrain structures and compositions and each of them deserves in-depth investigation. Moreover, the regulatory activities can provide guidelines for the future researches about EV safety improvement.

Chapter 3 discusses the tri-port converter that has a modular and concise structure, which meets the requirements for HEV applications. Firstly, the topology of the new converter is explained. Then, the functions of the converter are detailed according to the powertrain working modes, and simultaneously, the corresponding control strategies are developed to cooperate with the different working modes. Finally, the fault tolerance characteristics of the tri-port converter are investigated to expand its feasibility under the harsh HEV application conditions.

Chapter 4 shows the mechanism, parameter dependency analysis results and attenuation method of UCG for interior permanent magnet synchronous machines (IPMSM) in BEVs. Firstly, an accurate steady-state model for UCG analysis is established. Then, the peak current which depends on the machine parameters, the instantaneous speed and dc-link voltage are discussed for better understanding of the UCG process. It is worth mentioning that this research considers many system parameters, such as *d*, *q*-axis inductance, stator resistances, permanent magnet flux linkage and battery internal resistance.

Chapter 5 introduces the winding-based capacitor discharge strategy to quickly and safely dissipate the bus capacitor voltage for a PMSM based BEV powertrain. By applying nonzero *d*, *q*-axis currents to the machine, the capacitor voltage can be regulated to remain under the safe level during the whole bleeding process. In order to endow the discharge strategy with position sensor fault tolerance ability, an improved position observer based on the SM theory is constructed at first.

Chapter 6 discusses the new FCS-MPC strategy that simultaneously evaluates two targeting control objectives including speed and currents in a single cost function, achieving high-performance single-closed-loop control structure for EVs (regardless of the EV types). As the FCS-MPC method is simple to implement, and it is realized according to the optimal control principle, the reliability and safety of the EV drive trains can be prompted.

Chapter 7 draws a summary of the main contributions of this dissertation It also provides suggestions for future research areas.

1.3 References

[1] Hooftman, N., Oliveira, L., Messagie, M., Coosemans, T. and Van Mierlo, J. "Environmental Analysis of Petrol, Diesel and Electric Passenger Cars in a Belgian Urban Setting," *Energies*, vol. 9, no. 2, pp. 84-108, 2016.

[2] "Global EV Outlook 2018," in Towards cross-modal electrification, International Energy Agency, 2018.

[3] R. Ferries. NTSB opens an investigation into Tesla crash in Florida. 2018. Available: https://www.cnbc.com/2018/05/09/two-florida-teenagers-killed-in-tesla-crash.html.

[4] Electric car gets crashed with the driver killed. Available: https://news.china.com/news100/11038989/20181002/34064308_all.html.

[5] Un-Noor, F., Padmanaban, S., Mihet-Popa, L., Mollah, M.N., Hossain, E., "A Comprehensive Study of Key Electric Vehicle (EV) Components, Technologies, Challenges, Impacts, and Future Direction of Development," *Energies,* vol. 10, no. 8, pp. 1217-1299, 2017.

Chapter 2 Review of EV Categories, Electric Powertrain Components and Safety Issues

In terms of EVs, they can be divided into three major categories on the basis of their powertrain composition and structure: battery electric vehicle (BEV), HEV and plug-in hybrid electric vehicle (PHEV). The whole thesis aims to comprehensively develop novel and effective safety improvement technologies for both the BEV and HEV powertrains. Before introducing the research problems and the relevant solutions in details, this chapter will firstly give a comprehensive review about the EV categories, powertrain structure and composition, pointing out that the varieties of different EV systems that are currently in service. As a result, the review indicates that it is crucial to conduct in-depth and further investigation for any types of EVs due to their popularity. Secondly, by analysing the powertrain components of EVs, various high-voltage and high-power power electronics and energy storage devices can be found in an EV powertrain, posing particular risks distinctive from those for a traditional gasoline ICE vehicle. In this chapter, the potential risks for EVs according to the United Nations (UN) Regulations are introduced. The review validates the research topics about EV safety problems introduced in the rest of the chapters fully comply with the international standards and the appropriate and valuable.

2.1 EV Types

According to the International Electrotechnical Commission's Technical Committee 69 (Electric Road Vehicles), the vehicles that only use battery as the energy source are BEVs [1-3], while the vehicles that use two or more types of energy source, storage or converter are named after HEVs, as long as at least one of those together with battery provides electrical energy [4]. HEVs are a broad family due to the various possible combinations such as ICE and battery [5], battery and capacitor [6], battery and fuel cell [7], battery and compressed air energy storage [8], etc. Recently, both ordinary consumers and specialists have started referring to the vehicles with an ICE and electric motor as combination HEVs, the battery and capacitor

combination ones as ultra-capacitor-assisted EVs, and those with battery and fuel cell combination as fuel-cell-assisted EVs [9]. As researching the structure and features of EVs are the main objectives of this research, therefore, those vehicles with different power sources are collectively referred to as HEVs. Moreover, considering the differences in the charging systems, the PHEV will be discussed individually. In summary, this chapter will categorize the EVs as the following: 1) battery electric vehicle, BEV, 2) hybrid electric vehicle, HEV and 3) plug-in hybrid electric vehicle, PHEV.

2.1.1 Battery Electric Vehicle, BEV

BEV is also commonly known as pure EV (PEV), which denotes only-electric vehicles or all-electric vehicles. It is a type of electric vehicle (EV) that uses chemical energy stored in battery packs. BEVs use electric motors and motor controllers instead of ICEs for propulsion. They derive all power from battery packs and thus possess no ICEs, fuel cell, capacitor or fuel tank. Nowadays, BEVs are becoming more and more attractive considering the higher oil prices and the advancement of new battery technology (lithium-ion battery) offering higher power and energy density. Because the BEVs are vehicles only utilise charged on-board batteries for propulsion, the running distance of such vehicles mainly depends on the battery capacity. Thanks to the lithium-ion battery packs carry an energy density of 0.9–2.63 MJ/L (2.5 to 7.3 times higher than the old lead-acid batteries), typical BEVs are able to cover 100 km-250 km on a single charge [10]. However, some advanced vehicles can last much further, from 300 km to 500 km. Table 2-1 list eight models and their nominal top running distance. Notably, if comparing the BEVs to the gasoline-based cars, there is still a large room for BEVs to advance. The traditional gasoline ICE vehicles can easily cover 300 km-700 km, benefiting from the higher energy density of the petroleum-based fuels (gasoline having an energy density of 34.2 MJ/L, 38 to 13 times higher than the state-of-art batteries). Another defect of pure EVs is that when the energy stored in the battery packs is depleted, the charging time will significantly increase compared to refuelling a conventional ICE vehicle. The charging time can be up to 36 hours to completely replenish the batteries [11-12]. Indeed, there also exist BEVs that take far less time (charging 80 percent within nearly half an hour) to recharge the batteries once the rapid chargers are employed [13], but none is comparable to the insignificant time required to refill a fuel tank. The charging time depends on the charger configuration, its infrastructure and

operating power level.

TABLE 2-1
Typical BEVs

Models	Top electricity-powered cruising range (km)	Models	Top electricity-powered cruising range (km)
Tesla Model 3	350	Tesla X	565
BMW i3	345	Toyota Rav4	160
Chevy Bolt	322	Tesla Model S	530
Nissan LEAF	311		

The advantages of BEVs lay in their simple construction, operation and convenience. The BEVs produce no greenhouse gas and create no noise, being hugely environmentally friendly. Moreover, electric propulsion can provide instant and high torques, even at low speeds. These make the BEVs one of the ideal means of transportation in urban areas.

Figure 2-1 shows the basic configuration for BEVs: the wheels are driven by electric machines which are powered by the battery pack (B) through power inverter circuits.

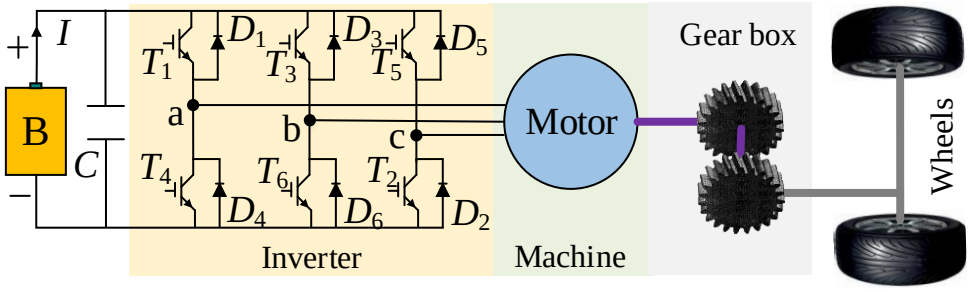

Fig. 2-1. Basic configuration for BEVs.

2.1.2 Hybrid Electric Vehicle, HEV

This part will exemplify the best-known HEVs that combine a conventional ICE system with an electric propulsion system to discuss their features and structure. The presence of the electric powertrain is intended to achieve a better fuel economy than better performance in conventional vehicles. The modern HEVs aim to make full use of efficiency-improving technologies such as regenerative brakes which convert vehicles' kinetic energy to electric

energy to store in a battery or supercapacitor. Varieties of HEVs use an ICE to turn an electrical generator, which either recharges the batteries of vehicles or directly powers its electric drive motors. Many HEVs reduce idle emission by shutting down the engine at idle and restarting it when needed, known as the start-stop system. A hybrid-electric system produces less tailpipe emission than a comparably sized gasoline car, since the hybrid gasoline engine is usually smaller than that of a gasoline-powered vehicle. If the engine is not used to drive the car directly, it can be geared to run at the maximum efficiency, further improving fuel economy. According to the above analysis, HEVs are primarily ICE driven cars that use an electric drive train to improve mileage or to enhance performance. Table 2-2 illustrates eight typical HEV models and their maximum electricity-powered cruising range. It can be noted that once gasoline is running out, the battery energy is capable of propelling the car to operate as normal in the next dozens of kilometres.

TABLE 2-2
Typical HEVs

Models	Top electricity-powered cruising range (km)	Models	Top electricity-powered cruising range (km)
Chevy Volt	85	Volvo XC90 T8	50
BMW i8	55	Toyota Prius	40
BMW 330e	60	Kia Optima	46
Audi A3 E-Tron	50	Hyundai Sonata	45

There are three commonly used HEV configurations [14-18], namely, 1) series hybrid, 2) parallel hybrid and series-parallel hybrid.

1) Series hybrid

Fig.2-2 depicts the structure of the series hybrid as the simplest for forming an HEV. In this configuration, only the electric motor drives the drivetrain, and an ICE works as a generator to power the electric motor or to recharge the batteries. At this stage, the vehicle can be regarded as a BEV that is assisted by an ICE generator. Therefore, the series hybrids have a larger battery pack than the parallel hybrids. There are numerous advantages of this configuration. Firstly, when the battery state of charge (SOC) is low, the engine can generate power at its optimum settings at all times and then charge the battery, making the use of gasoline more efficient (ICE

always works at the maximum working efficiency). Secondly, because the wheels are propelled by the electric drivetrain, the response speed is fast.

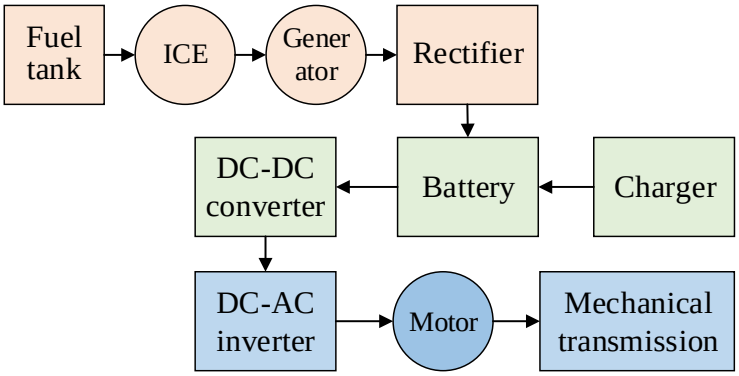

Fig. 2-2. Series hybrid for HEVs.

2) Parallel hybrid

Fig.2-3 illustrates the structure of the series hybrid. In this configuration, the ICE and the electric motor are both connected to the mechanical transmission to drive the wheels. Either one of them or both of them can transmit power. In this case, the vehicle can be considered as an ICE-based system with electric assistance. Before the year of 2013, the commercialized parallel hybrids usually adopt full-power combustion engines and low-capacity electric machines (<20 kW) together with small battery packs [14]. After 2015, the parallel hybrids with over 50 kW electric powertrain are available, enabling electric driving at moderate acceleration. The parallel hybrids are more efficient than those comparable non-hybrid vehicles especially during urban stop-and-go conditions where the electric motor is expected to contribute and during highway operations. Usually, ICE in this type of configuration can also serve as a generator to recharge the battery packs when it produces more power than the energy required for driving. However, it needs to be mentioned that the control process and algorithms of the parallel hybrids are more difficult than the series ones, though they are endowed with more flexibility.

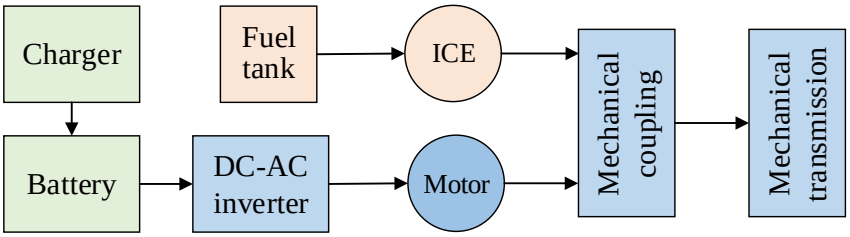

Fig. 2-3. Parallel hybrid for HEVs.

3) Series-parallel hybrid

Series-parallel drivetrains merge the advantages and complications of the parallel and series drivetrains. Paper [19] points out that this type of configuration is achieved by relying on the presence of a planetary gear unit (as in Fig.2-4). Fig.2-5 shows the structure of the series-parallel hybrid based on the planetary gear. As shown in the figure, the sun gear is connected to a generator; the ICE is coupled to the planetary gear by the use of the planetary carrier; the output shaft of the traction motor and the massive ring gear are connected to the gearbox to provide propelling force with clutches.

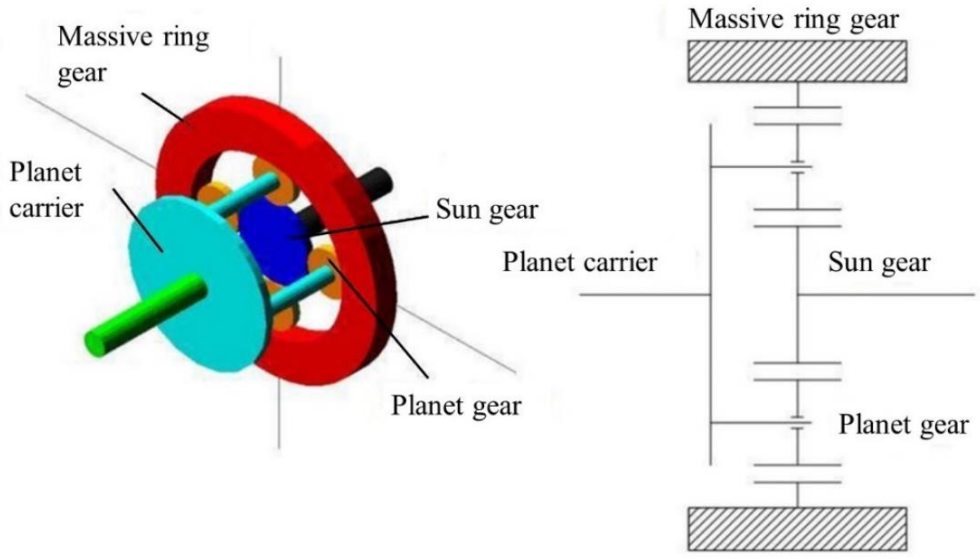

Fig. 2-4. Planetary gear unit[19].

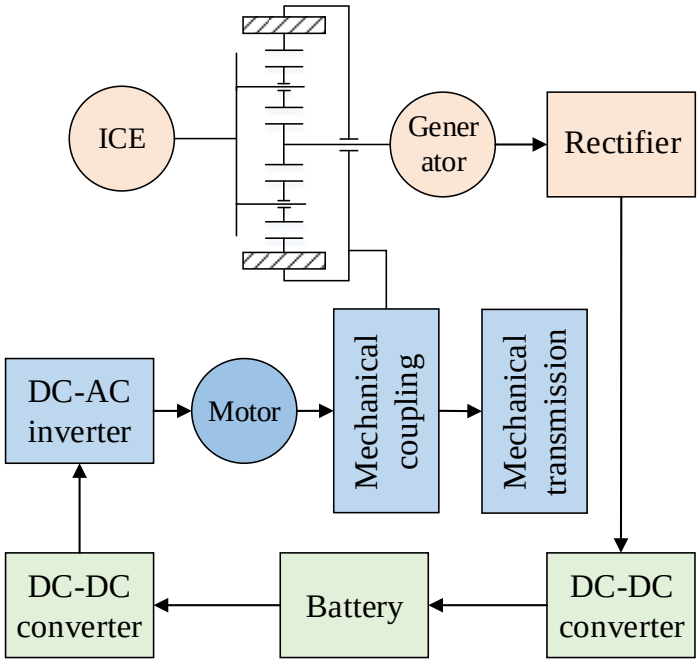

Fig. 2-5. Series-parallel hybrid drivetrain by using a planetary gear unit.

By combining the series hybrid and parallel hybrid, the engine can both drive the wheels directly (as in the parallel drivetrain) and be effectively disconnected, with only the electric motor providing power (as in the series drivetrain). With gas-only and electric-only options, the engine can operate at near-optimum efficiency in more scenarios. At lower speeds, it operates more like a series vehicle. While at high speeds, where the series drivetrain is less efficient, the engine takes over and the energy loss is minimized. This system incurs higher costs than a pure parallel hybrid since it requires a generator, a larger battery pack, and more computing power to control the dual system. Nevertheless, its efficiencies mean that the series-parallel drivetrain can perform better and use less fuel than either the series or parallel systems alone.

2.1.3 Plug-In Hybrid Electric Vehicle, HEV

The concept of PHEV appears to extend the range of HEVs [20–25]. As the name suggests, it is an HEV whose battery can be recharged by plugging into an external source of electric power as well as by its on-board engine and generator. Unlike HEVs, PHEVs usually possess the ability to run solely on battery power, gas, or a combination of both, resulting in a higher

requirement of battery capacity than HEVs [14]. PHEVs can charge their batteries directly from the grid (HEVs cannot), and they also have the facility to utilize regenerative braking. Charging the battery from the grid can cost less than using the on-board engine, helping to reduce operating costs. Moreover, because PHEVs can run by only using electricity for most of the time, they consume less fuel and thus reduce the corresponding cost and greenhouse gas emission.

2.2 Electric Powertrain Components

As shown in Fig.2-1 and Fig.2-2, the principal electric powertrain components in an EV include the following five parts: 1) Battery pack that supplies power to the whole system; 2) DC-bus capacitor which can smoothen the bus voltage and suppress the voltage surge; 3) DC-AC inverter that converts the DC voltage to the AC one; 4) Traction motor that provides the driving force; 5) DC-DC converter that converts low battery voltage to high. It needs to be mentioned that the former four components are mandatory for any EVs while the DC-DC converter might not be employed in some vehicle models when the battery is able to provide a sufficiently high voltage. This part will introduce these powertrain components at length.

2.2.1 Power Battery

The power batteries used in EVs are different from the conventional ones, which must meet the following requirements [26-30]: firstly, the discharge time is extended when the discharge current stands at the medium position; secondly, the maximum allowable discharge current is supposed to be high considering the vehicle starting and accelerating status. Further, in order to increase the safety level and simultaneously reduce the cost of EVs, the power batteries should generally own the following characteristics: high specific energy; great specific power; long working life; adequate uniformity, high reliability; high temperature performance; excellent environmental adaptability; low self-discharge rate; environmentally friendly; low price. Unluckily, although the battery technologies have been developed significantly, time and efforts are still needed before creating the perfect power batteries that meet all the above requirements. Nowadays, the commercially used batteries mainly include the lead-acid battery, the nickel-metal-hydride and the lithium-ion battery.

1) Lead-acid battery

Lead-acid batteries are currently the most widely used batteries in the automotive field [31-32], which are mainly used as a power source for various electrical and electronic equipment inside the ICE vehicles. The lead-acid battery was invented in 1859 by the French chemist Gaston Plante. Now, the lead-acid batteries used in vehicles generally adopt lead dioxide and sponge-like lead as the cathode and the anode, respectively, and the electrolyte is dilute sulfuric acid solution. Because this type of battery is reliable and cost-effective, they have been widely used at the early stage of EVs. Even now, the lead-acid batteries are prevalent in some tourist cars, electric forklifts and short-distance buses. However, lead-acid batteries have several crucial shortcomings, such as heavy mass, poor overcharge and discharge performance and high self-discharge rate.

Due to the above defects, both scholars and companies have turned their attentions to other types of power batteries. They believe that the lead-acid batteries will gradually withdraw from the EV market. However, it turns out that the vitality of lead-acid batteries is still strong. For example, many hybrid models such as Wuzhou Long Automobile and Anyuanke and Ankai are still using lead-acid batteries. Because the technologies related to the lead-acid batteries are relatively mature, they will not disappear shortly and the improved ones will also be competitive.

2) Nickel metal-hydride battery

Nickel metal-hydride battery is a member of the alkaline batteries which are composed of the nickel base and alkaline solution electrolytes [33]. Nickel metal-hydride battery is developed in the 1990s. The negative electrodes of the battery cells use the hydride electrode, and the positive electrodes adopt nickel hydroxide. Besides, the electrolyte is the aqueous potassium hydroxide solution. The potential advantages of the battery include high operating voltage, high specific energy and specific power, adequate overcharge and discharge capacity, etc. Compared with lead-acid batteries, the nickel-metal-hydride type offers much higher specific energy without pollution to the environment. Consequently, many commercial HEVs have adopted them as the power source.

Currently, the nickel-metal-hydride battery usually serves as auxiliary power in most of the

hybrid vehicles on the market. The reasons why the application cannot get wider is that the capacity of them will drop significantly at low-temperature conditions and the self-discharge rate is high. In addition, the price of the nickel-metal-hydride battery is relatively high. This happens because the raw materials such as nickel metal are expensive. In terms of the battery technologies, although the nickel-metal-hydride battery is able to store more energy than the lead-acid battery, it is easier to suffer from the permanent damage caused by the over-charge or over-discharge. This leads to the state of charge (SOC) of the battery must be limited within a small range to protect the battery, and most of the energy stored in the battery cannot be sufficiently used. For example, Toyota Prius can only use 20% of the energy stored in the nickel-metal-hydride battery.

3) Lithium-ion battery

Lithium-ion batteries with the characteristics of high capacity are developed in the 1990s [34-36]. The traditional structures for lithium-ion batteries include the graphite cathodes, lithium ion-based anodes and the electrolytic solution (lithium salt solution in which organic solvent is dissolved). The lithium-ion can be freely diffused in the crystal lattice of the positive and negative anode materials. When a battery is charged, lithium ions are taken out from the positive electrode and embedded in the negative electrode, and vice versa. Therefore, during the charge and discharge cycle of the battery, lithium ions reciprocate between the two electrodes of the battery to transfer electric energy through the electrolyte.

As a new type of chemical power source, lithium-ion batteries have the following outstanding advantages: 1) The operating voltage of single cells is high, so the consistency requirements when the cells constitute a battery pack are lower than those of the lead-acid batteries and hydrogen nickel batteries, leading to improved service life. 2) The specific energy is more substantial (as in Fig.2-6), which contributes to decreasing the vehicle mass while increasing the cruising mileage on one charge. 3) The battery volume is smaller under the same capacity, which significantly increases the application range. 4)The cycle life is extended, up to 2~3 times higher than that of lead-acid batteries. 5) The self-discharge rate is low, which is less than 5% within a month. 6) Lithium-ion batteries have the advantages of wide voltage range, no memory effect, and environmental friendliness. Consequently, lithium-ion batteries are recognized as the most promising EV power battery.

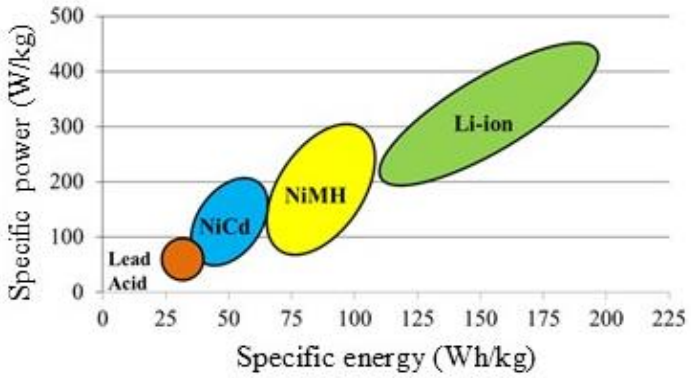

Fig. 2-6. Specific energy of different power batteries[35].

Fig.2-7 comprehensively compares the characteristics of different batteries [37]. As illustrated from the figure, apart from higher specific energy, the lithium-ion batteries have the property of higher specific power. Therefore, they are highly suitable for present-day EVs regardless of the HEVs that require high-power batteries, PHEVs that need both high-energy and high-power batteries, or the BEVs that places a high demand on the high-energy batteries. Thus, the lithium-ion battery technologies are attracting increasing attention recently, and an increasing number of manufacturers use lithium batteries as the power batteries for EVs.

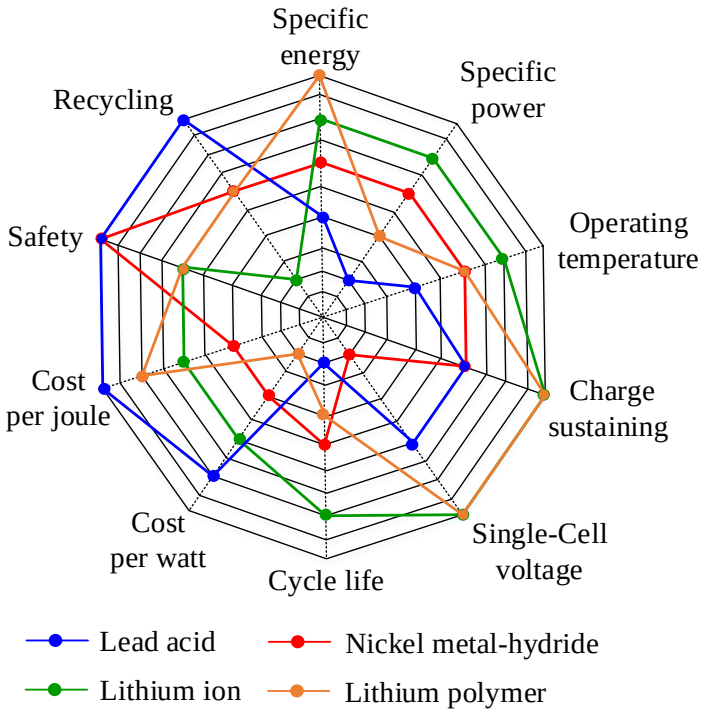

Fig. 2-7. Characteristic comparison of different power batteries[37].

2.2.2 DC-DC Converter

When the output voltage of the battery pack is high and it can satisfy the requirement of machine propulsion, as is shown in Fig.2-1 and Fig.2-3, DC-DC converters are not necessarily needed. But as in Fig.2-2 and Fig.2-5, when the battery voltage is less than the required level or the battery needs to be charged by a generator (either regenerative braking or ICE-based charging), the DC-DC converters must be adopted in these EV powertrains. In terms of the functions of the DC-DC converters in EVs, the commonly used converters can be classified into three types, namely, unidirectional converter, bidirectional converter and tri-port converter [38-42]. The structures of these converters are discussed as follows.

1) Unidirectional converter

A unidirectional converter is usually adopted to convert the low battery voltage to the high bus voltage, and the energy cannot flow back from the bus side to the battery side even in the braking conditions. According to whether there exist electrical isolation parts between the input and the output ports, the unidirectional DC-DC converter can be divided into two categories: non-isolated DC-DC converter without electrical isolation, and isolated DC-DC converter with electrical isolation. The basic non-isolated boost DC-DC converter is shown in Fig.2-8 (a), and the isolated half-bridge converter structure is comparatively illustrated in Fig.2-8 (b).

(a) (b)

Fig. 2-8. Structure of unidirectional DC-DC converters. (a) Non-isolated converter. (b) Isolated converter.

The differences between the two topologies are as follows:

1) The structure of the isolated converter is much more complicated. In Fig.2-8 (b), more power electronics including a transformer, two transistors, three capacitors and four diodes are adopted.

2) In order to reduce the volume of the isolated DC-DC converter as much as possible, the transformer needs to operate at the high-frequency situations, so the high-frequency properties of the power devices (transistors) in Fig.2-8 (b) should be good. Hence, Metal Oxide Semiconductor (MOS) is the best choice. Comparatively speaking, Insulated Gate Bipolar Translator (IGBT) which is suitable for higher-power situations can be used in Fig.2-8 (a).

2) Bidirectional converter

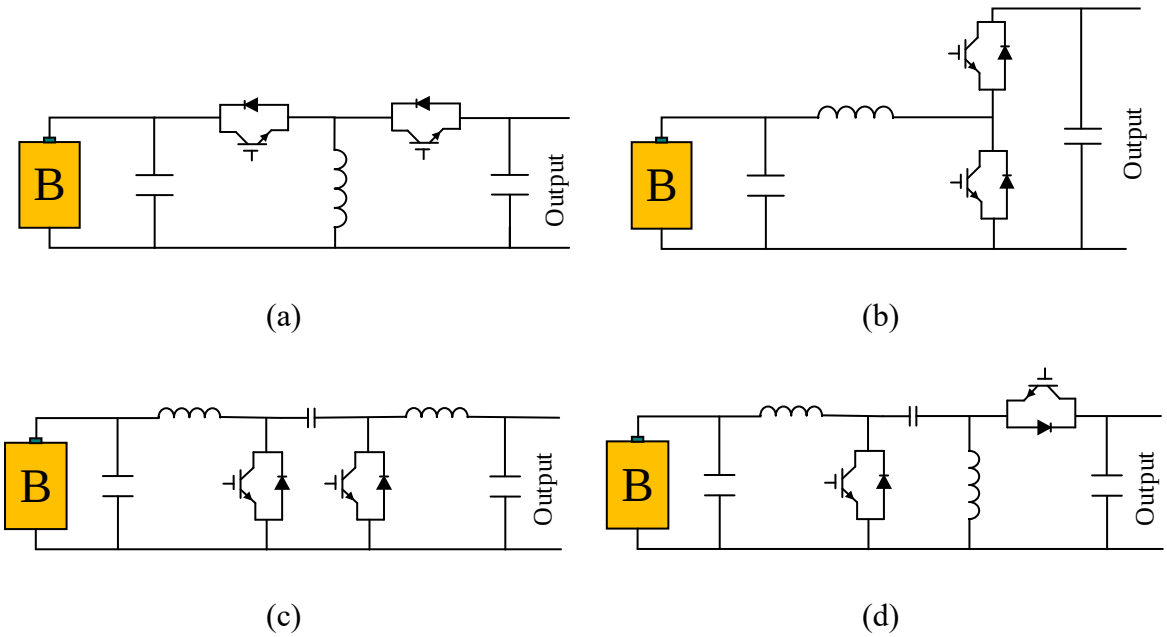

Fig. 2-9. Structure of bidirectional DC-DC converters. (a) Bidirectional Buck/Boost converters. (b) Bidirectional half-bridge converter. (c) Bidirectional Cuk converter. (d) Bidirectional SEPIC converter.

In comparison with the unidirectional converter, a bidirectional converter can not only transfer the low battery voltage to the high bus voltage but also allow the energy flow back to the battery packs. This kind of converter has been widely used for regenerative braking operations when the traction motor also serves as a generator in the braking states. The topologies of the bidirectional DC-DC converters are developed based on the unidirectional DC-DC converter. Specifically, the bidirectional DC/DC converters are achieved by adding more transistors and diodes into the unidirectional circuits (as in Fig.2-9). The structure in Fig.2-9 (a) is the basic bidirectional Buck/Boost converters. Fig.2-9 (b) is a bidirectional half-bridge converter. The

bidirectional Cuk converter and SEPIC converter are demonstrated in Fig2-9 (c) and Fig.2-9 (d), respectively. Because these four non-isolated circuit topologies are simple compared to the isolated converter topologies, they are inclined to satisfy the requirements of small volume and low cost.

3) Tri-port converter

Tri-port converters are proposed only for HEVs or PHEVs, in which apart from the battery pack and traction motor, a generator should also be employed to generate power and charge the battery (as in Fig.2-2). The topology of a tri-port converter is shown in Fig.2-10. The purpose of developing such a converter is to achieve flexible energy flow among the battery, generator and traction motor by using one single converter (detailed in Chapter III). Definitely, the functions of a tri-port converter can be realised by using more than one unidirectional and bidirectional DC-DC converters. But the advent of the tri-port converter can significantly reduce the volume and cost of powertrain devices. Moreover, the tri-pot converter is endowed with great fault-tolerance ability, contributing to the system safety improvement.

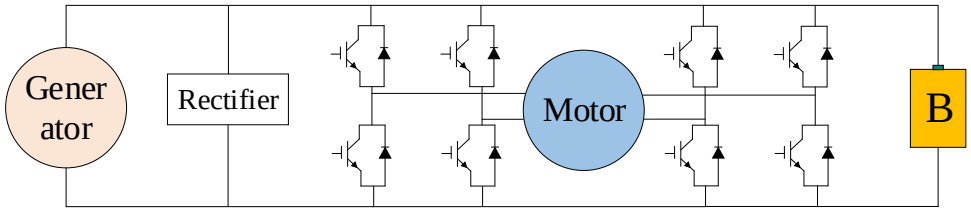

Fig. 2-10. Structure of tri-port converter.

2.2.3 DC-Bus Capacitor

In the powertrain of an EV, the battery pack needs to be connected to the inverter through a DC bus. However, high voltage surges would be generated on the DC bus during the control process, posing significant potential risks to the motor controller. Therefore, it is necessary to employ a DC-bus capacitor that is in parallel with the inverter to absorb the undesired voltage surges. On this ground the functions of a DC-bus capacitor are as follows:

1) To smoothen the bus voltage and reduce the spike voltage especially at the moment when the power transistors are turned on/off.
2) To absorb the current surges on the DC bus.

The application of DC-bus capacitor has changed from the electrolytic capacitor to the commonly used film capacitor, but the use of electrolytic capacitors has not completely disappeared, especially in low-speed vehicles or the logistics vehicle controllers that are based on MOS power electronics. The first generation of the electric powertrain in Toyota Prius used electrolytic capacitor, as is shown in Fig.2-11 (a). Three Panasonic electrolytic capacitors are connected in parallel and their specifications are 450V/2700uF. Nevertheless, the second generation of the Prius powertrain starts to employ the film capacitors made by Panasonic Corporation as well (as in Fig.2-11 (b)). Compared to the electrolytic capacitors, the film capacitors comprises six main advantages: 1) Better thermal and frequency properties; 2) No polarity so as to withstand reverse voltage; 3) Higher rated voltage; 4) No risk of electrolyte leakage; 5) Stronger capacity of current ripple suppression; 6) Longer service life.

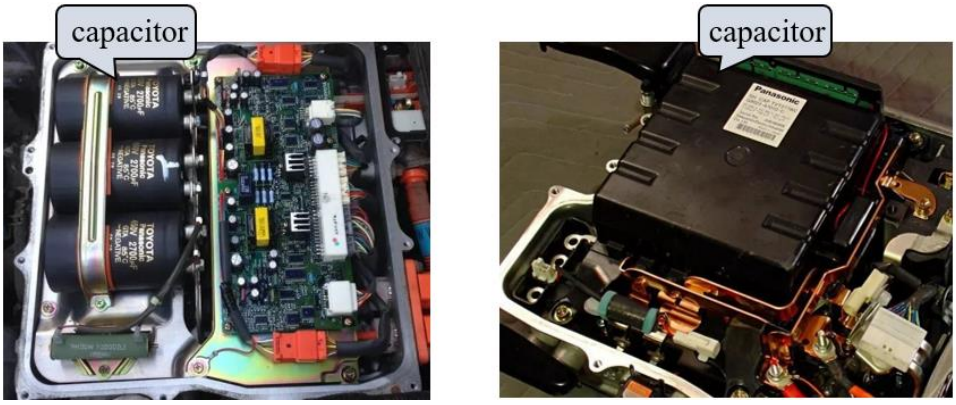

(a) (b)

Fig. 2-11. Capacitor in Toyota Prius. (a) Electrolytic capacitor in the first generation. (b) Film capacitor in the second generation[43].

2.2.4 DC-AC Inverter

Currently, most of the traction motors for EVs are AC machines. Since the battery can only supply DC voltage, DC-AC inverters must be employed for speed and current regulation. The topology of a typical three-phase full-bridge inverter has been depicted in Fig.2-1. Noticeably, the inverter is composed of six transistors and six free-wheeling diodes. The transistor can be controlled by the pulse signals generated by particular pulse width modulation (PWM) algorithms, such as the sine PWM (SPWM) and space vector PWM (SVPWM) algorithms [44].

The freewheeling diodes are crucial in freewheeling in the circuits. Besides, they will constitute an uncontrolled rectifier when the transistors are sealed off once the unwanted faults occur or the regenerative braking state is launched. Additionally, when using a full-bridge inverter, the connection of the machine windings should be in the form of star or delta [45].

2.2.5 Propulsion Motor

The propulsion system is the heart of an EV [46–47], and the electric motor sits right in the core of the system. The motor converts electrical energy that it draws from the battery into mechanical energy which enables the vehicle to move. It also acts as a generator during regenerative action which sends energy back to the energy source. Papers [4, 48] listed the requirements of a motor for EVs, including high power, high torque, wide speed range, high efficiency, reliability, robustness, low noise, small size and flexible structure. Direct current (DC) motor drives demonstrate some required properties needed for EV application, but the presence of the commutator or brushes and maintenance requirement associated in these drives result in lack in efficiency, bulky structure, lack in reliability, making them less attractive [4]. With the advances of power electronics and control systems, different AC motors emerged to meet the needs of the automotive sector, including induction motors (IM), permanent magnet (PM) brushless DC motors (BLDCM), permanent magnet synchronous motors (PMSM) and switched reluctance motors (SRM), etc.

1) DC motors

These motors have permanent magnets (PM) to make the stator; rotors have brushes to supply the stator. The advantage of these motors is that they have demonstrated a great ability to provide maximum torque in low speed. The disadvantages reflect in their bulky structure, low efficiency, large heat generation and the adoption of brushes. The heat is also difficult to remove as it is generated in the centre of the rotor. Due to these reasons, brushed DC motors are not used in EVs in the current industry [49].

2) Induction motors (IM)

IMs are widely used in early EVs like the GM EV1 as well as current models like the Tesla Model S. Among the different AC motor drive systems, IM is the most maturely developed

model [4]. Vector control is useful to empower induction motor drives to meet the requirements of EV systems. Such a system with the ability to minimise loss at any load condition is demonstrated in [50]. Field orientation control enables an IM to act as a separately excited DC motor by decoupling its field control and torque control. Flux weakening can extend the speed range over the base speed while keeping the power constant, while field orientation control can achieve three to five-folds the base speed with a properly designed IM [51].

3) Brushless DC motors (BLDCM)

Permanent magnets are installed in the rotor of this type of motor, and the stator is provided with AC current from the battery through an inverter. As no winding is involved in the rotor, rotor copper loss is negligible, which makes it more efficient than induction motors. This motor is also lighter, smaller, better at heat dissipation and more reliable. It provides larger torque density and more specific power. However, because of its restrained field-weakening ability, the constant power range is relatively short. The output torque also decreases as the speed increases because of back electromotive force (EMF) generated in the stator windings. However, by controlling the conduction angle of the power converter can improve the efficiency of PM BLDCMs and the speed range, reaching as high as four times the base speed, by trading the efficiency at very high speed resulting from demagnetisation of PM [4]. In terms of the PM configurations, the PMs can be buried into the rotor or be mounted on the surface of the rotor.

4) Permanent magnet synchronous motors (PMSM)

These machines are one of the most advanced ones, capable of operating at a wide range of speed without using any gear system. This feature makes these motors more efficient and compact. PMSMs can provide high torque even when the machine speed is deficient. Usually, NdFeB PMs are used in PMSMs for high energy density. In terms of the PMSM rotor structures, same as BLDMs, the PMs can be embedded into the rotor (interior PMSM, IPMSM) or mounted on the surface of the motor rotor (surface-mounted PMSM, SPMSM). Nevertheless, unlike the BLDCMs of which air-gap flux linkage is square, the air-gap flux linkage of a PMSM is sinusoidal intrinsically. Therefore, the PMSMs require to be controlled using standard sinusoidal voltage supplies and the vector control algorithms have been proven to be

suitable [52]. Currently, PMSM is the most commonly used motor in various EV models [53].

5) Switched reluctance motors (SRM)

As a new type of stepper motor, SRM is an electric motor that runs by reluctance torque. The stator and rotor are composed of silicon steel sheet laminates with a "salient pole" structure [54]. No windings, slip rings and PMs are employed on the rotor, and only a simple concentrated field winding is mounted on the stator. The ends of the field windings are short with no interphase jumpers. The magnetic flux is concentrated in the pole region, which is excited by the stator current. The reluctance of the magnetic circuit of each phase varies, which is related to the position of the rotor. The operation of the rotor relies on magnetic attraction, and the rotating speed can be up to 15,000 r/min. According to the number of poles of the rotor and stator, there are several combinations of SRMs, the two most common of which are the three-phase 6/4 structure and the four-phase 8/6 structure.

Table 2-3 summarises the advantages and disadvantages of the motor types mentioned above. Simultaneously, different vehicle models are listed correspondingly. Note that varieties of BEV, HEV and PHEV vehicles composed of different-machine-based powertrains are currently in service and it is significant to implement in-depth investigation for any types of EVs.

TABLE 2-3
Advantages and Disadvantages of Traction Motors and Corresponding Vehicle Models

Motor types	Advantages	Disadvantages	Vehicle models
DC motor	1. Large torque at low speed	1. Bulky structure 2. Low efficiency 3. Use of Brushes	• Fiat Panda Elettra (BEV) • Conceptor G-Van (BEV)
IM	1. Mature technology 2. High control performance 3. Robust structure	1. Lower efficiency than PMSM	• Tesla Model S (BEV) • Tesla Model X (BEV) • Toyota RAV4 (BEV)
BLDCM	1. Wide speed range 2. High efficiency 3. Compact structure	1. Small constant power range 2. High cost due to PMs	• Toyota Prius 2005 (HEV) • Honda civic

	4. Large output torque	3. Larger ripple than PMSM	hybrid (HEV) • Smart Fortwo ED (BEV)
PMSM	1. Wide speed range 2. High efficiency 3. Compact structure 4. Large output torque 5. Large power density 6. No rotor loss	1. High cost due to PMs	• Toyota Prius (HEV) • Nissan Leaf (BEV) • Soul EV (BEV)
SRM	1. Simple and robust structure 2. Low cost 3. Wide speed range 4. Relatively high efficiency	1. Large ripples 2. Much noise 3. Lower efficiency than PM machines 4. Complex control schemes	• Chloride Lucas (HEV) • Holden ECOmmodore (BEV)

2.3 Safety Issues Considering Regulatory Activities

The electric powertrains of EVs bear the responsibility of transmitting the electric power to the mechanical power, while the traditional ICE powertrains transfer the chemical energy stored in the fuel into mechanical power. From the perspective of energy conversion, the electric safety issues of EVs should gain more attention compared to ICE vehicles, and they can be treated as the particular safety hazards for EVs. As explained in the previous sections, the EV powertrains are composed of battery, converter, inverter, DC-bus capacitor and traction motors. As a power source (energy storage tank), the battery pack requires to provide high voltage (e.g., 300 V~600 V) and ample output power (current) to ensure normal operations of vehicles.

Meanwhile, the power electronic devices need to operate under high-voltage and high-power situations. The dangers of the high voltage and high power, such as electric shocks, are indeed noticeable for passengers or drivers. Besides, the battery fire affairs and crash safety problems are diverting the market interests in EVs. In addition to the consumers, the experts and engineers in the area of EVs never stops exploring novel technologies and creating up-to-date regulations to enhance the vehicle safety level. For example, European Community Whole Vehicle Type-Approval (ECWVTA), UN Regulations, International Organisation for

Standardisation (ISO) and International Electrotechnical Commission (IEC) [55]. According to the UN Regulations, the safety provisions for EVs should cover electrical safety in: firstly, the normal and daily use; secondly, following crash cases. The "normal-use" topics include:

1) Protection from electric shock.
2) Safety requirements for rechargeable energy.
3) Functional safety and protection against failures.

The "post-crash" topics include:

1) Electrical isolation and protection from electric shock.
2) Battery integrity.
3) Battery discharge procedures.
4) Power electronics discharge procedures.

This part will discuss several potential safety risks for EVs following the international regulations (UN regulations) [56]. It is the intention to scientifically explain the potential hazards that exist in EVs, contributing to a better understanding of the EV electric safety problems. Additionally, the explanations will provide guidelines for developing brand-new safety improvement techniques in the near future.

2.3.1 Safety in Normal-Use

1) Protection from electric shock

The voltages used in EVs are potentially hazardous. However, a range of safety features is typically used to ensure the safety of drivers or other passengers. Crucially, the high voltage circuit is isolated from the vehicle chassis (and any other conductors), meaning a person would need to touch both the positive and the negative sides of the circuit to receive an electric shock. This hazard only occurs at the loss of isolation on both sides of the circuit (i.e. a double-fault). In fact, the ground-fault monitoring system would detect any leakage of current and would disconnect the high voltage system from the rechargeable energy storage system.

The safety requirements for electrical powertrains are set in UN Regulation 100. In terms of the protection against electric shock, the requirements generally apply to high voltage buses

when they are disconnected to external high voltage supplies. Three main measures are as follows: 1) protection against direct contact; 2) protection against indirect contact with exposed conductive parts; 3) isolation resistance. In detail, vehicles may employ various means to prevent direct contact with live parts, such as insulating materials or physical barriers. UN Regulation 100 ensures that conventional electrical protection degrees (e.g., ingress protection XXB, IPXXB) are enforced [57]. For example, the regulation specifies that live parts in the passenger or luggage compartments must be protected to a degree of at least IPXXD. Enclosures in other areas must have a protection degree of at least IPXXB. In each case, an access probe is pushed against any openings of the enclosure with a specified test force and must not be in connection of live parts. In the case of IPXXD, the probe is a test wire, 1 mm in diameter and 100 mm long, and in the case of IPXXB, the probe is a jointed test finger, 12 mm in diameter and 80 mm long. Protection against indirect contact with live parts is closely related to the prevention of electrical faults. The regulation requires that any exposed conductive parts, such as barriers or enclosures, are connected to the chassis to prevent dangerous potentials being produced. The regulation also specifies a limit for the resistance between all exposed conductive parts and the chassis of 0.1 ohms when there is a current flow of at least 0.2 amperes. Finally, detailed specifications are included for isolation resistance. The specifications depend on whether the power train comprises separate or combined DC and AC buses. Limits are specified according to the types of buses and their connections, and test procedures are provided in an annexe.

2) Safety requirements for rechargeable energy

The rechargeable energy storage system is arguably the key component of an EV. Although batteries are the most common type, electric double-layer capacitors and electro-mechanical flywheels may also be used. Any type of rechargeable energy storage system possesses potential hazards if designed uncarefully. Hazards can emerge during the normal operation of the battery or conditions or events outside its normal operating range. These include electrolyte/material spillage if individual cell casings are damaged, the battery's reaction to high external temperatures and fire, and its electrical properties under short circuit, over-voltage and voltage reversal conditions.

UN Regulation 100 deals with the safety of EVs "normal-use" and includes specifications that

relate mainly to the protection of users against electric shock. There are some original specifications for rechargeable energy storage systems, which cover the protection against excessive current and accumulation of gas. The main requirement concerning excessive current is simply that the rechargeable energy storage system "shall not overheat". However, if it is subject to overheating, it must be equipped with a protective device such as fuses, circuit breakers or main contactors. Accumulation of gas is controlled by a requirement to provide a ventilation fan or duct in places containing an "open-type battery" that may produce hydrogen gas. UN Regulations 94 and 95 (frontal and side-impact respectively) are being amended to include post-impact electrical safety requirements for EVs that will cover protection against electric shock, retention of the rechargeable energy storage system and electrolyte spillage following the impact test.

3) Functional safety and protection against failures

Functional safety relates to the overall safety of a system and is particularly crucial for complex software-based systems. EVs typically require greater use of distributed control systems than conventional vehicles, which can be highly integrated. However, the focus here is not on these complex electrical and electronic systems. Instead, consideration is given to the potentials for unexpected vehicle movements caused by drivers (or others) being unaware that the vehicle is in an active mode. EVs could present some potential functional safety hazards, particularly around the safe operation of the powertrain by drivers. For example, if the vehicle is stationary for a period of time, such as in a car park or similar situation, a driver may "forget" that the vehicle is capable of motion. They may leave the vehicle in this condition, or they may unintentionally activate the powertrain. To prevent inadvertent movement through activation of the drive circuit, the presence of a warning device is necessary. Procedure access must be properly organized to avoid possible harm through excessive torque, amperage or excessive acceleration, which eliminates the possibility of activating the controller when the accelerator is pressed. For EVs, it is mandatory to have a device (switch) in case of emergencies. Electromagnetic interference coming from outside or the controller must not affect the functioning of the controller. The powertrain components are expected to provide high reliability and strong capability against unwanted faults (fault tolerance). Because some of these functions must be realized with the aid of control algorithms, the control and management schemes of an EV powertrain (e.g., battery management and machine drive strategies, etc.)

should be reliable and elaborate [58-59].

UN Regulation 100 includes basic functional safety requirements that deal with the safety of the drivers, passengers and pedestrians outside. For instance, the regulation requires that:

1) At least a momentary indication is given to the driver when the vehicle is in "active driving mode".
2) When leaving the vehicle, the driver must be informed by a signal if the vehicle is still in the active driving mode.
3) Vehicle movement by its own propulsion system is prevented during charging as long as the connector of the external power supply is physically connected to the vehicle inlet.
4) The state of the drive direction control unit is identified to the driver.
5) The powertrain components and control/management schemes are reliable, elaborate and fault-tolerant, etc.

2.3.2 Safety in Post-Crash

A collision could compromise electric safety measures and could increase the risk of electric shock. For example, electrical isolation might be compromised, leading to both the positive and negative sides of the circuit come into contact with the vehicle bodywork. If any of the occupants touched the bodywork, they would become part of the high voltage circuit and would receive an electric shock. However, it is likely that most EVs will be fitted with a device that disconnects the energy storage system from the high voltage circuit in the event of a crash. This is generally achieved by linking the system to crash detection sensors used to activate pre-tensioners and airbags. Disconnecting the energy storage system from the rest of the high voltage circuit will reduce the risk of electric shock during and following a crash. Also, it will also be essential to ensure that the energy storage system is not damaged in such a way that can lead to a fire or an explosion. Furthermore, discharging the energy stored in the high-voltage power electronics (e.g., DC-bus capacitor and traction motor) will be necessary for the safe handling and recovery of the vehicle.

UN Regulation 94 sets the minimum requirements for the frontal impact performance of cars. They both specify a frontal impact test in which the car is propelled into an offset, deformable

barrier at 56 km/h. Similarly, UN Regulation 95 sets the minimum requirements for side-impact performance. They specify an impact test in which a mobile deformable barrier is propelled into the side of the car at 50 km/h. The test procedures and occupant safety requirements could be applied to any vehicle, regardless of powertrain types. However, there are no specifications for the preparation of an electrical powertrain or the electrical safety of the occupants during and following the impact. In 2009, a group of experts was formed to work on post-crash provisions for EVs. The aim of the task was to derive amendments to UN Regulations 94 and 95 so that they are appropriate for the assessment of EVs. The group was formed mainly of experts in electrical safety from the UN informal working group on electrical safety and experts in crash safety from the UN informal working group on frontal impact. The proposals to amend UN Regulations 94 and 95 were completed in 2010. With regards to the protection against electric shock following the impact test, the amendments specify four performance criteria:

1) Physical protection (IPXXB and resistance between exposed conductive parts and electrical chassis < 0.1 Ω).
2) Electrical isolation (minimum resistance specified depending on whether DC and AC buses are separate or combined)
3) Absence of high voltage (⩽ 30 VAC or 60 VDC).
4) Low electrical energy (< 2 Joules).

As denoted from the amendments, at least one of these four criteria must be met following the impact test. However, the isolation resistance criterion does not apply if more than one part of the high voltage bus is unprotected (i.e. the conditions of IPXXB are not met). This requirement was added to prevent vehicles meeting the isolation resistance criterion and hence gaining approval while presenting a risk of electric shock. If the vehicle is equipped with an automatic device that separates the energy storage system from the rest of the high voltage circuit in the event of a crash, or a device that divides the power train circuit, (one of) the criteria must be met by the disconnected circuit, or by each divided circuit individually after the disconnect function is activated.

UN Regulations 94 and 95 also specify requirements for the retention of the rechargeable energy storage system and electrolyte spillage. The requirements for the retention of the rechargeable energy storage system depend on its location. If it is located within the passenger

compartment, it must remain in the location in which it is installed, and all the components must remain within its boundaries. No part of an energy storage system located outside the passenger compartment can enter the passenger compartment during the test. Electrolyte spillage within the passenger compartment is not allowed in the amendments to UN Regulations 94 and 95. Outside the passenger compartment, it is limited to 7%. These requirements are valid over a 30-minute period, starting from the point of impact. Batteries have traditionally featured liquid electrolytes. However, solid electrolytes have started to emerge. The amendments do not distinguish between liquid and solid electrolytes and hence the 7% limit should apply in either case.

2.4 Summary

This chapter reviews the EV categories, powertrain components and the safety considerations for EVs. Firstly, the EVs are classified into BEVs, HEVs and PHEVs according to their powertrain structures and components. Then, the components in the EVs are introduced, which reveals two crucial problems: 1) the power electronics and the rechargeable energy storage system are usually operating at high-voltage and high-power conditions, which constitutes the main reasons for the electric shock risks; 2) there are a variety of EV models in terms of different components comprised, each of which deserves in-depth investigation. Finally, from a professional perspective, the EV safety issues are analysed following the UN regulations. The review work is significant in the following two aspects: 1) ordinary readers will gain a more comprehensive understanding of EV safety problems; 2) scholars can learn how the EV hazards are regulated by the international standards, providing guidelines for future studies on EV safety improvement techniques. It needs to be mentioned that the work in the following chapters will show efforts to address these regulations.

2.5 References

[1] P. Saad, C. Fager, H. Cao, H. Zirath and K. Andersson, “Design of a highly efficient 2-4ghz octave band-width GaN-HEMT power amplifier," IEEE Trans. Microwave Theory and Techniques, vol. 58, pp. 1677-1685, Jul.2010.

[2] Yeqin Wang and Yixing Liu, "Electronic control system design and test of pure electric vehicle battery management system," *2011 Second International Conference on Mechanic Automation and Control Engineering*, Hohhot, 2011, pp. 1289-1292.

[3] X. Bai, "Pure electric vehicle power system parameters matching and the analysis of vehicle control," *2014 IEEE Workshop on Advanced Research and Technology in Industry Applications (WARTIA)*, Ottawa, ON, 2014, pp. 737-740.

[4] C. C. Chan, "The State of the Art of Electric, Hybrid, and Fuel Cell Vehicles," in *Proceedings of the IEEE*, vol. 95, no. 4, pp. 704-718, April 2007.

[5] R. Ghorbani, E. Bibeau and S. Filizadeh, "On Conversion of Hybrid Electric Vehicles to Plug-In," in *IEEE Transactions on Vehicular Technology*, vol. 59, no. 4, pp. 2016-2020, May 2010.

[6] J. Xie, X. Han, T. Ding, J. Shi, M. Wang and L. Li, "Operation Strategy and Reliability Analysis of the Control System for the Hybrid Capacitor-Battery Pulsed High Magnetic Field Facility," in *IEEE Transactions on Applied Superconductivity*, vol. 24, no. 3, pp. 1-4, June 2014, Art no. 3800804.

[7] M. Carignano, V. Roda, R. Costa-Castelló, L. Valiño, A. Lozano and F. Barreras, "Assessment of Energy Management in a Fuel Cell/Battery Hybrid Vehicle," in *IEEE Access*, vol. 7, pp. 16110-16122, 2019.

[8] A. Rufer and S. Lemofouet, "Energetic performance of a hybrid energy storage system based on compressed air and super capacitors," *International Symposium on Power Electronics, Electrical Drives, Automation and Motion, 2006. SPEEDAM 2006.*, Taormina, 2006, pp. 469-474.

[9] O. M. F. Camacho, P. B. Nørgård, N. Rao and L. Mihet-Popa, "Electrical Vehicle Batteries Testing in a Distribution Network Using Sustainable Energy," in *IEEE Transactions on Smart Grid*, vol. 5, no. 2, pp. 1033-1042, March 2014.

[10] E. A. Grunditz and T. Thiringer, "Performance Analysis of Current BEVs Based on a Comprehensive Review of Specifications," in *IEEE Transactions on Transportation Electrification*, vol. 2, no. 3, pp. 270-289, Sept. 2016.

[11] SAE International. SAE Electric Vehicle and Plug-in Hybrid Electric Vehicle Conductive Charge Coupler. In *SAE Standard J1772*, Society of Automotive Engineers (SAE): Warrendale, PA, USA, 2010.

[12] M. Yilmaz and P. T. Krein, "Review of Battery Charger Topologies, Charging Power Levels, and

Infrastructure for Plug-In Electric and Hybrid Vehicles," in *IEEE Transactions on Power Electronics*, vol. 28, no. 5, pp. 2151-2169, May 2013.

[13] IEEE Standard Technical Specifications of a DC Quick Charger for Use with Electric Vehicles," in *IEEE Std 2030.1.1-2015*, vol., no., pp.1-97, 5 Feb. 2016

[14] Un-Noor, F.; Padmanaban, S.; Mihet-Popa, L.; Mollah, M.N.; Hossain, E. A Comprehensive Study of Key Electric Vehicle (EV) Components, Technologies, Challenges, Impacts, and Future Direction of Development. *Energies* 2017, *10*, 1217.

[15] M. H. Hajimiri and F. R. Salmasi, "A Fuzzy Energy Management Strategy for Series Hybrid Electric Vehicle with Predictive Control and Durability Extension of the Battery," *2006 IEEE Conference on Electric and Hybrid Vehicles*, Pune, 2006, pp. 1-5.

[16] S. J. Kim, K. Kim and D. Kum, "Feasibility Assessment and Design Optimization of a Clutchless Multimode Parallel Hybrid Electric Powertrain," in *IEEE/ASME Transactions on Mechatronics*, vol. 21, no. 2, pp. 774-786, April 2016.

[17] Y. Yan and H. Xie, "Model predictive control for series-parallel plug-in hybrid electrical vehicle using GPS system," *2011 International Conference on Electrical and Control Engineering*, Yichang, 2011, pp. 2334-2337.

[18] Y. Pan, S. He and X. Tang, "High-efficiency series–parallel form hybrid envelope-tracking power supply based on the optimised power losses," in *Electronics Letters*, vol. 55, no. 14, pp. 810-813, 11 7 2019.

[19] Yimin Gao, M. Ehsani and J. M. Miller, "Hybrid Electric Vehicle: Overview and State of the Art," *Proceedings of the IEEE International Symposium on Industrial Electronics, 2005. ISIE 2005.*, Dubrovnik, Croatia, 2005, pp. 307-316.

[20] W. Kreeumporn and I. Ngamroo, "Optimal Superconducting Coil Integrated Into PV Generators for Smoothing Power and Regulating Voltage in Distribution System With PHEVs," in *IEEE Transactions on Applied Superconductivity*, vol. 26, no. 7, pp. 1-5, Oct. 2016, Art no. 5402805.

[21] H. Nafisi, S. M. M. Agah, H. Askarian Abyaneh and M. Abedi, "Two-Stage Optimization Method for Energy Loss Minimization in Microgrid Based on Smart Power Management Scheme of PHEVs," in *IEEE Transactions on Smart Grid*, vol. 7, no. 3, pp. 1268-1276, May 2016.

[22] P. Grahn, J. Munkhammar, J. Widén, K. Alvehag and L. Söder, "PHEV Home-Charging Model Based on Residential Activity Patterns," in *IEEE Transactions on Power Systems*, vol. 28, no. 3, pp. 2507-2515, Aug. 2013.

[23] S. S. Williamson, "Electric Drive Train Efficiency Analysis Based on Varied Energy Storage System

Usage for Plug-In Hybrid Electric Vehicle Applications," *2007 IEEE Power Electronics Specialists Conference*, Orlando, FL, 2007, pp. 1515-1520.

[24] S. G. Wirasingha, N. Schofield and A. Emadi, "Plug-in hybrid electric vehicle developments in the US: Trends, barriers, and economic feasibility," *2008 IEEE Vehicle Power and Propulsion Conference*, Harbin, 2008, pp. 1-8.

[25] B. Kramer, S. Chakraborty and B. Kroposki, "A review of plug-in vehicles and vehicle-to-grid capability," *2008 34th Annual Conference of IEEE Industrial Electronics*, Orlando, FL, 2008, pp. 2278-2283.

[26] M. Vasiladiotis and A. Rufer, "A Modular Multiport Power Electronic Transformer With Integrated Split Battery Energy Storage for Versatile Ultrafast EV Charging Stations," in *IEEE Transactions on Industrial Electronics*, vol. 62, no. 5, pp. 3213-3222, May 2015.

[27] N. Tashakor, E. Farjah and T. Ghanbari, "A Bidirectional Battery Charger With Modular Integrated Charge Equalization Circuit," in *IEEE Transactions on Power Electronics*, vol. 32, no. 3, pp. 2133-2145, March 2017.

[28] C. Kim, M. Kim and G. Moon, "A Modularized Charge Equalizer Using a Battery Monitoring IC for Series-Connected Li-Ion Battery Strings in Electric Vehicles," in *IEEE Transactions on Power Electronics*, vol. 28, no. 8, pp. 3779-3787, Aug. 2013.

[29] N. SARAVANAN and S. HOSIMIN THILAGAR, "Ultracapacitor Aided Performance Enhancement of Battery Powered Electric Vehicles," *2018 IEEE International Conference on Power Electronics, Drives and Energy Systems (PEDES)*, Chennai, India, 2018, pp. 1-4.

[30] Amal S., R. V. Chacko, Sreedevi M.L, Mineeshma G.R and Vishnu V., "Modelling of ultracapacitor and Power Management strategy for the parallel operation of Ultracapacitor and Battery in Electric Vehicle Configuration," *2016 IEEE International Conference on Power Electronics, Drives and Energy Systems (PEDES)*, Trivandrum, 2016, pp. 1-6.

[31] A. Singh and P. B. Karandikar, "Lead-acid battery for HEV using fuzzy controller and ultracapacitor," *2016 Biennial International Conference on Power and Energy Systems: Towards Sustainable Energy (PESTSE)*, Bangalore, 2016, pp. 1-5.

[32] C. Pillot, "Micro hybrid, HEV, P-HEV and EV market 2012–2025 impact on the battery business," *2013 World Electric Vehicle Symposium and Exhibition (EVS27)*, Barcelona, 2013, pp. 1-6.

[33] Z. Cai, G. Liu and J. Luo, "Research State of Charge Estimation Tactics of Nickel-Hydrogen Battery," 2010 International Symposium on Intelligence Information Processing and Trusted Computing,

Huanggang, 2010, pp. 184-187.

[34] M. A. Hannan, M. M. Hoque, A. Hussain, Y. Yusof and P. J. Ker, "State-of-the-Art and Energy Management System of Lithium-Ion Batteries in Electric Vehicle Applications: Issues and Recommendations," in *IEEE Access*, vol. 6, pp. 19362-19378, 2018.

[35] X. Chen, W. Shen, T. T. Vo, Z. Cao and A. Kapoor, "An overview of lithium-ion batteries for electric vehicles," *2012 10th International Power & Energy Conference (IPEC)*, Ho Chi Minh City, 2012, pp. 230-235.

[36] M. Scarfogliero *et al*., "Lithium-ion batteries for electric vehicles: A review on aging models for vehicle-to-grid services," *2018 International Conference of Electrical and Electronic Technologies for Automotive*, Milan, 2018, pp. 1-6.

[37] S. M. Lukic, J. Cao, R. C. Bansal, F. Rodriguez and A. Emadi, "Energy Storage Systems for Automotive Applications," in *IEEE Transactions on Industrial Electronics*, vol. 55, no. 6, pp. 2258-2267, June 2008.

[38] H. Liu, M. S. A. Dahidah, J. Yu, R. T. Naayagi and M. Armstrong, "Design and Control of Unidirectional DC–DC Modular Multilevel Converter for Offshore DC Collection Point: Theoretical Analysis and Experimental Validation," in *IEEE Transactions on Power Electronics*, vol. 34, no. 6, pp.

[39] O. C. Onar, J. Kobayashi, D. C. Erb and A. Khaligh, "A Bidirectional High-Power-Quality Grid Interface With a Novel Bidirectional Noninverted Buck–Boost Converter for PHEVs," in *IEEE Transactions on Vehicular Technology*, vol. 61, no. 5, pp. 2018-2032, Jun 2012.

[40] Z. Tao and L. Li, "Control loop design and bidirectional control strategy of a bidirectional DC/DC converter," *IECON 2017 - 43rd Annual Conference of the IEEE Industrial Electronics Society*, Beijing, 2017, pp. 5720-5725.

[41] Y. Hu, C. Gan, W. Cao and Y. Fang, "Tri-port converter for flexible energy control of PV-fed electric vehicles," *2015 IEEE International Electric Machines & Drives Conference (IEMDC)*, Coeur d'Alene, ID, 2015, pp. 1063-1070.

[42] H. Al-Atrash, F. Tian and I. Batarseh, "Tri-Modal Half-Bridge Converter Topology for Three-Port Interface," in *IEEE Transactions on Power Electronics*, vol. 22, no. 1, pp. 341-345, Jan. 2007.

[43] Motor controller bus capacitance selection and detailed analysis. Available: http://www.lllio.com/newsinfo/1278720.html?templateId=1133604.

[44] M. Wu and R. Zhao, "Method analysis and comparison of SVPWM and SPWM," *Proceedings of the 29th Chinese Control Conference*, Beijing, 2010, pp. 3184-3187.

[45] F. J. T. E. Ferreira, M. V. Cistelecan and A. T. de Almeida, "Comparison of Different Tapped Windings for Flux Adjustment in Induction Motors," in *IEEE Transactions on Energy Conversion*, vol. 29, no. 2, pp. 375-391, June 2014.

[46] K. Kim, "A Novel Magnetic Flux Weakening Method of Permanent Magnet Synchronous Motor for Electric Vehicles," in *IEEE Transactions on Magnetics*, vol. 48, no. 11, pp. 4042-4045, Nov. 2012.

[47] C. C. Chan, J. Z. Jiang, G. H. Chen and K. -. Chau, "Computer simulation and analysis of a new polyphase multipole motor drive," in *IEEE Transactions on Industrial Electronics*, vol. 40, no. 6, pp. 570-576, Dec. 1993.

[48] K. Rajashekara, "Present Status and Future Trends in Electric Vehicle Propulsion Technologies," in *IEEE Journal of Emerging and Selected Topics in Power Electronics*, vol. 1, no. 1, pp. 3-10, March 2013.

[49] C.P. Jose, S. Meikandasivam, A Review on the Trends and Developments in Hybrid Electric Vehicles. *InInnovative Design and Development Practices in Aerospace and Automotive Engineering*, pp. 211–229,Springer: Singapore, 2017.

[50] K. Yamada, K. Watanabe, T. Kodama, I. Matsuda, T. Kobayashi, “An efficiency maximizing induction motor drive system for transmissionless electric vehicle,” *In Proceedings of the 13th International ElectricVehicle Symposium*, Osaka, Japan, vol.2, pp. 529–536, Oct. 1996.

[51] A. Boglietti, P. Ferraris, M. Lazzari, F. Profumo, “A new design criteria for spindles induction motors controlled by field-oriented technique,” *Electr. Mach. Power Syst.*, vol.21, pp.171–182, 1993.

[52] C.P. Jose, S. Meikandasivam, “A Review on the Trends and Developments in Hybrid Electric Vehicles,” *In Innovative Design and Development Practices in Aerospace and Automotive Engineering, Springer: Singapore*, pp. 211–229, 2017.

[53] II-Kuen Won, Jun-Ha Hwang, Do-Yun Kim, Young-Hee Jang and Chung-Yuen Won, "Performance improvement of IPMSM using finite predictive current control for EV," *2015 IEEE 2nd International Future Energy Electronics Conference (IFEEC)*, Taipei, 2015, pp. 1-7.

[54] M. Jahanmahin, A. Hajihosseinlu, E. Afjei, A. Siadatan and A. Tavakoli, "A novel multilayer 8 by 4 switch reluctance machine with ripple reduction," *International Symposium on Power Electronics Power Electronics, Electrical Drives, Automation and Motion*, Sorrento, 2012, pp. 536-540.

[55] C. Visvikis, “Safety considerations for electric vehicles and regulatory activities,” in *26th Electric Vehicle Symposium*, Los Angeles, CA, pp.1-14, May 2012.

[56] United Nation Economic Commission for Europe Vehicle Regulation, No.94 (ECE R94), Unifrom provisions concerning the approval of vehicles with regard to the protection of the occupants in the event of a frontal collision, Rev. 2, Annex 11, Aug. 2013.

[57] A. Fornells, and N., Parera, "Safety Protocol for Crash Tests Involving Electric and Hybrid Vehicles," in *Symposium on International Automotive Technology 2017*, United States, pp.1-6, Jan. 2017.

[58] B. Bilgin *et al*., "Making the Case for Electrified Transportation," in *IEEE Transactions on Transportation Electrification*, vol. 1, no. 1, pp. 4-17, June 2015.

[59] R. Xiong, J. Cao, Q. Yu, H. He and F. Sun, "Critical Review on the Battery State of Charge Estimation Methods for Electric Vehicles," in *IEEE Access*, vol. 6, pp. 1832-1843, 2018.

Chapter 3 Modular Tri-port Converter with Fault-Tolerance Capability for Switched Reluctance Motor based HEVs

Chapter 2 illustrates that SRM-based HEV is one of the promising means of transportation. In the powertrain of these applications, there are three critical electrical components: generator, battery bank, and SRM. This section will illustrate a tri-port converter that can combine the three energy components using a single power converter, which is of high reliability. The tri-port converter has a modular and concise structure, which meets the requirements for HEV applications. The proposed tri-port converter supports six working modes, including generator to SRM, battery bank to SRM, generator and battery bank to SRM, generator to SRM and battery bank, and battery bank to SRM and generator under driving conditions. Under standstill conditions, the generator to battery bank and battery bank to generator energy flow can also be realized without requiring extra converters. The corresponding control strategies are also developed to cooperate with different working modes. Moreover, the fault tolerance characteristics of the tri-port converter are investigated to expand its feasibility under harsh HEV application conditions, enhancing the safety level of the system. The simulation and experiments are undertaken on a prototype to evaluate the performance of the proposed tri-port converter for HEV applications.

3.1 Introduction

For a HEV, there are three main energy components, namely, a battery, a motor, and a generator. To support flexible energy flows, several power electronics converters are needed as shown in Fig.3-1, in which B stands for battery bank, M stands for SRM, and G stands for generator/starter [1-4]. Specifically, B-M denotes the battery bank supplies energy to the drive motor alone; M-B denotes the motor recycles energy to the battery bank; G-M means the generator supplies energy to the drive motor alone. Currently, some HEV integrates the

generator and starter in a single motor. Therefore, the battery needs to supply energy to the generator to start the ICE, which is B-G [5]. G-B indicates that the generator charges the battery bank under HEV standstill conditions. G-M-B stands for the case that the generator supplies energy to the motor and charges the battery simultaneously. B-G refers to the situation that the battery bank supplies energy to the generator to start the ICE. For M-G-B, the motor releases energy to the generator and battery bank in the braking condition. In order to simplify the system structure, a tri-port converter is needed to combine the generator, battery, and motor in one converter, through which flexible energy flow states are realized. In addition to the functional requirements for adjustable energy flow, the modular structure and simple power electronics topology are also the basis for electric powertrains of HEV to achieve massive production. Therefore, developing a power electronics converter with the mentioned characteristics is an urgent priority.

Currently, a number of topologies have been proposed for SRM based EVs/HEVs [6], [7-10]. Paper [6] presents an advanced three-phase 12/8 SRM drive system with integrated charging functions to enhance the market adoption of plug-in HEVs. However, in this converter, the battery bank terminal voltage should match the ICE generator output voltage, which decreases the system design flexibility. Paper [7] developed an integrated driving/charging SRM drive with a front-end converter for EVs to achieve plug-in charging, which does not include the tri-port function. In paper [8], by adding a passive circuit to the front-end of a conventional asymmetric converter, the new converter can boost the dc-link voltage for a high negative bias in the demagnetisation mode. However, this topology is only used for the driving function. In paper [9], a dual-source drive topology for SRM was studied, which allows an SRM to operate from ac mains or a low voltage battery supply, without applying a transformer to match the two voltage levels. However, the converter structure is relatively complex. Another low-cost battery-powered SRM drive with driving and charging functions was also proposed in [10]. Its battery charging is achieved through the motor windings without external transformers or other charging units. Due to the non-modular structure, the converter cannot be used in HEV. In order to obtain the characteristics of fast current build-up and suitable demagnetisation, a power converter with the functions of increased excitation and demagnetisation voltages was designed by using an additional capacitor for high-speed operations [11]. Nevertheless, it is only used for the driving mode. Similarly, paper [12] proposed a four-level converter for SRM driving

system to achieve fast demagnetization. Although the above-mentioned state-of-the-art research has developed numerous driving topologies for SRM driving or driving and charging integration topology, none of which can stratify the function presented in Fig.3-1.

In this chapter, a novel converter with the characteristics of tri-port and modular structure is proposed. The proposed topology can support all of the six working modes without changing the traditional driving topology of SRM. Moreover, the proposed converter has the fault tolerance function, which can block the fault point to achieve fault tolerance operation.

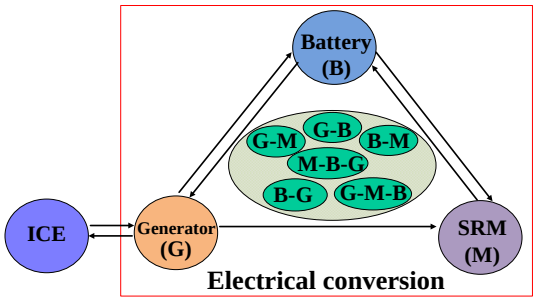

Fig. 3-1. Desired energy flow modes.

3.2 Tri-port Converter and Operation Modes

3.2.1 Proposed Tri-port Converter

Fig.3-2 presents the proposed converter and its deduction progress. In Fig.3-2, S_1~S_8 are MOSFETs; D_1~D_8 are diodes; J_1, J_2 and J_3 are the relays that are used for fault tolerance operation. Three ports are included for the proposed converter: the first port is connected with the generator, and the second port is connected with the battery tank. The first and the second ports are combined by a front-end three-level DC-DC converter, as shown in Fig.3-2 (a). V_1 and V_2 are the voltages of the generator (G) and battery bank (B), respectively. The third port is SRM, and the corresponding drive topology is a traditional asymmetrical half-bridge, as shown in Fig.3-2 (c), in which N_a, N_b and N_c are the central tapped nodes that can be achieved without any changes in the SRM body structure. L_{a12} and L_{a34} are the windings of phase A of SRM, as shown in Fig.3-2 (b); similarly, L_{b12} and L_{b34} are the windings of phase B of SRM; L_{c12} and L_{c34} are the windings of phase C of SRM. The phase winding nodes are linked with the front-end three-level converter by a relay. The whole proposed topology is illustrated in

Fig. 3-2 (d).

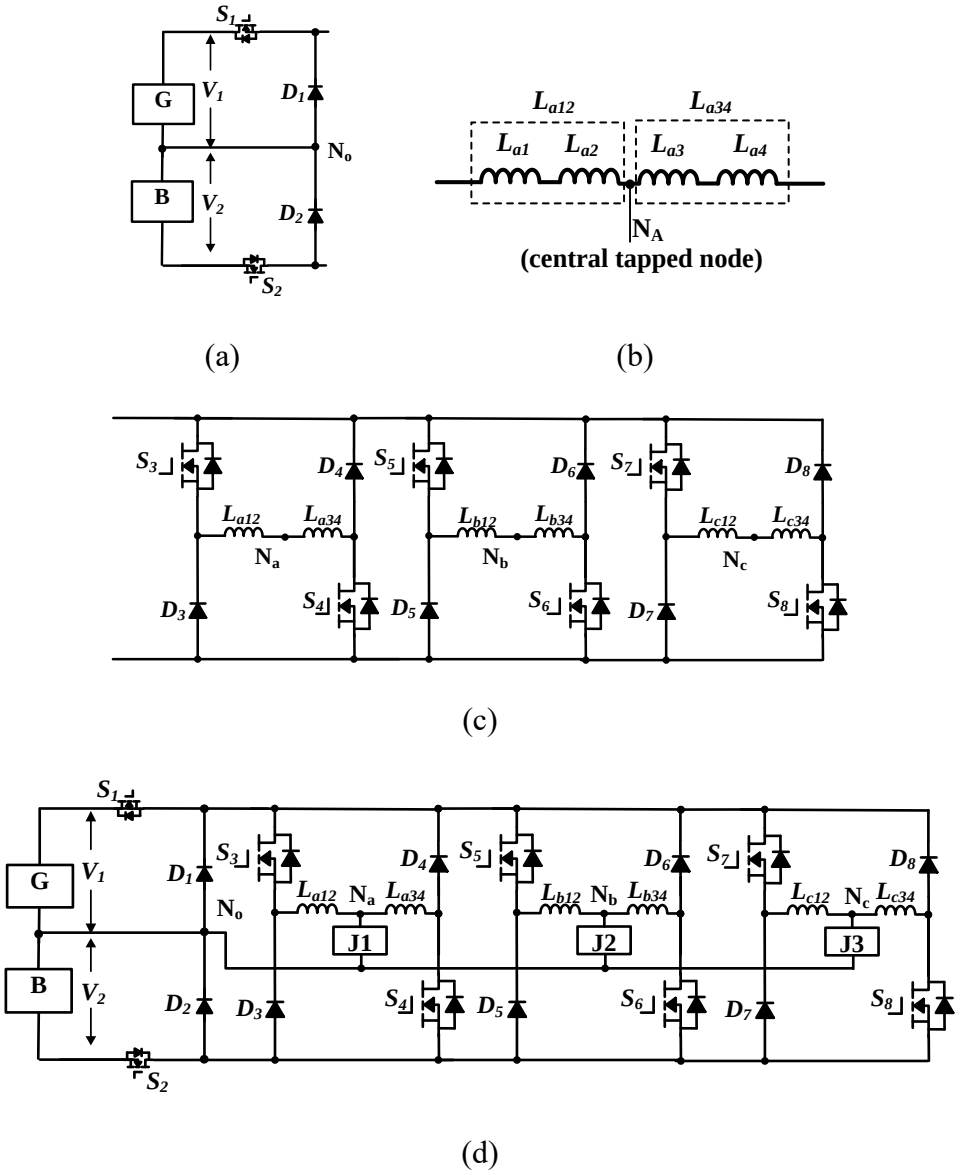

Fig. 3-2. Proposed SRM driving topology. (a) Front-end tree-level converter. (b) Traditional asymmetrical half bridged. (c) Phase winding with a central tapped node. (d) Proposed multi-level and fault tolerance driving topology for SRM.

The proposed topology comprises a modular structure that is convenient for massive production. As shown in Fig.3-3, the proposed topology is composed of eight modules, in which a diode and a switching device together form a module. Compared with a traditional asymmetrical half-bridge driving topology for SRM, only two extra modules are added.

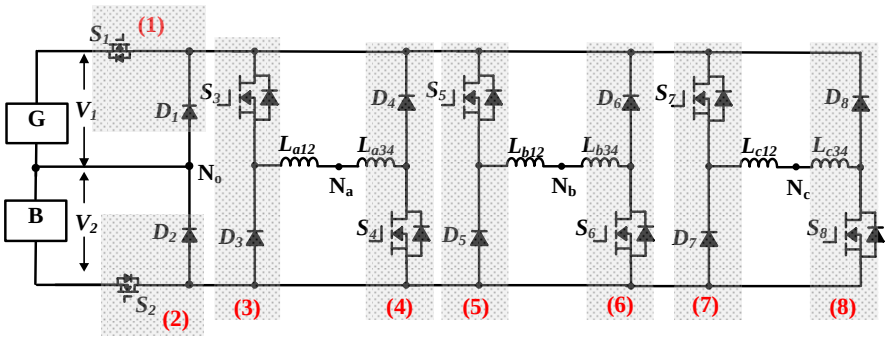

Fig. 3-3. Modular structure of proposed converter.

3.2.2 Working States of Proposed Converter

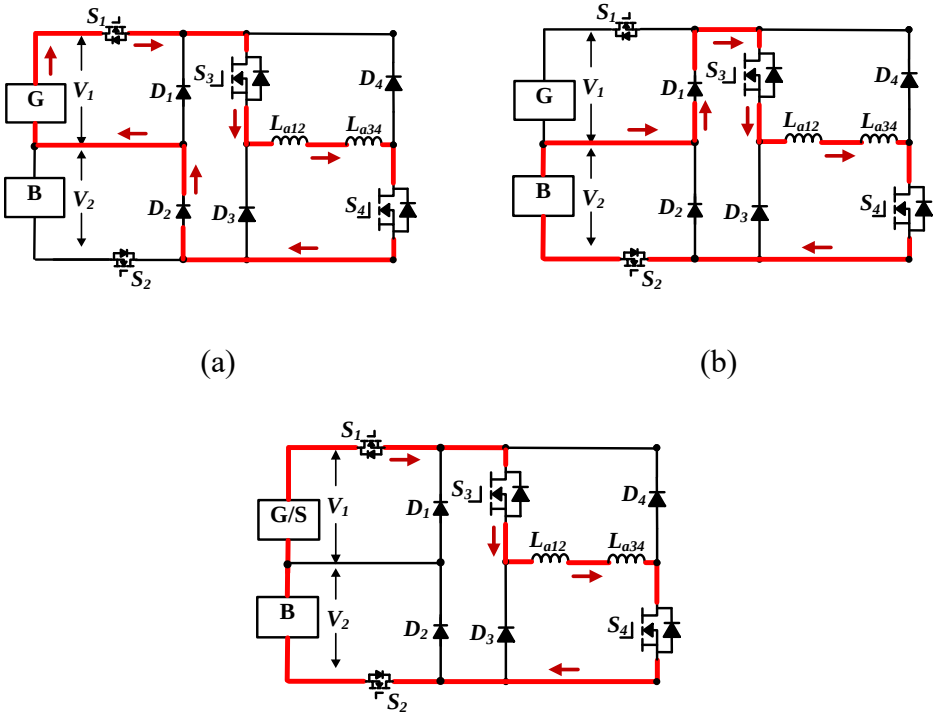

(a) (b)

(c)

Fig. 3-4. Excitation working states. (a) State 1. (b) State 2. (c) State 3.

In the proposed topology, there are different working states for different energy flow modes. When both the generator and battery bank are working, by controlling the switching devices S_1 and S_2, three excitation modes can be achieved as shown in Fig.3-4. In Fig.3-4 (a). S_1 is conducted, and only the generator supplies energy to the motor; in Fig.3-4 (b), conducting S_2, only the battery bank supplies energy to the motor. By conducting both S_1 and S_2, the generator

and battery bank supply energy to the motor at the same time. By controlling S_1 and S_2, three voltage levels can be achieved, which are V_1, V_2 and V_1+V_2, respectively. In the proposed topology, there are two demagnetization modes.

Fig.3-5 (a) presents a freewheeling mode, and Fig.3-5 (b) shows the case where energy recycles to the generator and battery bank.

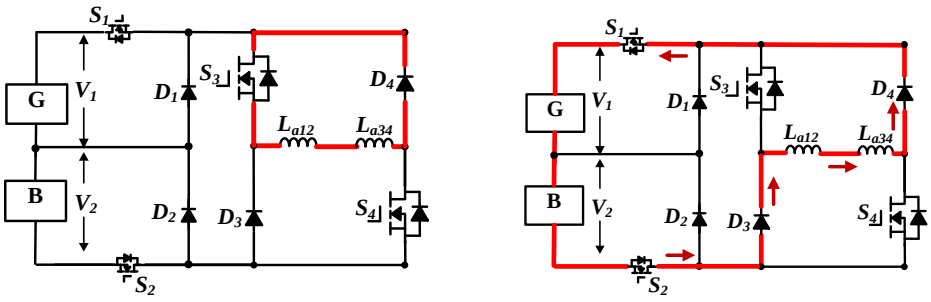

(a) (b)

Fig. 3-5. Demagnetization working states. (a) Freewheeling. (b) Energy recycling.

When an HEV is working in the standstill mode, the generator only needs to supply energy to the battery bank. The proposed converter works as a DC-DC converter. In Fig.3-6, switching on J_1, J_2 and J_3; for phase-A, S_1 and S_3 are turned on, and the generator charges SRM phase inductor, as illustrated in Fig.3-6 (a). Then, turn off S_1 and S_3, and turn on S_2 to discharge the energy in SRM phase inductance to the battery bank, as shown in Fig.3-6 (b).

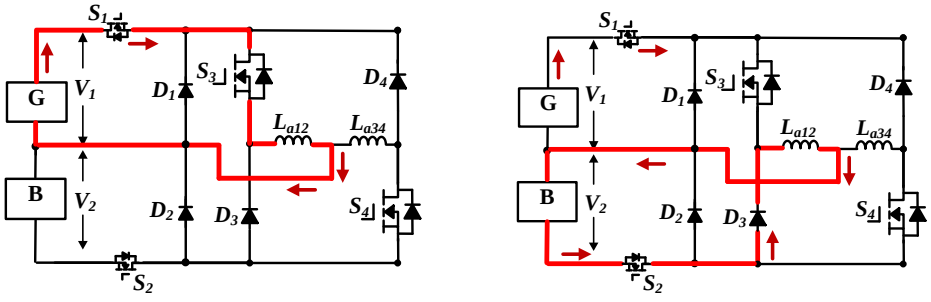

(a) (b)

Fig. 3-6. Working states under standstill condition. (a) G-B state 1. (b) G-B state 2.

When the HEV is in the standstill mode, the battery bank supplies energy to the generator/starter to start the ICE. There are two working states in this progress. In Fig.3-7, switching on J_1, J_2 and J_3; for phase-A, by turning on S_2 and S_4, the battery bank charges SRM

phase inductor, as illustrated in Fig.3-7 (a); and then, turn off S_2 and S_4, turn on S_1 to make the SRM phase inductance discharge energy to the generator, whose working state is shown in Fig.3-7 (b).

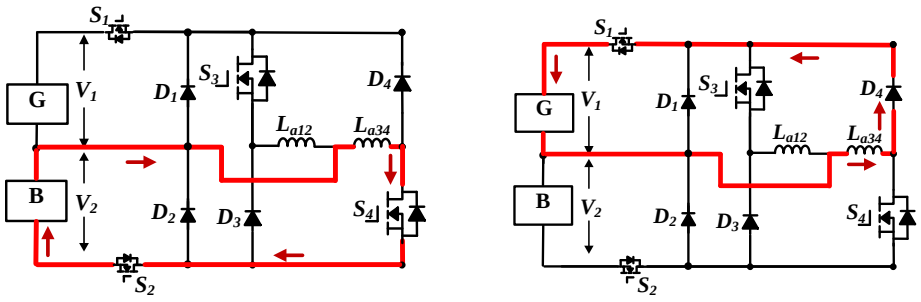

(a) (b)

Fig. 3-7. Energy supply to generator working states. (a) B-G state 1. (b) B-G state 2.

All the six power flow modes shown in Fig.3-1 can be realized in the working states discussed above. The following chapter will illustrate the control strategies for the six power flow modes.

3.2.3 Battery Bank Charging

The battery bank can be charged in driving and standstill conditions. When the vehicle is in the driving condition, only the generator is employed to excite the windings of SRM, as shown in Fig.3-4 (a). During the demagnetisation process, the battery bank can be charged, and the corresponding state is shown in Fig.3-5 (b). When the vehicle is in the standstill condition, the winding of SRM and the drive circuit will work as a DC-DC converter to transfer the power from the generator to the battery; the corresponding working states are presented in Fig.3-6 (b).

3.3 Control Strategy for the Proposed Tri-port Converter

As mentioned in Fig.3-1, there are six energy flow modes. Among these energy flow modes, there are two categories. The first one is the two-port energy flow mode, including G-M, B-M, B-G and G-B. The second one is the three-port energy flow mode, where G-B-M and M-G-B belong to this mode.

3.3.1 Two-port Energy Flow Condition

a) Control strategy for driving mode

G-M and B-M are the driving modes under two-port flow condition. When the proposed multi-port converter is in SRM driving mode, the system topology is equivalent to the traditional SRM driving topology; the voltage-PWM control and Current Chopping Control (CCC) are adopted as the two basic control schemes. According to the given speed ω^*, the controller works in CCC mode under low-speed conditions, and it works in voltage-PWM control mode under high-speed conditions. The whole control block diagram is presented in Fig.3-8. The classical Proportional-Integral (PI) is used in the speed controller, which is used to regulate the SRM speed. The encoder gives the SRM rotor position information, and the corresponding motor speed can be calculated by using a micro-controller. In the CCC strategy, the phase current is the control variable. The phase currents are measured by current sensors, and the current reference (i^*) is derived from the speed controller. The hysteresis controller is employed to generate the driving signals for the switching devices. In the voltage-PWM control system, the phase voltage is the control variable. According to the speed error, the effective phase voltage is controlled by the duty ratios of switching the devices.

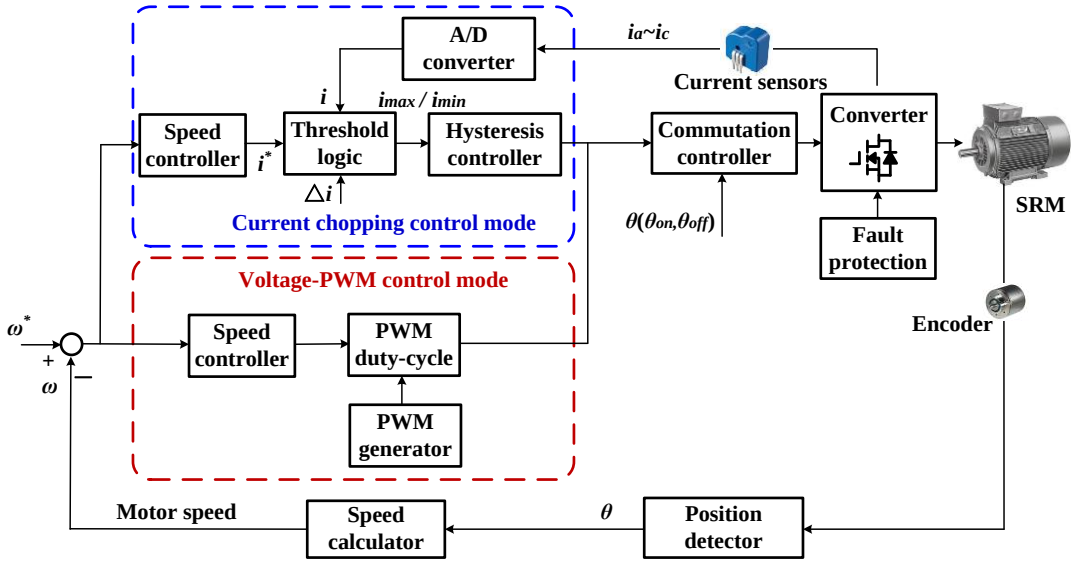

Fig. 3-8. SRM control strategy under driving mode.

b) Control for standstill energy exchange

Both B-G and G-M are included in the standstill energy exchange mode. When HEV is in the standstill battery charging mode (G-B) or standstill generator starting mode (B-G), the proposed tri-port converter needs to operate as a DC-DC converter to transfer energy from one

component to the others. In order to achieve a high-power level, the three phases operate in the parallel mode. Fig.3-9 indicates the control block scheme. Fig.3-9 (a) illustrates the control block diagram of battery bank supplying energy to the generator. Fig.3-9 (b) illustrates the standstill battery charging control block diagram.

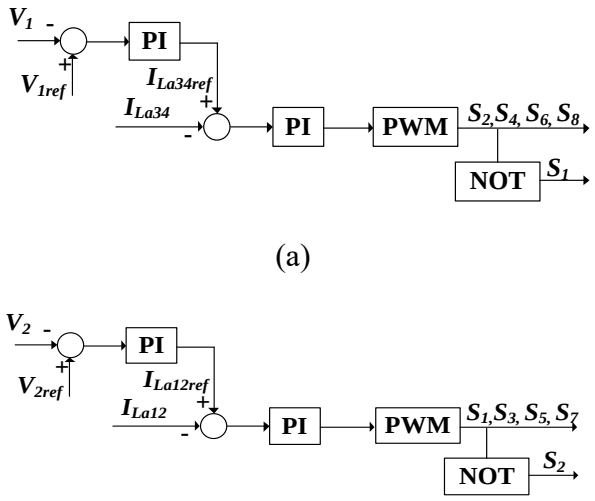

Fig. 3-9. HEV standstill energy exchange control. (a) Control diagram for HEV standstill generator starting. (b) Control diagram for HEV standstill battery charging.

3.3.2 Three-port Energy Control Strategy

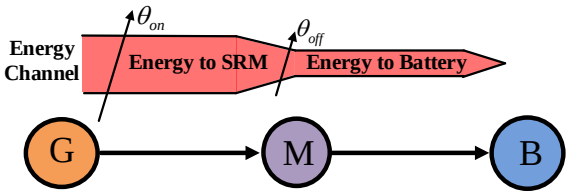

Fig. 3-10. Control strategy for three-port (G-M-B) energy exchange.

When applying G-B-M, the generator output energy and the motor and battery bank input energy exists in both the battery charging and generator starting modes, where the energy is decoupled by SRM. The turn-on angle θ_{on} and turn-off angle θ_{off} of phase converter can be employed as the control variables to achieve energy control under the situation of energy decoupling. The other type of three-port energy flow is M-B-G that possesses the same state of energy recycling of the phase current as shown in Fig.3-10.

3.4 Fault Tolerance Control with Proposed Multi-port Converter

Under the harsh application condition of EV and HEV, the SRM driving system is prone to fault to errors such as open circuit or short circuit of switching devices and phase windings. In a traditional three-phase asymmetrical half-bridge topology, when one of the components is in open circuit, the faulty bridge arm cannot work, and the whole converter is under the phase absence working condition. The corresponding torque ripple will increase obviously. By contrast, the proposed converter has fault tolerance characteristics that can realize fault tolerant operations. The proposed converter can block both the short-circuit and open-circuit points.

3.4.1 Fault Diagnosis and Fault Tolerance

Due to harsh operation conditions, the solid-state devices suffer from short-circuiting and open-circuit faults, as well as the phase windings. Fig.3-11 shows a typical example of single switch open-circuit fault (S_3 or S_4 malfunctions, while S_1 and S_2 are normal). By switching on J_1, the battery bank and the right part of the faulty phase converter form a new converter to achieve fault tolerance operation when the left part of the converter fails. The corresponding operation states are shown in Fig.3-11 (b) and (c). In Fig.3-11 (b), switching on S_2 and S_4, in this state, the phase winding L_{a34} is excited (energy flows from B to M). The energy recycling loop is presented in Fig.3-11 (c), in which S_4 is turned off, and the energy in L_{a34} is recycled to the generator (energy flows from M to G). By forming the fault tolerance topology, the faulty part can be blocked.

Similarly, when the defective phase converter is with the open-circuit fault in the right part, as shown in Fig.3-11 (d), by switching on relay J_1, the fault tolerance topology can be formed. The corresponding fault tolerance working states are presented in Fig.3-11 (e) and (f). In Fig.3-11 (e), switching on S_3, in this state, the phase winding L_{a12} is excited and produces a torque. The energy recycling loop is presented in Fig.3-11 (f), in which S_3 is turned off, S_2 is turned on, and the energy in L_{a12} is recycled to the generator. In the fault tolerance topology, the switching devices S_1 and S_2 can be turned on all the time, which will not influence the power supply to healthy phases. Since the proposed fault tolerance can block the faulty part, the fault tolerance topology under short-circuit fault is the same as that under open-circuit failure. Therefore, in terms of the fault diagnosis strategy, only the fault location information is needed.

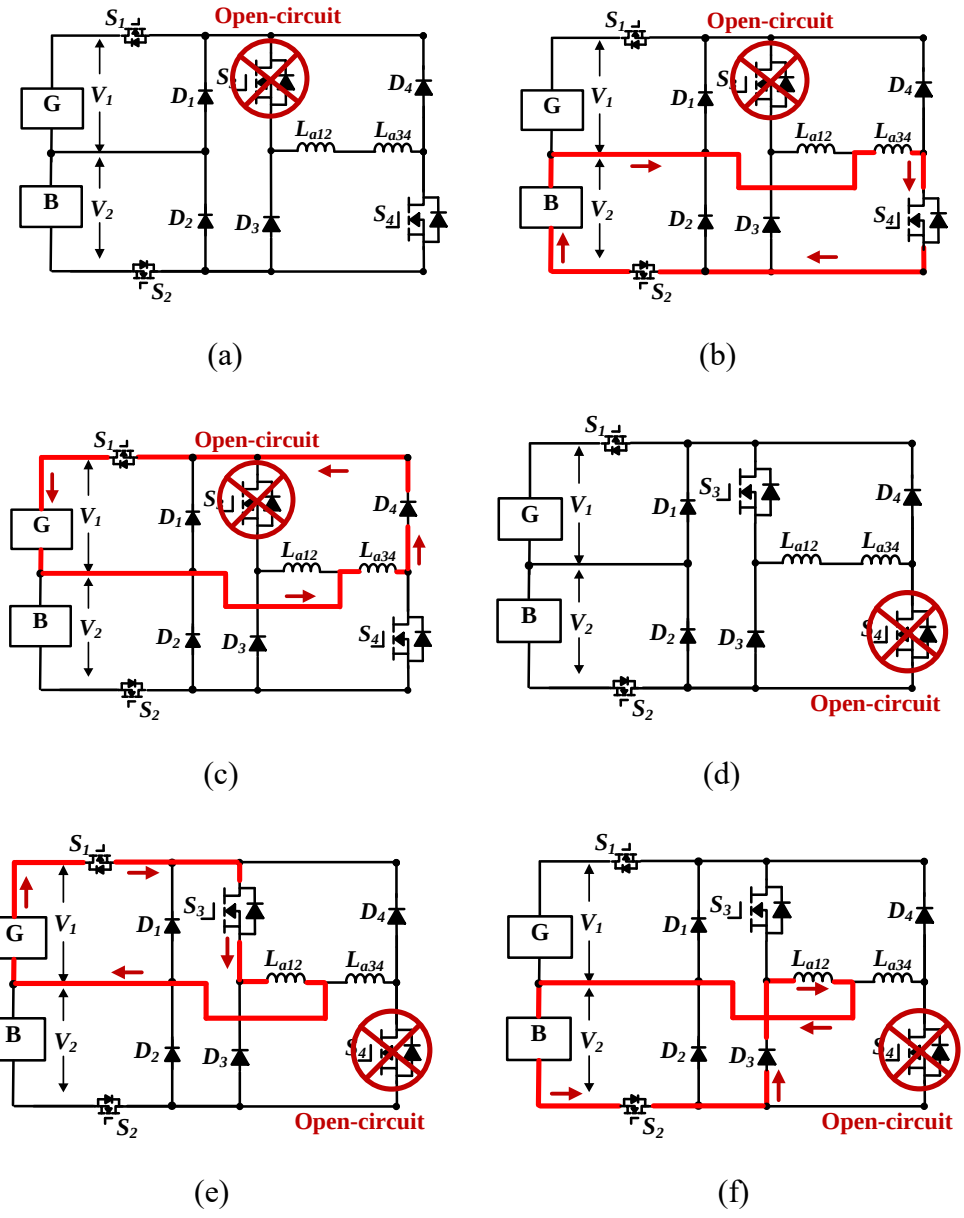

Fig. 3-11. Fault tolerance operation. (a) Left part open-circuit fault. (b) Left part fault tolerance under working state 1. (c) Left part fault tolerance working state 2. (d) Right part open-circuit fault. (e) Right part fault under working state 1. (f) Right part fault under working state 2.

The fault diagnosis flowchart for one phase is presented in Fig.3-12. As illustrated in Fig.3-12, when the phase-A current is always equal to or over zero, by switching on J_1 and switching off S_3, if there is a current in phase A, or the phase-A current can decrease to zero, the left part is faulty. Otherwise the right part of the fault is encountered. Since each phase converter operates independently, the fault diagnosis strategy and fault tolerance operation can also be applied in

other phases. For switching devices S_1 and S_2, the press pack switching devices can be employed. When press pack switching devices under fault condition are equivalent to a short circuit, the power supply will not be influenced.

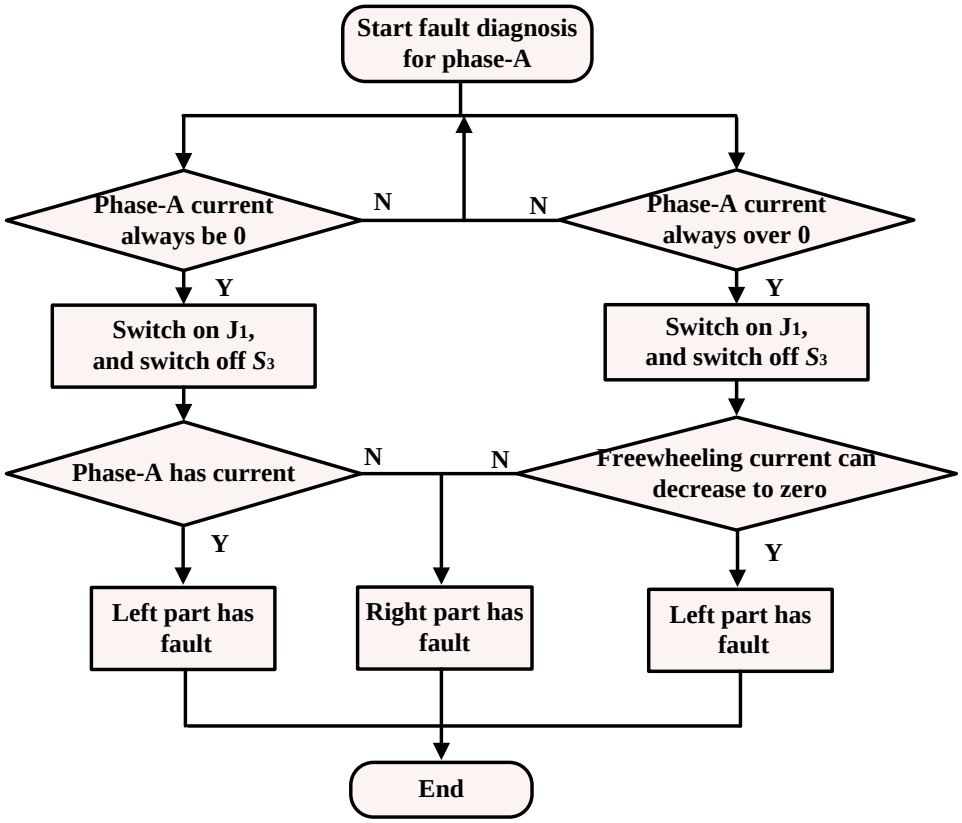

Fig. 3-12. SRM control strategy under driving mode.

3.4.2 SRM Modelling Under Fault Tolerance Operation

Under normal operations, the phase voltage balance is given by:

$$\pm U_{dc} = Ri + L(\theta)\frac{di}{dt} + i\omega\frac{dL(\theta)}{d\theta} \tag{3.1}$$

where U_{dc} is the phase voltage of SRM, R is the SRM phase resistance, L is the phase inductance, i is the SRM phase current, θ is the SRM rotor angular position, and ω is the SRM angular speed. Due to the dual salient structure, the SRM phase inductance changes with the rotor position.

The SRM electromagnetic torque can be written as:

$$T_e = \sum_{k=1}^{m} T_k = \sum_{k=1}^{m} \frac{1}{2} i_k{}^2 \frac{dL_k(\theta)}{d\theta} \tag{3.2}$$

where m is the motor phase, T_k is the phase instantaneous electromagnetic torque.

The mechanical motion equation of the SRM is given by:

$$J \frac{d\omega}{dt} + B\omega = T_e - T_l \tag{3.3}$$

where J is the combined moment of inertia of the motor and load, B is the combined friction coefficient of the motor and load, and T_l is the load torque.

When faults (open-circuit or short circuit) occur to the SRM drive system in solid state devices or phase windings, the fault tolerance strategy will be triggered. By using the proposed fault tolerance operation strategy, the converter can operate with a half part of the faulty phase winding, then:

$$\begin{cases} L_{\max}{}' = \frac{1}{2} L_{\max} \\ L_{\min}{}' = \frac{1}{2} L_{\min} \end{cases} \tag{3.4}$$

where $L_{\min}'$ and $L_{\max}'$ are the minimum and maximum inductances of the faulty phase; $L_{\min}$ and $L_{\max}$ are the minimum and maximum inductances of the healthy phase. The slope factor of phase inductance in the inductance ascending region in fault-tolerant operation is:

$$K_L{}' = \frac{1}{2} \frac{L_{\max}{}' - L_{\min}{}'}{\theta_2 - \theta_1} = \frac{1}{2} K_L \tag{3.5}$$

where θ_1 and θ_2 are the corresponding rotor positions; K_L and K_L' are the phase inductance slope factors in healthy and fault-tolerant operation states, respectively.

In the current-ascending region, the phase current slope in fault-tolerant operation is:

$$K_i' = \left(\frac{di}{d\theta}\right)' = \frac{U_{in}}{\omega_r \frac{1}{2} L_{\min}} = \frac{2U_{in}}{\omega_r L_{\min}} = 2K_i \tag{3.6}$$

where K_i and K_i' are the phase current slope factors in the healthy and fault-tolerant operation conditions, respectively. The peak value of phase current in fault-tolerant operation is:

$$i_{max}' = \frac{U_{in}}{\omega_r} \frac{\theta_1 - \theta_{on}}{\frac{1}{2} L_{\min}} = \frac{U_{in}}{\omega_r} \frac{2(\theta_1 - \theta_{on})}{L_{\min}} = 2i_{max} \tag{3.7}$$

where i_{max}' and i_{max} are the peak values of phase current in healthy and fault-tolerant operation states, respectively; θ_{on} is the turn-on angle; θ_1 is the position where the phase current reaches its peak value.

The SRM average electromagnetic torque of the faulty phase is given by:

$$T_{av}' = \frac{N_r}{2\pi} \frac{{U_{in}}^2}{\omega_r^2} \left(\theta_{off} - \theta_1\right) \left(\frac{\theta_1 - \theta_{on}}{\frac{1}{2} L_{\min}} - \frac{1}{2} \cdot \frac{\theta_{off} - \theta_1}{\frac{1}{2} L_{\max} - \frac{1}{2} L_{\min}} \right) = 2T_{av} \tag{3.8}$$

where N_r is the number of rotor poles, and T_{av} and T_{av}' are the phase average electromagnetic torques in healthy and fault-tolerant operation conditions, respectively.

According to (3.7) and (3.8), the current peak value and the average electromagnetic torque of the faulty phase in fault-tolerant operations are twice the value as in healthy conditions. However, in a closed-loop system, due to a constant load, the total average electromagnetic torque of SRM is the same as that in normal conditions.

By using the proposed fault tolerance strategy in CCC mode, the faulty part of the phase converter can be blocked, and the healthy part can still be employed for torque output. Since the controlling phase current is the target in the CCC mode, the phase current will be regulated to the same reference value as that of the healthy phase. By using the proposed fault tolerance strategy in voltage-PWM control mode, the phase voltage is to be controlled. Aiming at lowering the unbalanced phase current, the turn-on angle of the faulty phase can be adjusted to

reduce the influence of unbalanced phase current in the faulty winding. Therefore, the proposed tri-port converter can be employed to compensate and balance the current and torque; the torque ripple can also be reduced to improve the SRM drive performance under faulty conditions.

In the open-circuit condition, only half the phase winding can be employed to generate torque that will decrease the output torque of SRM in heavy load condition. However, CCC can enable the performance of the fault tolerance operation to be the same as the desirable conditions when the load is light.

3.5 Simulation and Experimental Verifications

In order to validate the proposed tri-port converter for an SRM based HEV, simulation studies and experiments are adopted to verify the proposed topology. A 750W 12/8 SRM with the proposed tri-port converter is modelled in Matlab/Simulink. Fig.3-13 presents the simulation results in the voltage-PWM control mode at 500 r/min under normal, power source switching, faulty and fault-tolerant conditions. The turn-on angle of SRM is 0°, and the turn-off angle of SRM is 20°, and the load torque is 1 N·m. In the waveforms, T and T^* are the instantaneous torque and given load torque, respectively; i_a, i_b, and i_c represent the three-phase currents, respectively. In the normal state, the three-phase currents have the same shape with a 15° phase-shift from each other, and the total torque is the sum of the three-phase torques, as shown in Fig.3-13 (a). Fig.3-13 (b) shows the power source switching conditions that switch from the battery bank power supply to battery bank and generator supply. The motor system operates steadily when the power supply changes from the battery to the dual-source. Fig.3-13 (c) illustrates the faulty condition of SRM, in which phase-A suffers from an open-circuit fault, and the phase current reduces to zero. Due to the independence of each phase, the other normal phases will not be affected by the faulty phase. While by increasing the PWM duty-cycle, the currents in the other healthy phases are excited to and bumped to compensate the torque loss. However, due to the absence of phase-A torque, the torque ripple is increased compared to normal conditions, as presented in Fig. 3-13 (c). Fig. 3-13(d) shows the voltage-PWM control mode under fault tolerance control in faulty conditions. The relay J_1 is switched on when an open-fault is detected in the upper-switch S_1. By passing the phase-A winding L_{a12}, L_{a34} still

can be employed for fault tolerance control under this condition, and the torque ripple is obviously reduced compared to that of Fig. 3-13 (c).

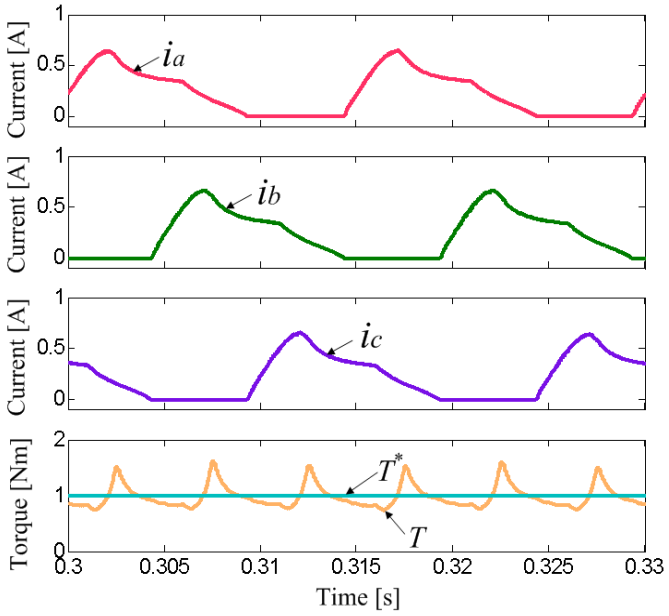

(a)

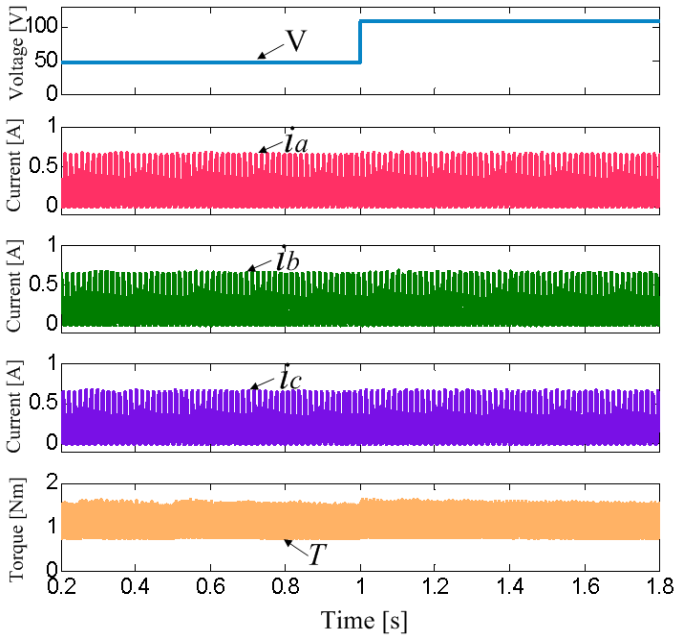

(b)

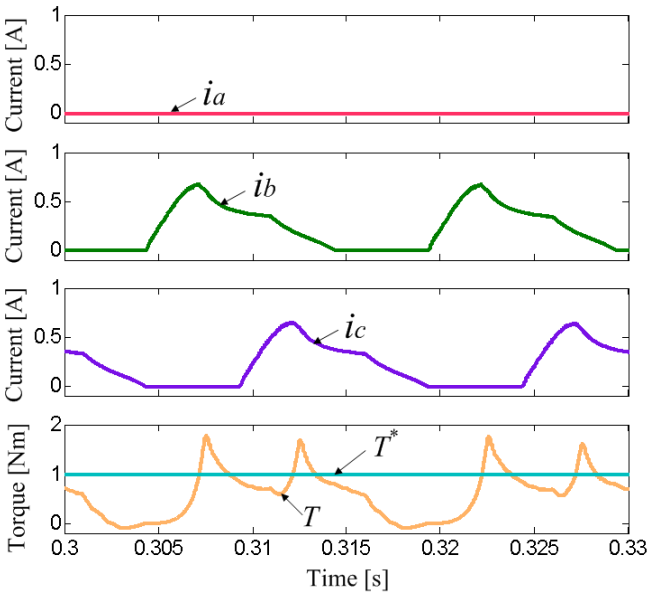

(c)

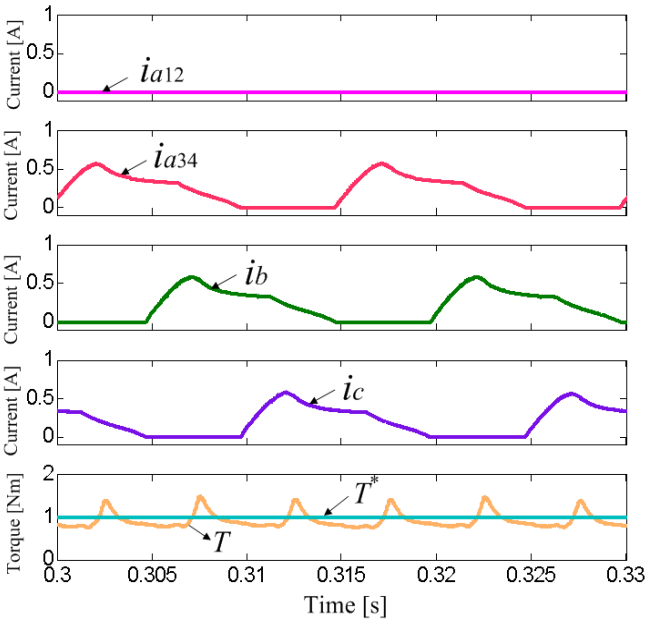

(d)

Fig. 3-13. Simulation results in voltage-PWM control mode. (a) Normal. (b) Power source switching. (c) Open fault. (d) fault-tolerance.

Fig. 3-14 shows the CCC mode under normal, power supply switching fault and fault-tolerant conditions. In Fig.3-14 (a), the torque ripple is smaller than that of voltage-PWM control mode in the normal condition. Fig.3-14 (b) shows the simulation results in power source exchange

conditions. When the power supply changes from the battery to the dual-source in this control mode, the SRM system still operates steadily without noticeable fluctuation. The torque ripple is increased obviously under faulty conditions, which is similar to the voltage-PWM control mode, as shown in Fig.3-14 (c). Fig.3-14 (d) presents the fault tolerance that results in CCC mode at 500 r/min. The torque ripple is obviously reduced to the normal state as compared to Fig.3-14 (c) by using the proposed topology.

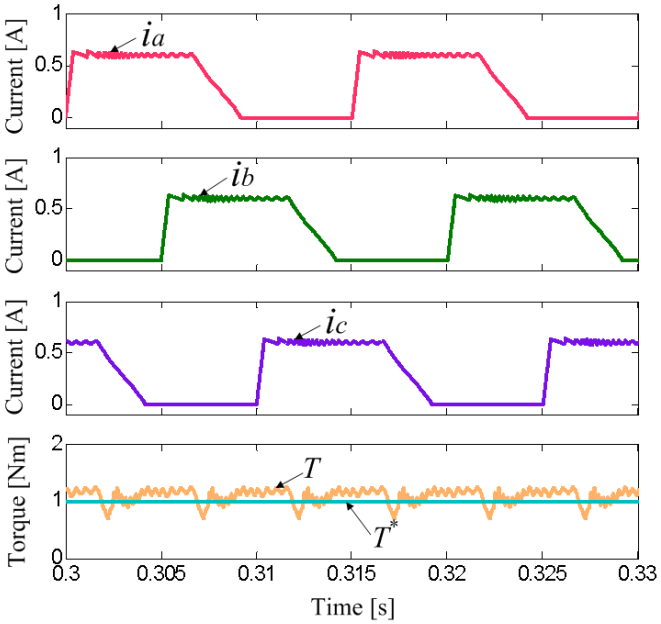

(a)

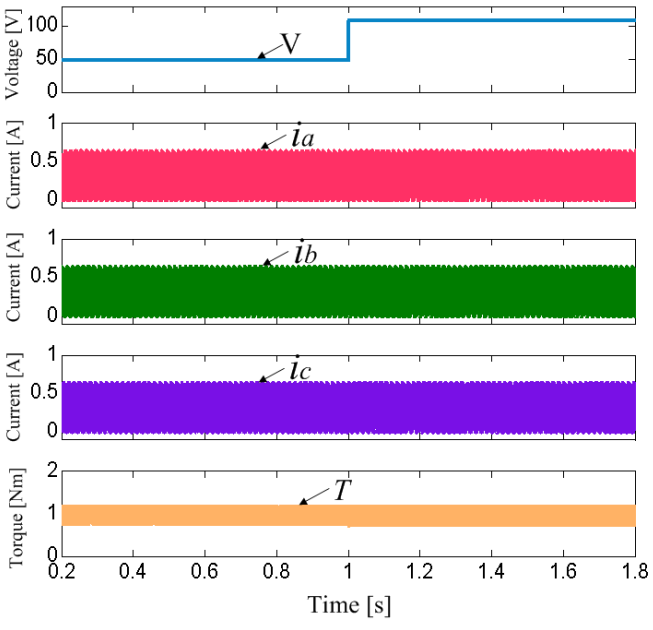

(b)

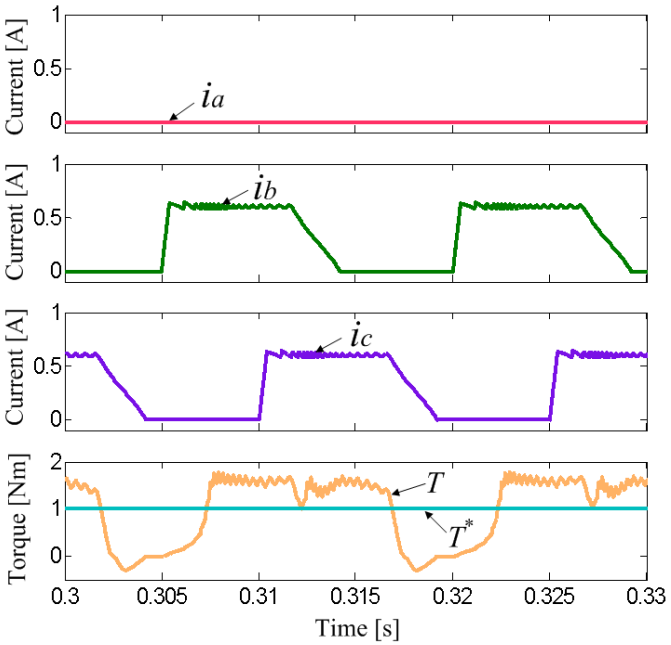

(c)

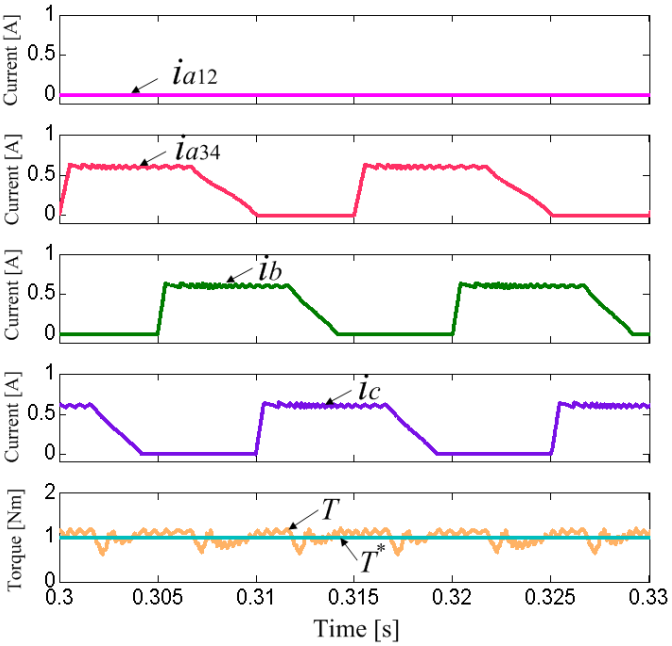

(d)

Fig. 3-14. Simulation results in current regulation mode. (a) Normal. (b) Power source switching. (c) Open fault. (d) fault-tolerance.

To verify the effectiveness of the proposed tri-port converter for HEV, an experimental rig for

testing a three-phase 12/8 prototype SRM driving system was built, as presented in Fig.3-15. Table 3-1 provides the main motor parameters. The central tapped winding nodes are created and pulled out at the terminals when manufacturing the prototype motor. In the experiment rig, the solid-state devices types are FDA59N30 for MOSFET and IDW75E60 for diode. A dSPACE 1006 platform is adopted to actualise the control algorithm. A magnetic brake is used as the load with 1 N·m torque. An 80 V dc power supply and a 48 V lead-acid battery are employed in the motor drive.

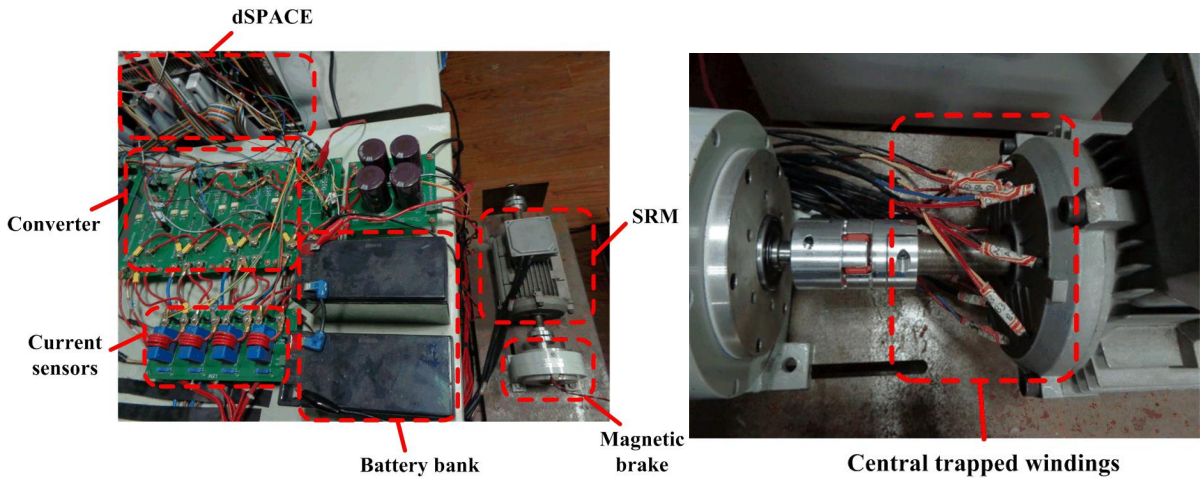

Fig. 3-15. Experimental setup.

TABLE 3-1
SRM Parameters

Parameters	Value	Parameters	Value
Phase number	3	Rotor outer diameter (mm)	55
Stator poles	12	Rotor inner diameter (mm)	30
Rotor poles	8	Stator outer diameter (mm)	102.5
Rated speed (r/min)	1500	Stator inner diameter (mm)	55.5
Rated power (W)	750	Core length (mm)	80
Phase resistor (Ω)	3.01	Stator arc angle	14°
Minimum phase inductance (mH)	27.2	Rotor arc angle	16°
Maximum phase inductance (mH)	256.7		

Fig.3-16 and Fig.3-17 present the experimental results of the three-phase 12/8 SRM at 500 r/min, where the turn-on angle is 0°, and the turn-off angle is 20°. Fig.3-16 (a) shows the experiment results in power source exchange conditions when the power supply changes from the battery to the dual sources. The motor system also operates steadily with limited fluctuations. When SRM is under a desirable condition, three-phase currents are with the same shape and amplitude, as shown in Fig.3-16 (b). When the SRM driving system is under one phase open-circuit fault without fault tolerance control, there is no current in the faulty phase. As illustrated in Fig.3-16 (c), the healthy phase currents are larger than the previous one. Due to the absence of phase A, the output torque is larger than that in the normal condition. A large torque ripple increases the mechanical vibration that may decrease the whole power train system reliability. Fig.3-16 (d) verifies the fault tolerance strategy under one phase fault condition. By employing a half part of phase-A winding, the operation of absent phase can be avoided, and the SRM output torque ripple can be noticeably decreased.

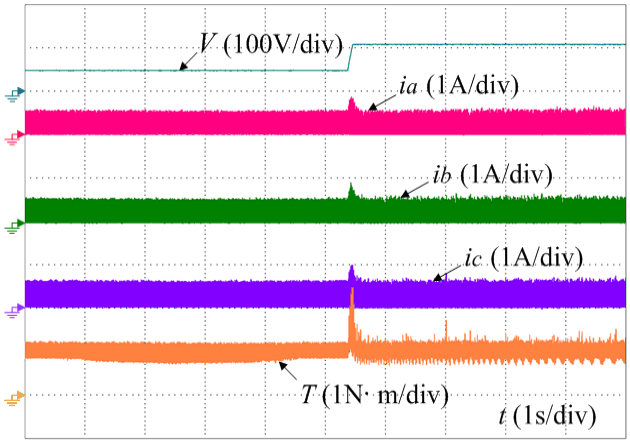

(a)

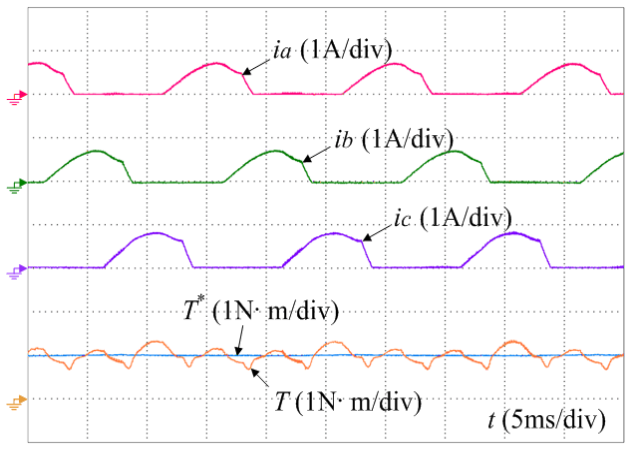

(b)

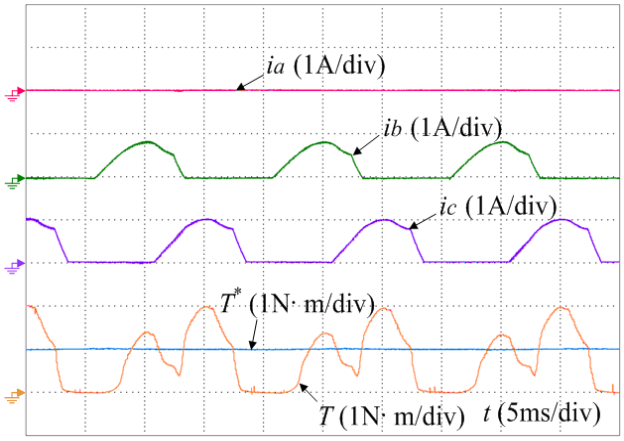

(c)

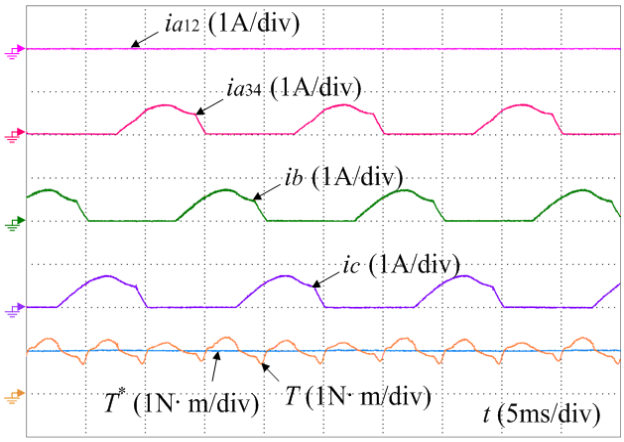

(d)

Fig. 3-16. Experimental results in voltage-PWM control mode. (a) Power source exchange. (b) Normal. (c) Open fault. (d) fault-tolerance.

Fig.3-17 presents the typical waveforms for the CCC system under normal, faulty and fault-tolerant conditions. When the power supply changes from the battery to the dual-source, the motor system still can be easily controlled without significant fluctuations, as shown in Fig.3-17 (a). Fig.3-17 (b) demonstrates the experimental waveforms under reasonable conditions. In the open-circuit fault condition, there is no current in the faulty phase, and the torque ripple increases significantly, as shown in Fig.3-17 (c). By utilising the proposed topology and the fault tolerance strategy, the faulty phase can still work and follow the reference current as the healthy phases under the CCC mode, as illustrated in Fig.3-17 (d).

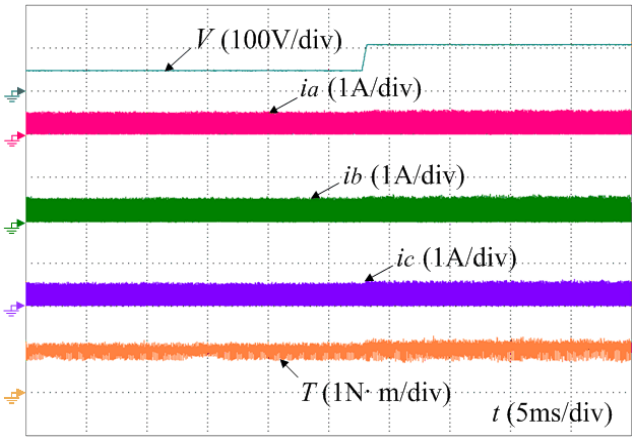
V (100V/div)
ia (1A/div)
ib (1A/div)
ic (1A/div)
T (1N· m/div)
t (5ms/div)

(a)

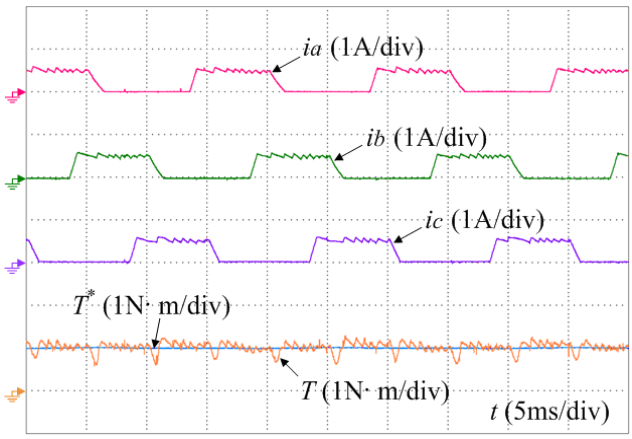
ia (1A/div)
ib (1A/div)
ic (1A/div)
T* (1N· m/div)
T (1N· m/div)
t (5ms/div)

(b)

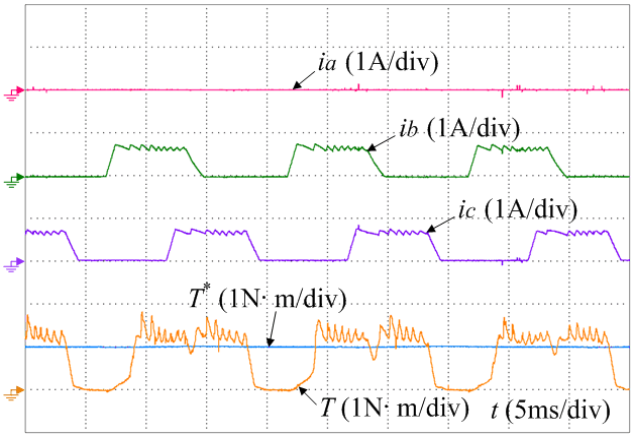
ia (1A/div)
ib (1A/div)
ic (1A/div)
T* (1N· m/div)
T (1N· m/div)
t (5ms/div)

(c)

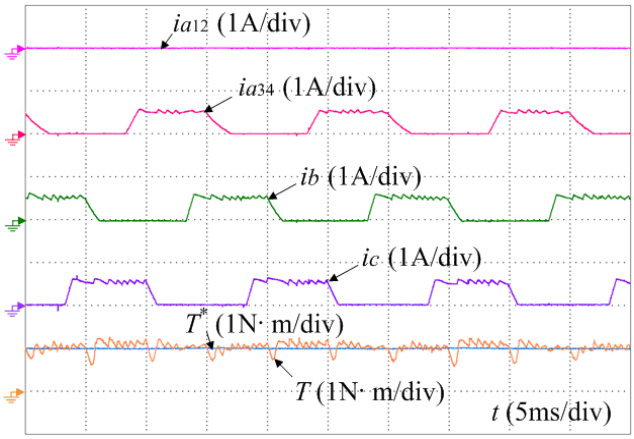

(d)

Fig. 3-17. Experimental results in current regulation control mode. (a) Power source exchange. (b) Normal. (c) Open fault. (d) fault-tolerance.

The proposed fault tolerance scheme can also perform optimally under heavy load conditions, as shown in Fig.3-18. When SRM works at 500 r/min with the load of 5 N·m, Fig.3-18 (a) displays the fault tolerance operation waveforms in the voltage-PWM control mode under phase-A open-circuit fault. The faulty part of the phase converter is blocked (i_{a12}=0), while the healthy part of the phase converter is still functional. By adjusting the turn-on angle, the current i_{a34} has the same amplitude as that in the normal phase. Fig.3-18 (b) is the fault tolerance operation waveform in the CCC control mode under phase-A open-circuit fault condition. By CCC, i_{a34} has the same amplitude as that in the normal phase. According to the waveform of output torque, the proposed fault tolerance control can successfully limit the torque ripple.

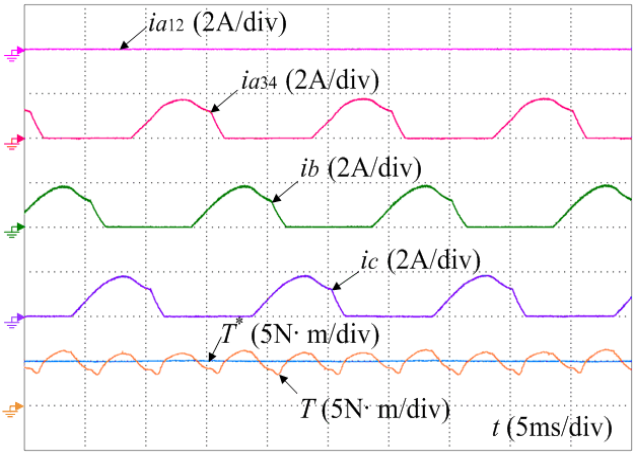

(a)

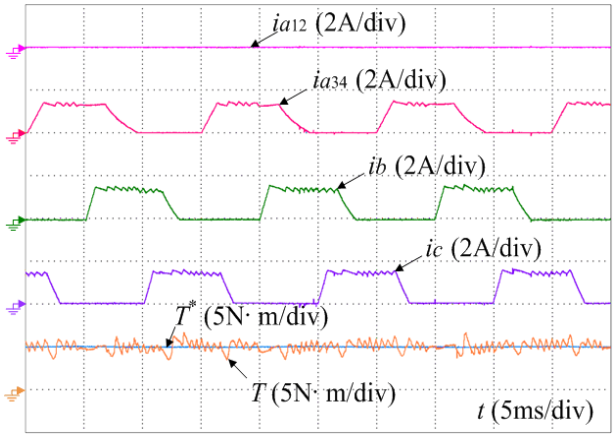

(b)

Fig. 3-18. Experimental results under heavy load. (a) Voltage-PWM control mode. (b) CCC mode.

Fig.3-19 illustrates the operation of the proposed SRM driving system during acceleration, high-speed operation and load increasing with 1 N·m load. As shown in Fig.3-19(a), the real-time speed responds to the command instantly when the speed increases. The proposed fault tolerance strategy can still work for the proposed tri-port converter, as shown in Fig.3-19(b). Fig.3-19(c) presents the transient process in the load increasing condition, and the speed are controllable with input command values.

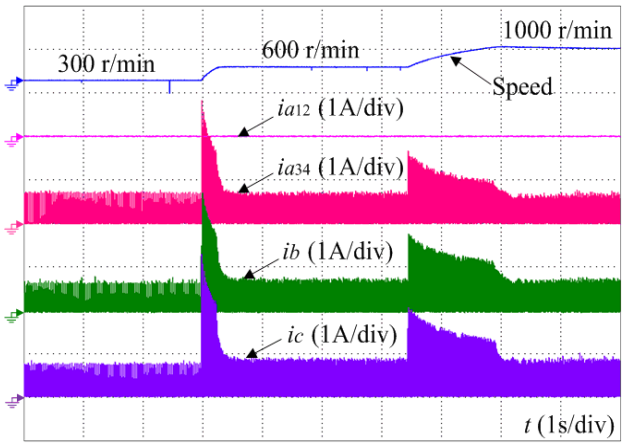

(a)

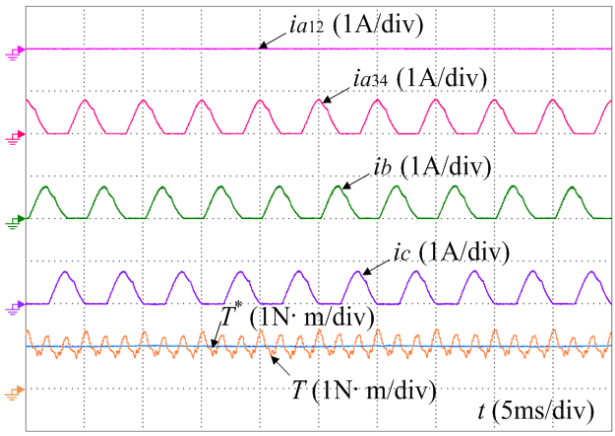

(b)

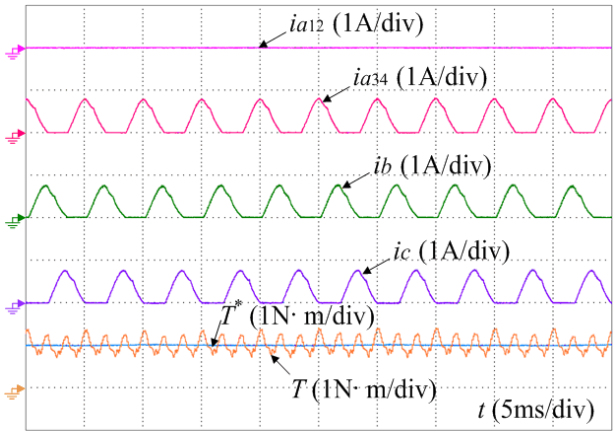

(c)

Fig. 3-19. Experiment results of fault-tolerant operation. (a) Acceleration. (b) High-speed operation. (c) Load increasing.

Fig.3-20 shows the experiment results of the generator supplying energy to the battery bank, in which $i_{battery}$ is the battery bank charging current, P_z stands for the position sensor signal. Three-phase windings are employed to improve charging power. As shown in Fig.3-20, P_z is zero during the charging progress, indicating that the SRM is in the standstill condition.

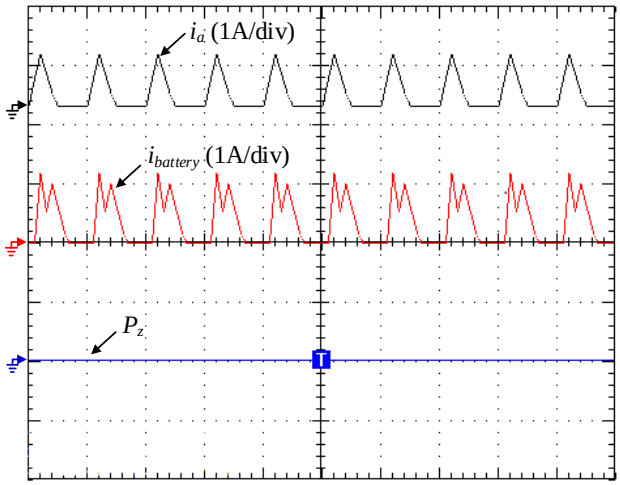

Fig. 3-20. Generator charging battery bank.

3.6 Summary

This chapter has proposed a tri-port converter with modular and concise structure to combine a generator, a battery bank and an SRM in one converter. The corresponding working modes, control strategy and fault tolerance operation were also investigated. This topic is related to the safety and reliability of normal working vehicles; thus, it plays a significant role in preventing complications. By deploying the proposed tri-port converter for SRM based HEV system, the topology with a modular structure can be massively produced and supports all the six working modes in one converter. Furthermore, the proposed system also can support fault diagnosis and fault-tolerant operation to improve the system safety level. In more-electric ships and aero-planes, the proposed tri-port converter also can be applied to achieve high power density, high reliability and flexible energy flow.

3.7 References

[1] J. Ye, B. Bilgin, and A. Emadi, "An extended-speed low-ripple torque control of switched reluctance motor drives," *IEEE Trans. Power Electron.*, vol. 30, no. 3, pp. 1457-1470, Mar. 2015.

[2] S. Wang, Q. Zhan, Z. Ma, and L. Zhou, "Implementation of a 50-kW four-phase switched reluctance motor drive system for hybrid electric vehicle," *IEEE Trans. Magn.*, vol. 41, no. 1, pp. 501-504, Jan.

2005.

[3] J. Liang, D. H. Lee, G. Xu, J. W. Ahn, “Analysis of passive boost power converter for three-phase SR drive,” *IEEE Trans. Industrial Electronics*, vol. 57, no. 9, pp. 2961-2971, Sep. 2010.

[4] A. G. Jack, B. C. Mecrow, and J. A. Haylock, “A comparative study of permanent magnet and switched reluctance motors for high-performance fault-tolerant applications,” *IEEE Trans. Ind. Appl.*, vol. 32, no. 4, pp. 889-895, Jul/Aug. 1996.

[5] Chai Feng, Pei Yulong, Li Xinmei, Guo Bin, and Cheng Shukang, “The Performance Research of Starter-Generator Based on Reluctance Torque Used in HEV,” *IEEE Trans. Magn.*, vol. 45, no. 1, pp. 635-638, Jan, 2009.

[6] Y. Hu, X. Song, W. Cao, and B. Ji, “New SR drive with integrated charging capacity for plug-in hybrid electric vehicles (PHEVs),” *IEEE Trans. Industrial Electronics*, vol. 61, no. 10, pp. 5722-5731, Oct. 2014.

[7] C. Hung-Chun, and L. Chang-Ming, “An integrated driving/charging switched reluctance motor drive using three-phase power module,” *IEEE Trans. Ind. Electron.*, vol. 58, no. 5, pp. 1763-1775, May 2011.

[8] L. Jianing, L. Dong-Hee, X. Guoqing, and A. Jin-Woo, “Analysis of passive boost power converter for three-phase SR drive,” *IEEE Trans. Ind. Electron.*, vol. 57, no. 9, pp. 2961-2971, Sep. 2010.

[9] M. Barnes, and C. Pollock, “Forward converters for dual voltage switched reluctance motor drives,” *IEEE Trans. Power Electron.*, vol. 16, no. 1, pp. 83-91, Jan. 2001.

[10] W. K. Thong, and C. Pollock, “Low-cost battery-powered switched reluctance drives with integral battery-charging capability,” *IEEE Trans. Ind. Appl.*, vol. 36, no. 6, pp. 1676-1681, Nov./Dec. 2000.

[11] D. H. Lee, and J. W. Ahn, “A novel four-level converter and instantaneous switching angle detector for high speed SRM drive,” *IEEE Trans. Power Electron.*, vol. 22, no. 5, pp. 2034-2041, Sep. 2007.

[12] L. Dong-Hee, and A. Jin-Woo, “A novel four-level converter and instantaneous switching angle detector for high speed SRM drive,” *IEEE Trans. Power Electron.*, vol. 22, no. 5, pp. 2034-2041, Sep. 2007.

Chapter 4 Analysis and Suppression Approaches of Uncontrolled Generation for PMSM based Battery EVs

As is demonstrated in Chapter 2, nowadays, the PMSM-based battery EVs are accounting for a large market share as well, so it is significant to investigate this hot spot. In order to enhance the safety level of this type of vehicles, this chapter analyses the UCG problem which occurs in the EV post-fault conditions. It is seldom discussed previously but closely related to the health of the electrical components in the powertrains and system safety. IPMSMs should work under flux weakening state in electrical vehicles for high speed. But inevitable faults such as overcurrent might occur when the motors rotate over high speed range, causing UCG phenomenon. In the process, large current might be generated and then flow back to the battery through the UR, posing a great risk to the power devices. For better understanding of UCG, this chapter firstly explains the transient process by establishing a dynamic model of the UR. Then, aiming at the steady-state generating stage, an enhanced UCG model is proposed for the analysis of motor parameter dependencies. Because it is found that the maximum UCG feedback current at high speed is inversely proportional to the *d*-axis inductance, an inductance design/optimization method for appropriate *d*-axis by changing the rotor structure is developed to attenuate the side effect of UCG. The proposed UCG model and the validity of the design/optimization approach are verified by experiments. These provide guidelines for the IPMSM design process.

4.1 Introduction

As is widely acknowledged, the constant-power speed ratio (CPSR) of IPMSM can reach a value of ten by adjusting the machine parameters (e.g., magnetic saliency ratio and permanent magnet flux) [1], resulting in that they can satisfy the requirements of wide speed regulation range for EV applications [2-18]. The simplified schematic diagram of the battery EV without

converter connecting the battery bank and the inverter is shown in Fig.4-1 (a). When the motor is controlled by a typical flux-weakening algorithm to operate at the situation in which the shaft speed considerably exceeds the corner speed, unavoidable faults (overvoltage and overcurrent, etc.) are more inclined to arise [19-21]. Practically, this will trigger the system protection mechanism and propel the transistors (T_1, T_2, …., T_6) in the inverter to "shut down" immediately. Then the air-gap magnetic field recovers promptly, leading to extremely high amplitude of back electromotive force (EMF). Because the battery internal resistance is small, large current flows back through the inverter freewheeling diodes (D_1, D_2, …., D_6) to battery until the rotor speed decreases to a threshold value [22-23]. That process is called uncontrolled generation (UCG). During UCG process, the system block diagram is illustrated in Fig.4-1 (b). Unfortunately, the large flowing-back current is feasible to ruin the inverter and influence the health state of the battery pack. Consequently, when designing an IPMSM drive system for EVs which require a wide range of constant-power operation, it would be highly desirable to get round the UCG phenomenon under any operating conditions if possible.

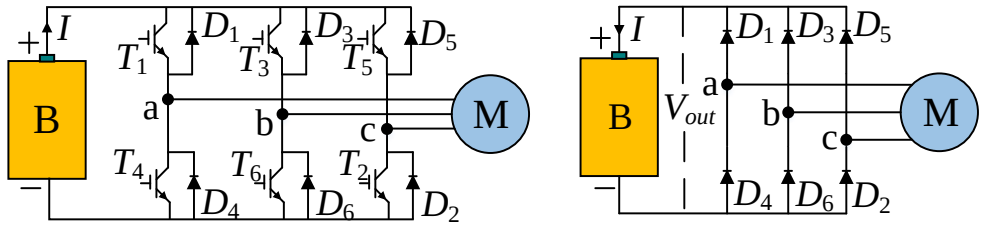

Fig. 4-1. (a) Schematic diagram of a typical EV drive system. (b) Schematic diagram of the drive system during UCG.

T. M. Jahns ever analyzed the UCG process. He assumed that the IPMSM currents shall remain sinusoidal and the resulting phase currents would be forced to be in phase with the corresponding terminal phase voltages, and further mocked up a normalized machine model under the *d*, *q* synchronous reference frame, obtaining the key performance characteristics and motor parameter dependencies related to UCG operating mode [24]. It is creative to present that the L_q/L_d inductance saliency ratio had tremendous impacts on the stator current and torque and predict hysteresis effect, but honestly, the conclusion requires to be discussed in depth because the value of *d*-, *q*-axis inductance might bring stronger influence to machine performance characteristics. More importantly, a third assumption that motor resistances are

so small to be ignored does not apply to EV drive systems where the load resistances (battery internal resistance) are low as well. Finally, this chapter will carry out experiments to study the current characteristics described but not testified in that work. C. Liaw reiterated and verified experimentally the hysteresis effect by using voltage-current loci rather than current-speed loci [25]. During the analysis, a simplified model which treated the rectifier and voltage source as a three-phase resistive load but irrationally ignored the DC voltage source was used to calculate operating currents and terminal voltages under different speed. The research undoubtedly put forward a practical modeling method, but it was utilized in a less precise way in the work. To be frank, the presence of hysteresis would not be highlighted if such a model were employed. What makes that research unique is that Liaw had planned to take advantage of UCG instead of keeping away from it because it was found that an IPMSM operating under UCG has potential to provide high output power. Those researches provide initial theoretical basis, but there exist some ameliorable aspects when analyzing UCG operation in EV drive systems.

Based on the above analysis of merits and defects, the first priority of this chapter is modeling more effectively, after which the switching process of intelligent power module (IPM) needs to be investigated for better understanding. That UCG leads to voltage and current "overshoot" makes it definitely necessary to take efficient measures to protect both battery and inverter from damage. Since the inverter transistors are completely inactive during the mode of operation, the peak current depends mainly on the machine parameters, the instantaneous speed and dc-link voltage. Instead of only pinpointing the correlation between saliency ratio and system performance characteristics, our research focuses on more parameters, such as *d*-, *q*-axis inductance, stator resistances, permanent magnet flux linkage and battery internal resistance. Analysis of parameter dependencies paves the way for motor parameter optimization. By choosing and designing appropriate IPMSM parameters, it is highly possible to minimize or eliminate the risks of undesired but occasionally unavoidable operating regime. In other words, those results have noteworthy implications for the design of IPMSM. This chapter exhibits pretty explicit procedures for machine design/optimization.

4.2 Modelling for UCG Analysis

As is shown in Fig.4-1 (b), three electrical parts work during the UCG process, namely, battery pack, UR and the machine. In order to analyse the properties of UCG, the system models require to be established.

4.2.1 Battery model

R_{int} model, also known as the internal resistance model, is a relatively simple battery model designed by Idaho National Laboratory [26]. It includes the output voltage V_{bat}, ideal voltage E_{bat} and internal resistor R_{bat}:

$$V_{bat} = E_{bat} + i \cdot R_{bat} \tag{4.1}$$

where i is the charge current.

4.2.2 Dynamic IPM Model

During UCG, the machine works as a generator and the terminal voltages are the input of the uncontrolled rectifier (UR) shown in Fig.4-1 (b). The working process of UR can be detailed as follows: whenever the line-to-line voltage (V_{ab}, V_{ac}, V_{ba}, V_{bc}, V_{ca}, V_{cb}) is greater than threshold voltage $2V_{on}+V_{bat}$, only a pair of diodes are switched on simultaneously and the output DC voltage of UR (V_{out}) equals the maximum one; if all six voltages are smaller than V_{bat}, no currents flow back to battery and V_{out} is equal to the battery output voltage. The dynamic IPM model can be expressed as follows:

$$V_{in} = \max(V_{ab}, V_{ba}, V_{ac}, V_{ca}, V_{bc}, V_{cb}) \tag{4.2}$$

$$\begin{cases} V_{out} = V_{in} - 2V_{on}, & if\,(V_{in} - 2V_{on}) > V_{bat} \\ V_{out} = V_{bat}, & if\,(V_{in} - 2V_{on}) \le V_{bat} \end{cases} \tag{4.3}$$

where V_{on} is the turn-on voltage of diode. Thanks to the model, we can gain better understanding of the switching process in detail.

4.2.3 Steady-state UCG Model Considering Machine

The steady-state UCG model used in [25] is assumed that the phase currents are sinusoidal, so that the IPMSM can be totally regarded as a generator, reducing remarkably the complexity of the modeling process. Whereas, it is unconvincing as to the reason why C. Liaw concluded that the three-phase rectifier and voltage-source can be approximated by a three-phase resistive load, as in Fig.4-2 (a). Firstly, E_{bat} is a constant. Consequently, R_L must be adjusted according to the real-time current to guarantee accuracy. Secondly, omission of DC voltage source not only hides the attribute that the stator current could remain stable for high values of speed but also degrades the hysteresis effect. The steady-state model used in this chapter, both stator impedance and battery voltage are taken into account by equalizing the three-phase rectifier and voltage-source to a battery model, as in Fig.4-2 (b).

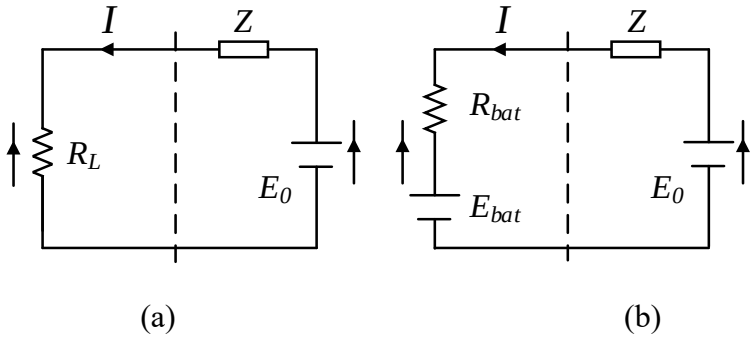

Fig. 4-2. (a) Electrical circuit model approximating the three-phase rectifier and voltage-source to a three-phase resistive. (b) Electrical circuit model approximating the three-phase rectifier and voltage-source to a battery model.

When the load is a battery and ignoring the mutual inductance, the currents and voltages in an IPMSM can be depicted by a phasor diagram in Fig.4-3. Below is the relation between phase terminal voltage V of IPMSM and load voltage when using Y-connected windings:

$$\sqrt{3}V = IR_{bat} + E_{bat} \tag{4.4}$$

The back EMF E_0 of IPMSM can be expressed as:

$$\begin{aligned} E_0 &= (V + IR_s)\cos\alpha + I_d X_d \\ &= [\frac{E_{bat}}{\sqrt{3}} + I(\frac{R_{bat}}{\sqrt{3}} + R_s)]\cos\alpha + I\sin\alpha\, p\omega L_d \end{aligned} \tag{4.5}$$

To determine the lead angle α, the imaginary vectors $\mathbf{V}+\mathbf{I}R_s$ and $j\mathbf{I}X_q$ can be used to obtain the following expressions:

$$\tan\alpha=\frac{IX_q}{IR_s+V}=\frac{Ip\omega L_q}{IR_s+\frac{E_{bat}+IR_{bat}}{\sqrt{3}}}=\frac{p\omega L_q}{R_s+\frac{R_{bat}}{\sqrt{3}}+\frac{E_{bat}}{\sqrt{3}I}} \tag{4.6}$$

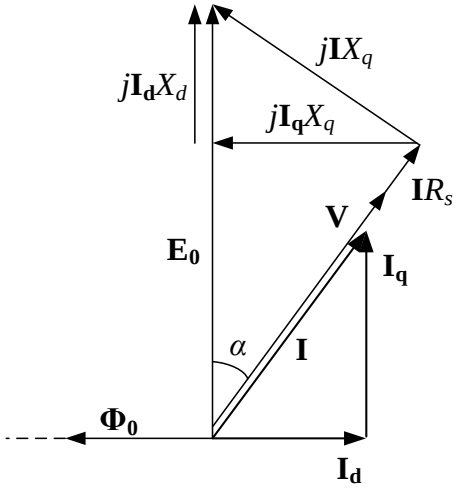

Fig. 4-3. Phasor diagram for an IPMSM operating as a generator.

And α can be described as:

$$\alpha=arc\tan\left(\frac{p\omega L_q}{R_s+\frac{R_{bat}}{\sqrt{3}}+\frac{E_{bat}}{\sqrt{3}I}}\right) \tag{4.7}$$

where p represents the number of pole pairs; ω is angular speed.

Obviously, there exist substantial differences between Liaw's model and (4.5). Now, an extra term $\frac{E_{bat}}{\sqrt{3}}\cos\alpha$ significantly boosts the complication when calculating UCG current I but it cannot be omitted. In order to get I, it is feasible to apply Taylor's theorem to sinα and cosα, and they are shown in (4.8) and (4.9), respectively.

$$\cos\alpha = \cos(arctan(\frac{p\omega L_q}{R_s + \frac{R_{bat}}{\sqrt{3}} + \frac{E_{bat}}{\sqrt{3}}})) - \sin(arctg(\frac{p\omega L_q}{R_s + \frac{R_{bat}}{\sqrt{3}} + \frac{E_{bat}}{\sqrt{3}}})) \cdot \frac{1}{1 + (\frac{p\omega L_q}{R_s + \frac{R_{bat}}{\sqrt{3}} + \frac{E_{bat}}{\sqrt{3}}})^2} \cdot \frac{p\omega L_q E_{bat}}{\sqrt{3}(R_s + \frac{R_{bat}}{\sqrt{3}} + \frac{E_{bat}}{\sqrt{3}})^2} \cdot (I - 1) \quad \textbf{(4.8)}$$

$$\sin\alpha = \sin(arctan(\frac{p\omega L_q}{R_s + \frac{R_{bat}}{\sqrt{3}} + \frac{E_{bat}}{\sqrt{3}}})) + \cos(arctg(\frac{p\omega L_q}{R_s + \frac{R_{bat}}{\sqrt{3}} + \frac{E_{bat}}{\sqrt{3}}})) \cdot \frac{1}{1 + (\frac{p\omega L_q}{R_s + \frac{R_{bat}}{\sqrt{3}} + \frac{E_{bat}}{\sqrt{3}}})^2} \cdot \frac{p\omega L_q E_{bat}}{\sqrt{3}(R_s + \frac{R_{bat}}{\sqrt{3}} + \frac{E_{bat}}{\sqrt{3}})^2} \cdot (I - 1) \quad \textbf{(4.9)}$$

Then we can solve (4.5) for I as follows:

$$I = \frac{-b_2 + \sqrt{b^2{}_2 - 4b_1 b_3}}{2b_1}$$

$$\begin{cases} b_1 = \dfrac{ACp\pi L_d n}{30} - BC(R_s + \dfrac{R_{bat}}{\sqrt{3}}) \\ b_2 = \dfrac{(B - AC)p\pi L_d n}{30} + (A + BC)(R_s + \dfrac{R_{bat}}{\sqrt{3}}) - \dfrac{BCE_{bat}}{\sqrt{3}} \\ b_3 = \dfrac{(A + BC)E_{bat}}{\sqrt{3}} - C'_e \Psi_f pn \\ A = \cos(arctg(\dfrac{p\pi L_q n}{30(R_s + \frac{R_{bat}}{\sqrt{3}} + \frac{E_{bat}}{\sqrt{3}})})) \\ B = \sin(arctg(\dfrac{p\pi L_q n}{30(R_s + \frac{R_{bat}}{\sqrt{3}} + \frac{E_{bat}}{\sqrt{3}})})) \\ C = \dfrac{p\pi L_q E_{bat} n}{30\sqrt{3}(R_s + \frac{R_{bat}}{\sqrt{3}} + \frac{E_{bat}}{\sqrt{3}})^2 (1 + (\frac{p\pi L_q n}{30(R_s + \frac{R_{bat}}{\sqrt{3}} + \frac{E_{bat}}{\sqrt{3}})})^2)} \end{cases} \quad \textbf{(4.10)}$$

where C'_e is the EMF constant relevant to motor, Ψ_f represents magnetic flux across per phase.

Because the peak value of charge currents and voltages at different speed can be calculated using the above model, the dynamic characteristics (such as maximum current--speed loci) can also be easily derived.

4.3 Analysis of UCG

For the sake of better understanding of the UCG process, the transient analysis is carried out firstly according to the dynamic IPM model proposed in section 4.2 and the working principles of IPMSM. Then, the differences between the traditional steady-state model and the new model are illustrated. After reaching the conclusion that the proposed steady-state model is more accurate for UCG analysis, the parameter dependencies of UCG performance characteristics are detailed finally.

4.3.1 Transient Process of UCG

UCG operation can be divided into three stages: firstly, transistors are shut down; secondly, diodes conduct; finally, UCG mode launches officially and enters a continuous generating stage. Analyzing switching process of IPM needs to investigate the transformation pattern in each course. For the sake of concise explanation, space vector pulse width modulation (SVPWM) method in the first sector [27] is taken as an example (as in Fig.4-4).

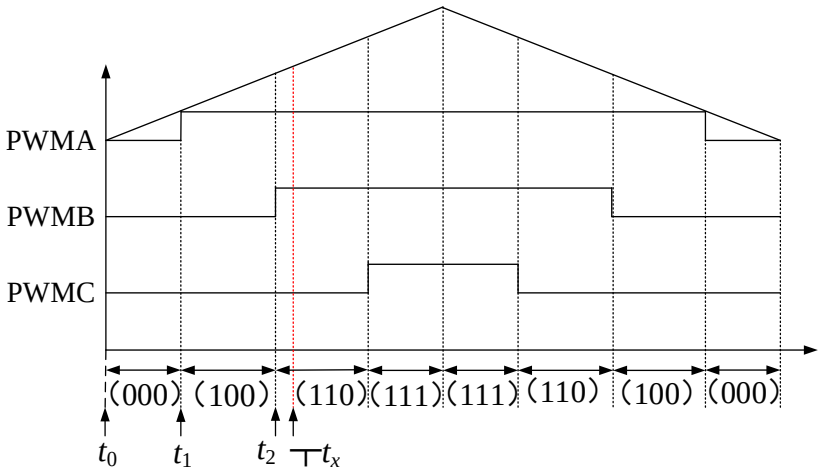

Fig. 4-4. SVPWM in the first sector.

The first stage is presented in detail in terms of different moments when a malfunction appears.

When the inverter functions normally, T_1， T_6， T_2 are on-state before t_0 after which zero space vector (000) works and D_4， T_6 and T_2 are freewheeling (as in Fig.4-5). A sudden shutdown over the period causes that the current has a tendency to drop and further the voltages on b-, c-phase windings are pulled up:

$$\begin{aligned} V_{bo} &= L_b \frac{\mathrm{d}I_b}{\mathrm{d}t} \approx L_b \frac{|I_b|}{\Delta t} \\ V_{co} &= L_c \frac{\mathrm{d}I_c}{\mathrm{d}t} \approx L_c \frac{|I_c|}{\Delta t} \end{aligned} \tag{4.11}$$

where V_{bo} and V_{co} are phase voltage; L_b and L_c are phase inductance; $\triangle t$ is the turn-off time which is so short that V_{bo} and V_{co} are prone to exceed dc-link voltage.

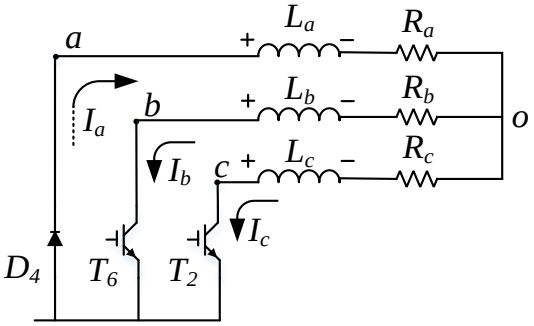

Fig. 4-5. Current loop composed of D4，T6，T2 and motor windings.

Between t_1 and t_2, T_1, T_6, T_2 are conducted, as in Fig.4-6. Aside from b-, c-phase windings, a-phase winding gets the same trend to generate high voltage if transistors are switched off. What is more, faults might occur practically between t_2 and (t_2+$\triangle t_x$) when a current loop composed of T_1， T_6 and D_3 works for freewheeling (as in Fig.4-7). Interestingly, the changing pattern of phase voltages is identical to that from t_0 to t_1.

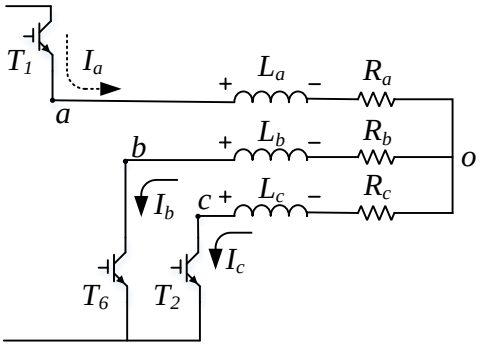

Fig. 4-6. Current loop composed of T_1, T_6, T_2 and motor windings.

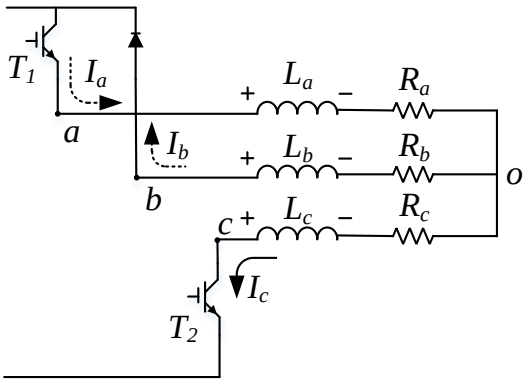

Fig. 4-7. Current loop composed of T_1, T_2, D_3 and motor windings.

In the second stage, freewheeling diodes always provide a passage for already existed currents in windings, but it differs from the normal freewheeling conditions in which currents can run through transistors and the energy is still in the motor [28]. Over the short-time period, the energy stored in the motor inductance will be released to the battery directly, resulting in high charge current probably. If UCG occurs at $t_0 \sim t_1$, the diode D_4 remains on and the voltages of b-, c-phase voltages are higher than that of phase a, so:

$$\begin{cases} V_{in} = \max(V_{ba}, V_{ca}) \\ V_{ba} = V_{bo} - V_{ao} \\ V_{ca} = V_{co} - V_{ao} \\ V_{out} = V_{in} - 2V_{on} \end{cases} \tag{4.12}$$

When $V_{ba}>V_{ca}$, D_3 turns on, and by contrast, D_5 does. When shutdown mode occurs between t_1 and t_2, a-phase voltage is the lowest and if $V_{ba}>V_{ca}$, D_3 and D_4 turns on at the same time, and in contrast, D_4 and D_5 does. Over the period $t_2 \sim (t_2+\triangle t_x)$, D_3 keeps on. A-phase voltage is lowest while c-phase voltage is highest, so that D_4 and D_5 are on:

$$\begin{cases} V_{in} = V_{ca} \\ V_{out} = V_{in} - 2V_{on} \end{cases} \tag{4.13}$$

The above account represents the process when the diodes conduct (energy release), after which consecutive UCG operation gets under way until charge current vanishes.

In the third stage, the magnetic field of air gap is restored soon after flux-weakening current disappears. Compared to the former two stages, this one is characterized by longer working time and large harmonic contents besides high current. Hence, battery and inverter are more inclined to get damaged over the period, as well. The following sections will mainly focus on the third stage, that is, the steady-state UCG process.

4.3.2 Comparison Between Traditional and Novel Steady-State Model

Compared to the proposed steady-state model used for performance analysis, the traditional one regarded the voltage source as a pure load resistance without the constant term E_{bat}. As is deduced in [25], the DC-link current can be easily calculated. But according to study results, that approximation method may miss important features of UCG, especially at high-speed points. Taking a prototype EV drive system with machine, inverter and battery parameters in Table 4-1 as an example, the curves of dc-link voltage and current versus different speed using different models are shown in Fig.4-8 and Fig.4-9, respectively.

TABLE 4-1
PROTOTYPE EV DRIVE SYSTEM PARAMETERS

Parameters	Value	Parameters	Value
motor phase resistance (Ω)	0.055	corner speed (rpm)	1700
d-axis inductance (mH)	0.1	battery ideal voltage (V)	60
q-axis inductance (mH)	0.8	battery internal resistance (Ω)	0.085
number of pole pairs	3	battery rated capacity (Ah)	20
PM magnetic flux (Wb)	0.0876	inverter maximum current (A)	70
EMF constant	0.078	diode turn-on voltage (V)	0.65

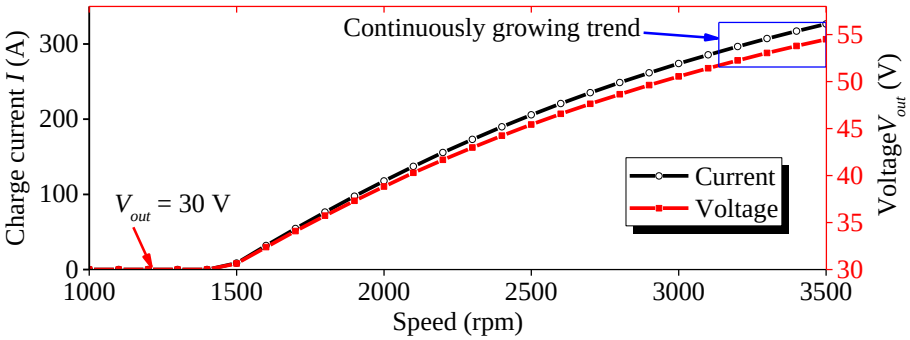

Fig. 4-8. DC-link voltage and current versus speed using traditional model.

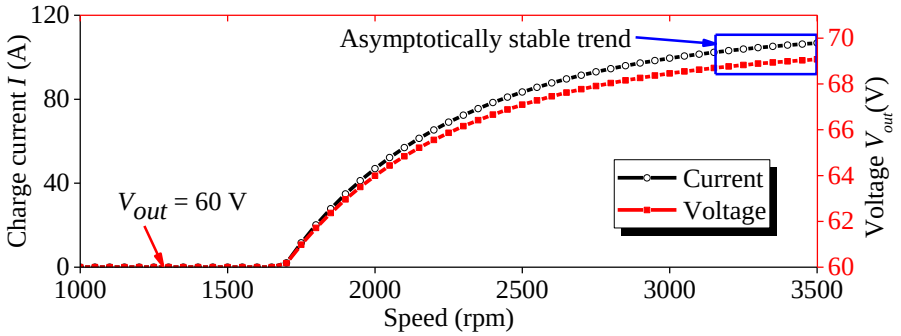

Fig. 4-9. DC-link voltage and current versus speed using proposed model.

It can be seen that there are substantial differences in both values and change trend. As for the traditional method, the currents and voltages keep going up continuously as the speed rises, which contradicts totally the conclusion drawn by Thomas. By contrast, the voltage for proposed model remains 60 V (E_{bat}) at low speed and the current curve is inclined to level off at high speed. Although the conventional model can reflect some characteristics, especially the output power, the new one is more precise for revealing the current and voltage properties.

4.3.3 Parameter Dependencies of UCG Performance

Equation (4.10) indicates the value of I heavily depends on motor inductance, phase resistance, magnetic flux and battery internal resistance. The detailed analysis of parameter dependencies of UCG will be conducted on the aforementioned machine as well.

In Fig.4-9, note that the charge current reaches 106.7 A (5.3 times the battery rated capacity, which is denoted as 5.3C) which overpasses greatly the inverter maximum working current when UCG starts at a speed of 3500 rpm. Undoubtedly, it's risky for the drive system.

Firstly, as is illustrated in Fig.4-10， when the *q*-axis inductance remains unchanged while the *d*-axis inductance increases (reducing saliency ratio), the dc-link current drops rapidly. Similarly, the current shows a downward trend while enlarging saliency ratio by keeping the *d*-axis inductance constant but expanding the *q*-axis inductance. What deserves to be mentioned is that *q*-axis inductance has less effect on the current changing rate than *d*-axis inductance. When *d*-axis inductance triples from 0.1 to 0.3 mH, the current decreases by over 39% from 106.7 to 64.9 A. Comparatively speaking, the current decreases by only 32% from a maximum of 46.8 to 31.8 A when *q*-axis inductance becomes threefold from 0.8 to 2.4 mH. Interestingly, even though the saliency ratio is fixed, the currents do not follow the same curve when *d*-, *q*-axis inductance shifts in the same proportion, which is inconsistent with Thomas's description. Overall, the inductance of machine rather than saliency ratio is the most direct factor affecting crucially the currents. Moreover, when *d*-, *q*-axis inductance increases to a certain extent, the current can be obviously suppressed or even rejected. For example, the largest DC-link current is merely 3.4 A at 3500 rpm with a combination of 40 mH *q*-axis inductance and 15 mH *d*-axis inductance.

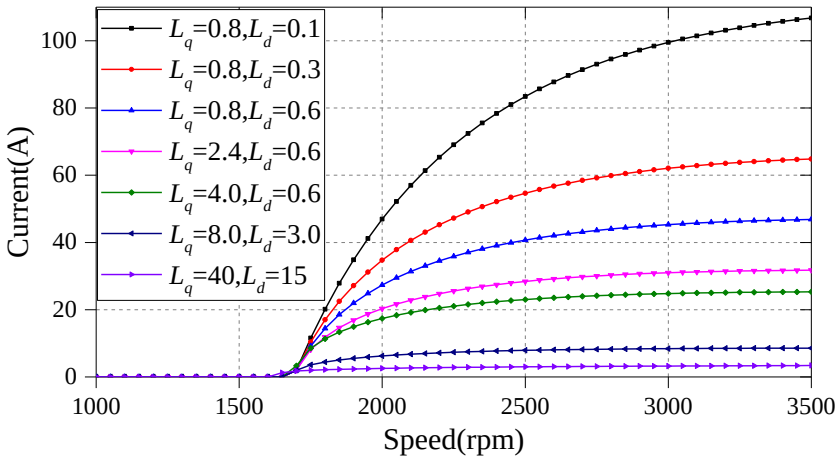

Fig. 4-10. DC-link current versus speed when *d*-, *q*-axis inductance is variable.

Secondly, for an extraordinarily compact and high-power- density IPMSM, the rotor structure limits the size of the permanent magnets, leading to that the value of Ψ_f changes within a small range of fluctuations in the course of design. When Ψ_f varies, the properties of DC-link current versus speed under different air-gap magnetic flux are demonstrated in Fig.4-11. As flux linkage goes up, the currents show an upward trend during UCG operation. The reason why this is the case is that the back EMF keeps in proportion to Ψ_f. When the magnetic flux increases

from 0.078 to 0.095 Wb, the maximum current obviously ascends from 57 to 70 A.Fig.10 also shows that the current curves shift laterally because the corner speed changes after changing the magnitude of Ψ_f.

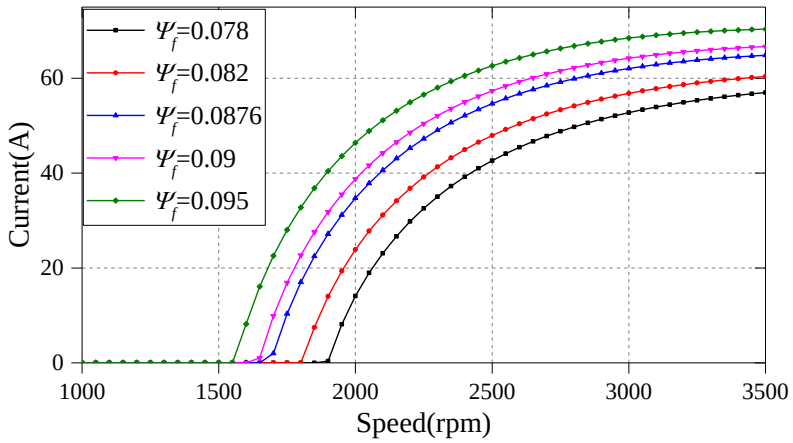

Fig. 4-11. DC-link current versus speed under different air-gap magnetic flux.

Thirdly, there are several ways which can influence the winding resistance—wire cross-sectional area, the number of conductor series turns, the number of parallel branches and external circuit series resistor that can be assumed as winding resistance. For purpose of simplicity, the fourth method is adopted to change the resistance and Fig.4-12 shows the characteristics of DC-link current versus speed in different cases. Clearly, the larger the motor resistances are, the lower the currents become. And interestingly, after R_s exceeds 0.1 Ω, the rate of decline for DC-link currents accelerates significantly.

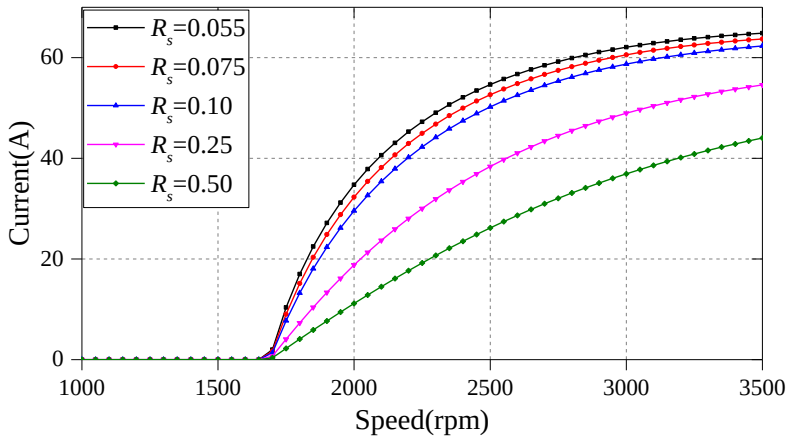

Fig. 4-12. DC-link current versus speed under different winding resistance.

Finally, battery stores energy, and the internal resistance which is inversely proportional to the

rated capacity works as load during UCG operation. To be honest, the battery internal resistance has the same impact on DC-link currents to machine phase resistors, as in Fig.4-13. It should be noticed that when the value of the parameter rises, the currents change pretty slightly because the value of battery resistances are too small. Between 0.015 and 0.15 Ω, the maximum currents at the speed of 3500 rpm are all above 60 A.

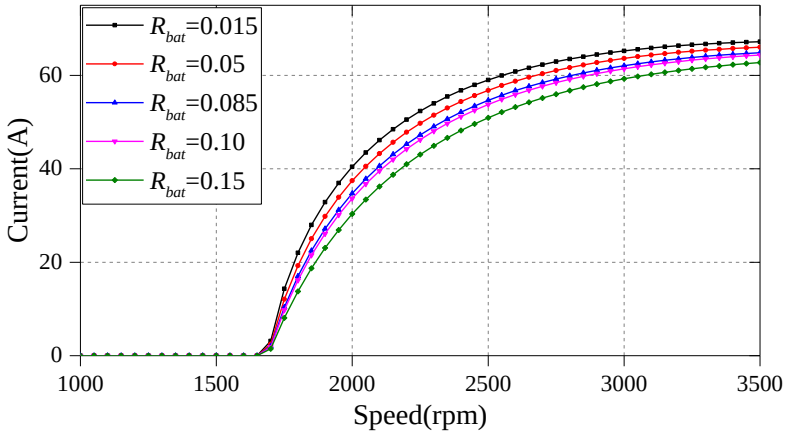

Fig. 4-13. DC-link current versus speed under various battery resistances.

Before leaving the current curves in Fig.4-9-Fig.4-13, it should be noted that the DC-link current appears to asymptote to a certain value for high speed. That is, the current for an IPMSM during UCG operation will not infinitely go over a constant value, which is identical to the previous conclusions.

4.4 IPMSM Design/Optimization for UCG Suppression

In Fig.4-9, it is noticed that the maximum UCG feedback current of the original IPMSM can reach over 106.7 A if the system protection mode is triggered in the high-speed range. In this research, the current magnitude is 5.3 C, which also overpasses greatly the inverter maximum working current. Undoubtedly, it poses great risk for the system safety. As is studied in section 4.3, proper motor parameters are contributive to the lower UCG feedback current, providing remarkable implications for designing/optimizing IPMSM. This section will introduce concrete procedures for attenuating the adverse effects of UCG.

4.4.1 Motor Parameter Optimization Strategy

The previous study of parameter dependencies indicates that the *d*-, *q*-axis inductance has more significant impacts on DC-link currents than Ψ_f and R_s do. For the cases where wide range of constant-power operation is needed, enlarging the *d*-axis inductance will also promote the flux-weakening capability of the machine and below is the reason. After injecting *d*-axis current i_d, the air-gap magnetic flux becomes:

$$\Psi_{f\_weaken} = \Psi_f + L_d i_d \tag{4.14}$$

Obviously, when the value of negative i_d is fixed, the air-gap magnetic flux will get reduced by much more once L_d increases. In other words, we can just impose smaller current to the IPMSM windings at the time when a fixed field is desired. Therefore, the strategy to modify the *d*-axis inductance without changing other parameters of machine is not only effective to reduce the maximum currents during UCG mode but also beneficial for speed-rising operation in the process of constant-power control.

As is shown in Fig.4-14, the IPMSM optimization flow aiming at an already existed scheme can be divided into four steps.

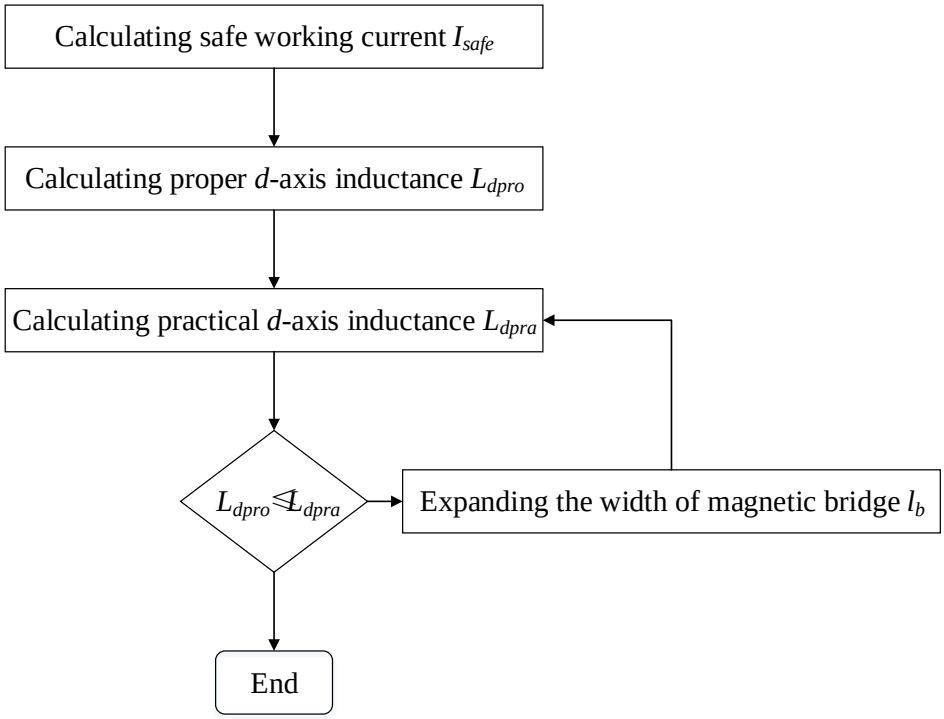

Fig. 4-14. Procedure for IPMSM redesign/optimization.

1) By the means of (4.10), we can calculate a proper *d*-axis inductance L_{dpro} when those other

machine parameters are fixed. But before that, the desired maximum speed n_{max} as well as the safe working current I_{safe} should be in a known state. Luckily, n_{max} is always determined by research or project requirements. When it comes to I_{safe}, the inverter maximum working current $I_{\max}$ and the battery rated capacity Q_{rated} need to be balanced comprehensively. It indicates that the largest battery charge current had better be under 3C [29], so that I_{safe} can be expressed by:

$$I_{safe} = \min(3C, I_{\max}) \tag{4.15}$$

2) After getting n_{max} and I_{safe}, we can solve (4.10) for L_{dpro}. Honestly, the value of L_{dpro} is just the inferior limit.

3) The practical *d*-axis inductance L_{dpra} of machine can be calculated using Maxwell whose results are more reliable than those calculated by predicting equations [30], after which we can compare L_{dpro} and L_{dpra}. That the real machine parameter is over the proper lower limit is capable of ensuring no dangerous over currents in the drive system.

4) The approach to increase the *d*-axis inductance is achieved by expanding the width of magnetic bridge l_b, as in Fig.4-15 (b). Compared with the IPMSM with Type "—" permanent magnet rotor structure in Fig.4-15 (a) (parameters are consistent with Table 4-1), the use of magnetic bridges reduces the *d*-axis reluctance so increases the relevant inductance. That can be explained by the predicting way to calculate *d*-axis reactance X_d [31]:

$$X_d = X_1 + C\frac{B_{ad}}{i_d} \tag{4.16}$$

where X_1 represents the leakage resistance of each phase winding while C is armature reaction reactance coefficient. They are related to angular speed, winding turns, length of rotor, pole pairs, the number of phase and the width of air gap. However, magnetic bridges rarely influence them. B_{ad} is the flux density amplitude of *d*-axis armature reaction. When the permeance along direct axis becomes larger by means of magnetic bridges, B_{ad} will dramatically increases in spite of injecting the same i_d. Consequently, larger X_d can be obtained and the wider l_b is, the greater *d*-axis inductance turns.

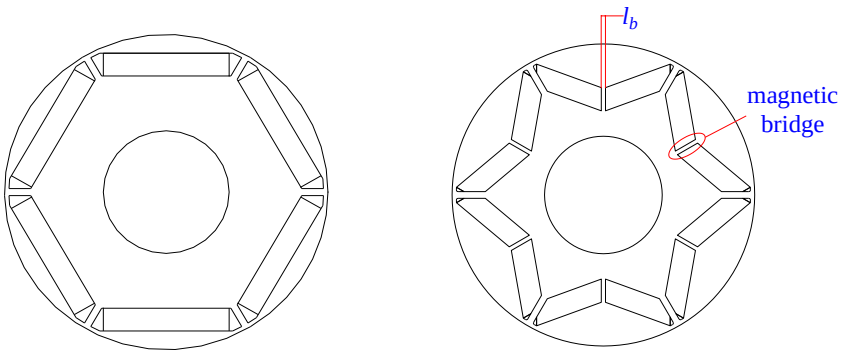

(a) (b)

Fig. 4-15. (a) Type "—" permanent magnet rotor structure. (b) V-type permanent magnet rotor structure.

Apply the design approach to the system shown in Table 4-1 and we can calculate that:

$$\begin{aligned} I_{safe} &= 60\text{A}, \\ L_{dpro} &= 0.35\text{mH} \end{aligned} \tag{4.17}$$

When l_b=1.25mm, the inductance matrix calculated by finite element simulation is shown in Fig.4-16, which can be transformed to the inductance values in the rotating reference frame as:

$$\begin{aligned} L_{dpra} &= 0.38\ \text{mH} \\ \therefore L_{dpra} &> L_{dpro} \end{aligned} \tag{4.18}$$

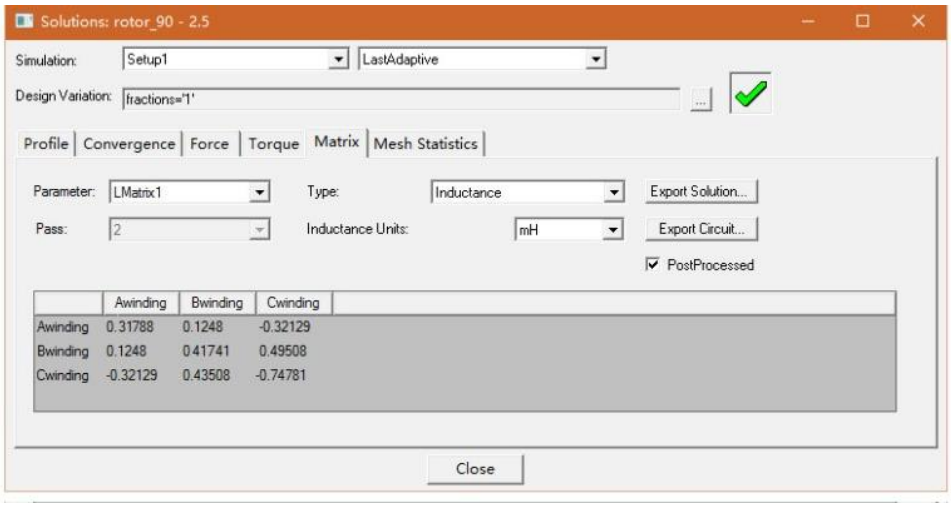

Fig. 4-16. Inductance matrix of the optimized IPMSM.

What has to be mentioned eventually is that although the motor design and optimization method can meet the requirements to restraint the peak UCG feedback current, it is time-consuming because of complex finite element analysis (FEA) process.

4.4.2 Experimental Verifications

The purposes of experiments include, firstly, gaining a better understanding of performance characteristics by monitoring the currents and voltages during UCG operation, and secondly, validating the improved steady-state model for UCG analysis and verifying the FEA based motor redesign approaches.

Experiments are conducted on a three-phase IPMSM drive system whose parameters are mostly consistent with Table 4-1 except the *d*-axis inductance (L_d=0.38mH). The experimental test bench is shown in Fig.4-17. The test machine is driven by another motor whose speed can reach a maximum of 3500 rpm. In the testing process, the motor drives the test IPMSM working as a generator to different speed from 3500 to 1000 rpm with a step decrease of 100 rpm. Although the experiments simulate the steady-state process of UCG at different speed points, a current (voltage)-speed curve concerning the dynamic characteristics can be depicted relying on the collected data. The speed is controlled by a DSP TMS32 28335 controller board. The DC-link currents and voltages are measured using HIOKI 3275 Clamp-on Probes which are connected to WT3000 used for displaying waveforms.

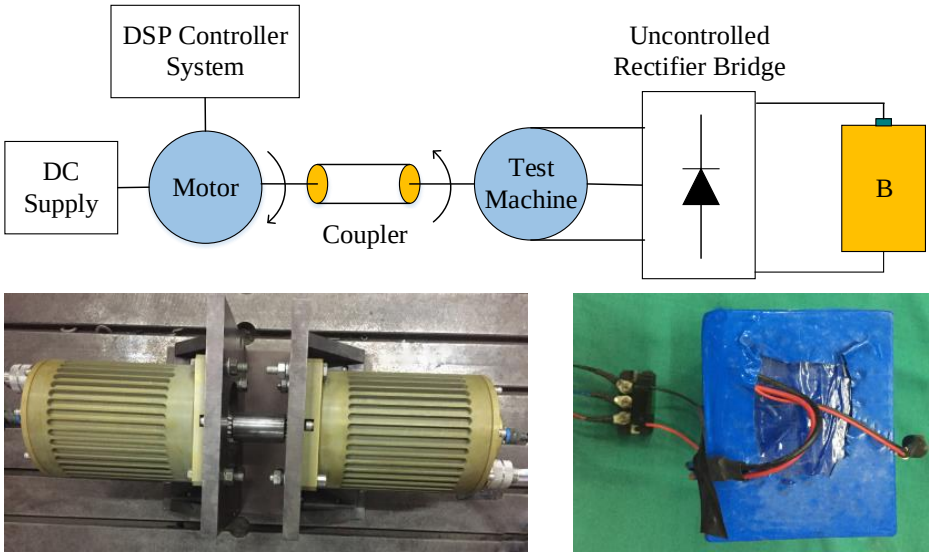

Fig. 4-17. Experimental test bench.

Curves of three-phase stator currents, DC-link current and voltage when the rotor speed is 3500 rpm are shown in Fig.4-18 from top to bottom. The motor three-phase currents are not continuous, which is determined by the diode conduction characteristics of UR in accord with (2) and (3). The output DC current and voltage are 63.5A and 72.4V. Thanks to that the rotor structure of the IPMSM is optimized, the current exceeds slightly the limit of 60A by only 5.5%. But the width of magnetic bridge should have been widened more. It is also noted that the frequency of ripple for both DC-link current and voltage is six times than that of the fundamental waves, accelerating positive-plate corrosion of battery life in the long run [32].

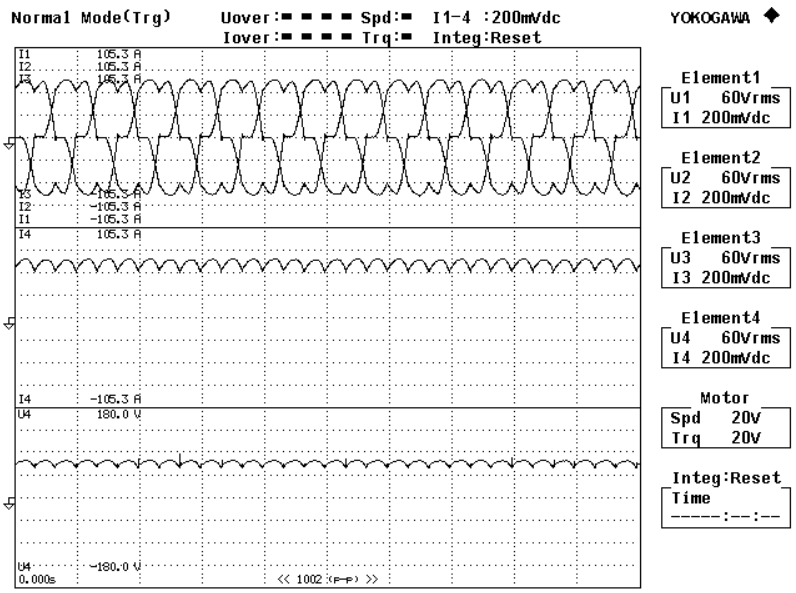

Fig. 4-18. Three-phase stator currents, DC-link current and voltage at the speed of 3500 rpm.

Fig.4-19 illustrates the current and voltage characteristics assuming that UCG occurs at the speed of 3300 rpm. It can be seen that the maximum DC-link current and voltage is 63.12 A and 73.85 V.

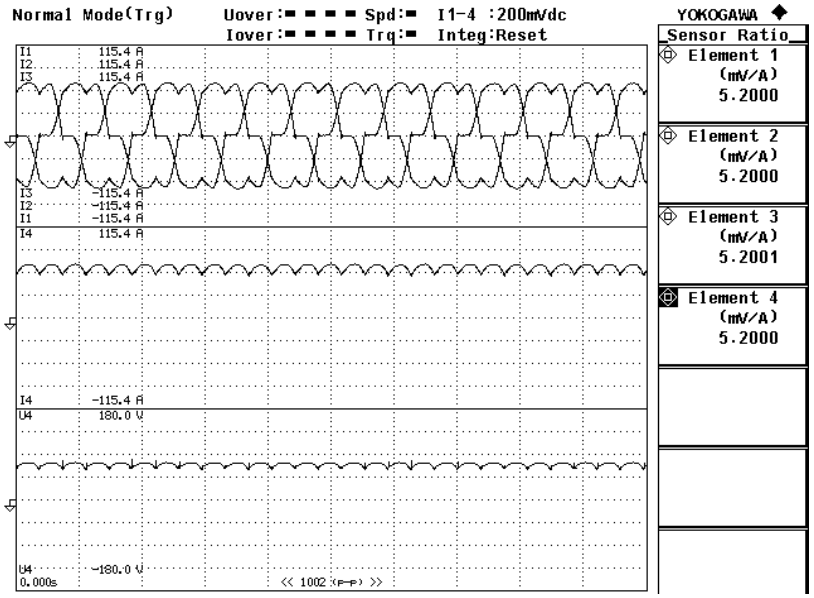

Fig. 4-19. Three-phase stator currents, DC-link current and voltage at the speed of 3300 rpm.

In Fig.4-20, the current and voltage performance characteristics UCG occurs at the speed of 3000 rpm are shown. The maximum DC-link current and voltage is 61.49 A and 71.89 V.

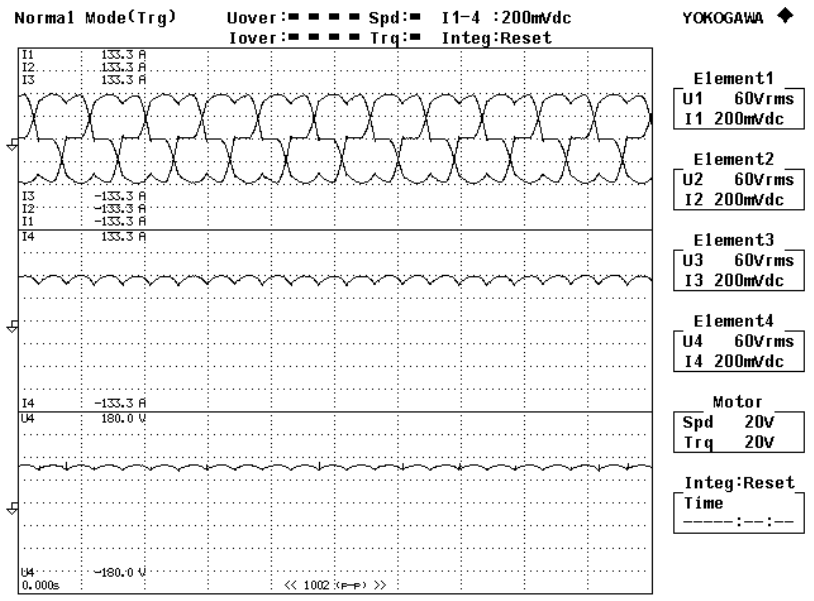

Fig. 4-20. Three-phase stator currents, DC-link current and voltage at the speed of 3000 rpm.

Fig.4-21 illustrates the current and voltage characteristics when the machine speed is 2600 rpm. The maximum DC-link current and voltage is 55.53A and 70.45 V.

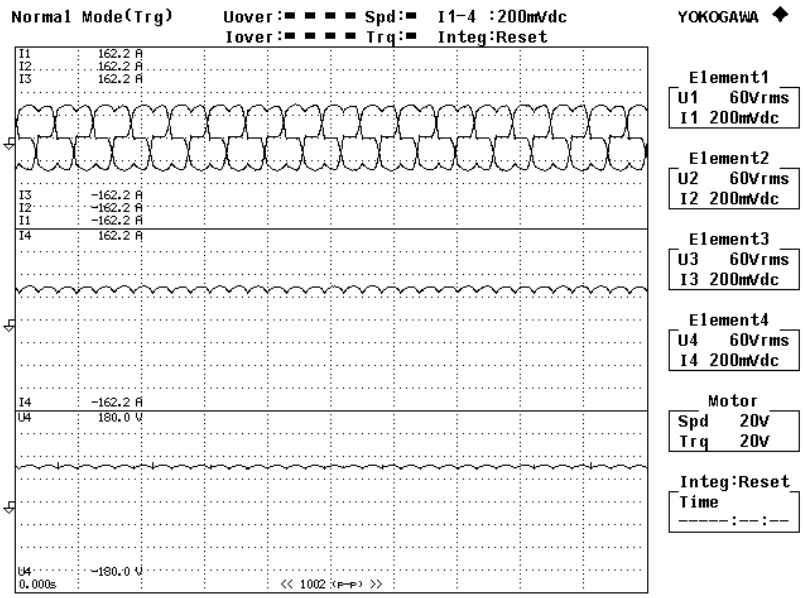

Fig. 4-21. Three-phase stator currents, DC-link current and voltage at the speed of 2600 rpm.

In Fig.4-22, the current and voltage characteristics when the machine speed is 2200 rpm are illustrated. The maximum DC-link current and voltage is 48.79 A and 68.12 V.

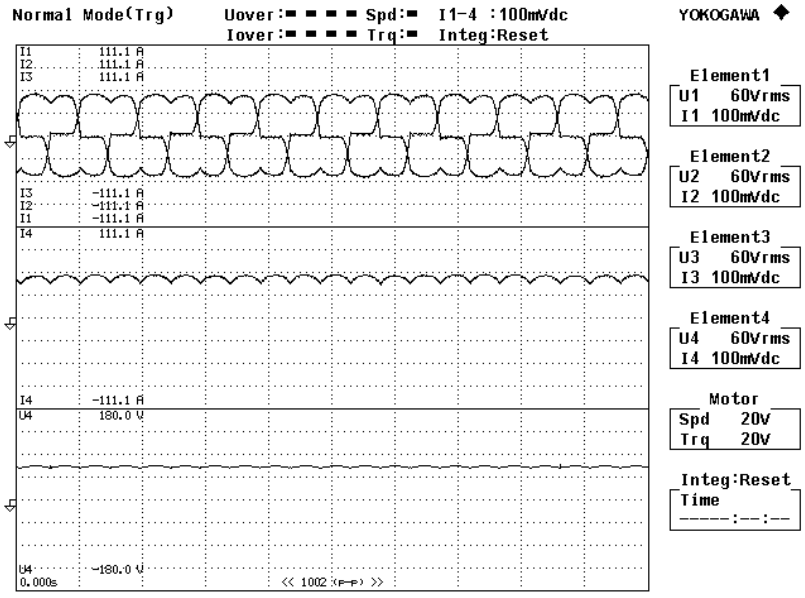

Fig. 4-22. Three-phase stator currents, DC-link current and voltage at the speed of 2200 rpm.

In Fig.4-23, the current and voltage characteristics when the machine speed is 1900 rpm are illustrated. It can be seen that the maximum DC-link current and voltage is 35 A and 65.5 V.

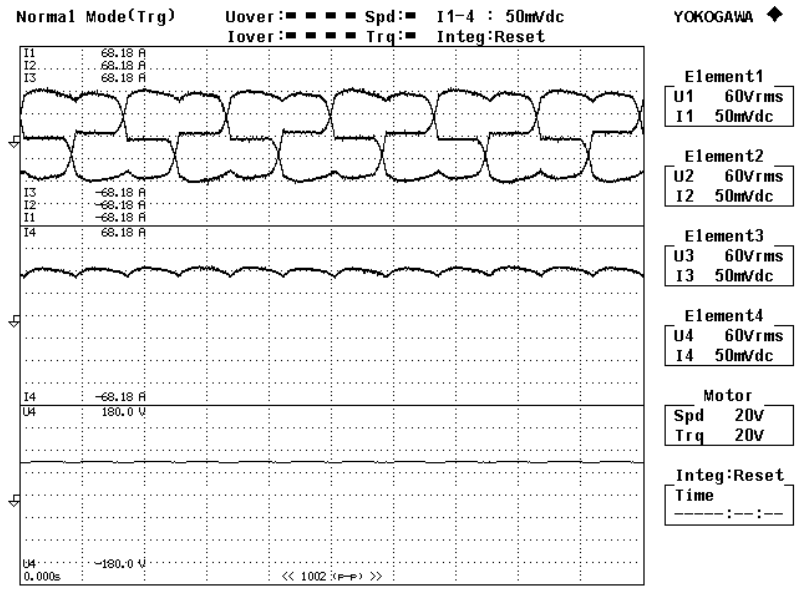

Fig. 4-23. Three-phase stator currents, DC-link current and voltage at the speed of 1900 rpm.

Fig.4-24 demonstrates the steady-state current and voltage characteristics when the machine speed is 1600 rpm. There still exists DC current with a value of 1.75A at the speed of 1600 rpm, indicating that the corner speed is not the cut-off point during deceleration, and verifying the prediction in [24].

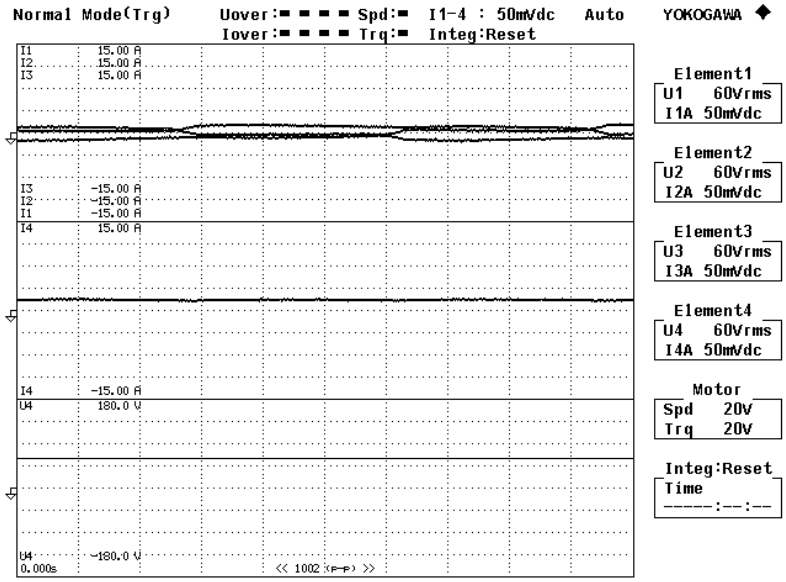

Fig. 4-24. Three-phase stator currents, DC-link current and voltage at the speed of 1600 rpm.

In fact, because the experiment simulates the steady-state process of UCG at different speeds, the recorded data can be converted into a current-speed curve, as shown in Fig.4-25. The predicted current is calculated based on the real motor and battery parameters using (3.10). Compared with the test curve, the steady-state UCG model proposed in this chapter achieve higher predicted values at low speed, especially at 1700 rpm. In the mid-speed section (1800-2600 rpm), the forecast error is the smallest. However, although the predicted result is a little lower than the measured value at high speed, the experimental results show that the final current will gradually level off. So the predicted model which is adopted to figure out the safe working current I_{safe} during IPMSM redesign can roughly ensure safety in the process of UCG.

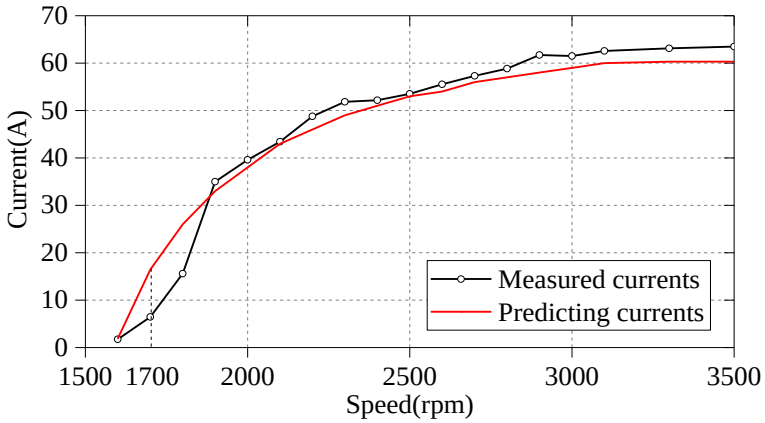

Fig. 4-25. DC-link current versus speed.

4.5 Summary

This chapter studies several aspects of UCG operation for IPMSM in EVs. This topic is related to the EV safety improvement in the post-fault situations. Firstly, a dynamic IPM model is established to observe the transient process, explaining the instantaneous transformation patterns after faults appear. Secondly, a steady-state UCG model is improved by approximating the DC voltage source to a resistor in series with an ideal voltage source rather than just a load resistance, investigating the relationship between performance characteristics and system parameters. Finally, a detailed IPMSM optimization method by increasing *d*-axis inductance is

proposed based on FEA to suppress UCG. The experimental results prove that the new model is more accurate and the IPMSM optimization method is effective.

4.6 References

[1] W. L. Soong and T. J. E. Miller, “Field-weakening performance of brushless synchronous AC motor drives,” *Proc. Inst. Elect. Eng.-Elect. Power Applicat.*, vol. 141, no. 6, pp. 331-340, Nov.1994.

[2] F. Li, K. T. Chau and C. Liu, “Pole-Changing Flux-Weakening DC-Excited Dual-Memory Machines for Electric Vehicles,” in *IEEE Trans. Energy Conv.*, vol. 31, no. 1, pp. 27-36, March 2016.

[3] L. Dang, N. Bernard, N. Bracikowski and G. Berthiau, “Design Optimization with Flux Weakening of High-Speed PMSM for Electrical Vehicle Considering the Driving Cycle, ” *IEEE Trans. Ind. Electron.*, vol. 64, no. 12, pp. 9834-9843, Dec. 2017.

[4] X. Du, J. Hu and X. Li, “Simulation of flux-weakening control of PMSM for electrical vehicle,” *17th Int. Conf. Electr. Mach. Syst.*, Hangzhou, 2014, pp. 529-532.

[5] X. Liu, H. Chen, J. Zhao and A. Belahcen, “Research on the Performances and Parameters of Interior PMSM Used for Electric Vehicles,” *IEEE Trans. Ind. Electron.*, vol. 63, no. 6, pp. 3533-3545, June 2016.

[6] Y. Zhang, W. Cao, S. McLoone and J. Morrow, “Design and Flux-Weakening Control of an Interior Permanent Magnet Synchronous Motor for Electric Vehicles,” *IEEE Trans. Appl. Supercond.*, vol. 26, no. 7, pp. 1-6, Oct. 2016.

[7] J. Mun, G. Park, S. Seo, D. kim, Y. Kim and S. Jung, "Design Characteristics of IPMSM With Wide Constant Power Speed Range for EV Traction," *IEEE Transactions on Magnetics*, vol. 53, no. 6, pp. 1-4, June 2017, Art no. 8105104.

[8] H. T. Anh and M. Hsieh, "Comparative study of PM-assisted SynRM and IPMSM on constant power speed range for EV applications," *2017 IEEE International Magnetics Conference (INTERMAG)*, Dublin, 2017, pp. 1-1.

[9] J. Du, X. Wang and H. Lv, "Optimization of Magnet Shape Based on Efficiency Map of IPMSM for EVs," *IEEE Transactions on Applied Superconductivity*, vol. 26, no. 7, pp. 1-7, Oct. 2016, Art no. 0609807.

[10] I. Won, D. Kim, Y. Jang, K. Choo, S. Hong and C. Won, "Improved FOC of IPMSM using model predictive current control decreasing switching loss for EV," *2016 19th International Conference on*

Electrical Machines and Systems (ICEMS), Chiba, 2016, pp. 1-6.

[11] J. Hwang, I. Won, D. Kim, Y. Kim and C. Won, "The current dynamic improving method of IPMSM using predictive current control for EV," *2015 18th International Conference on Electrical Machines and Systems (ICEMS)*, Pattaya, 2015, pp. 1786-1791.

[12] H. Jung, G. Park, D. Kim and S. Jung, "Optimal design and validation of IPMSM for maximum efficiency distribution compatible to energy consumption areas of HD-EV," *2016 IEEE Conference on Electromagnetic Field Computation (CEFC)*, Miami, FL, 2016, pp. 1-1.

[13] X. Fan, B. Zhang, R. Qu, J. Li, D. Li and Y. Huo, "Comparative thermal analysis of IPMSMs with integral-slot distributed-winding (ISDW) and fractional-slot concentrated-winding (FSCW) for electric vehicle application," *2017 IEEE International Electric Machines and Drives Conference (IEMDC)*, Miami, FL, 2017, pp. 1-8.

[14] J. Mun, G. Park, S. Seo, D. Kim, Y. Kim and S. Jung, "Design characteristics of IPMSM with wide constant power speed range for EV traction," *2016 IEEE Conference on Electromagnetic Field Computation (CEFC)*, Miami, FL, 2016, pp. 1-1.

[15] I. Urquhart, D. Tanaka, R. Owen, Z. Q. Zhu, J. B. Wang and D. A. Stone, "Mechanically actuated variable flux IPMSM for EV and HEV applications," *2013 World Electric Vehicle Symposium and Exhibition (EVS27)*, Barcelona, 2013, pp. 1-12.

[16] M. Lim, S. Chai and J. Hong, "Design of Saliency-Based Sensorless-Controlled IPMSM With Concentrated Winding for EV Traction," in *IEEE Transactions on Magnetics*, vol. 52, no. 3, pp. 1-4, March 2016, Art no. 8200504.

[17] T. Kato, T. Matsuura, K. Sasaki and T. Tanimoto, "Principle of variable leakage flux IPMSM using arc-shaped magnet considering variable motor parameter characteristics depending on load current," *2017 IEEE Energy Conversion Congress and Exposition (ECCE)*, Cincinnati, OH, 2017, pp. 5803-5810.

[18] Y. Hwang and J. Lee, "HEV Motor Comparison of IPMSM With Nd Sintered Magnet and Heavy Rare-Earth Free Injection Magnet in the Same Size," in *IEEE Transactions on Applied Superconductivity*, vol. 28, no. 3, pp. 1-5, April 2018, Art no. 5206405.

[19] S. Atiq, T. A. Lipo and B. I. Kwon, “Wide Speed Range Operation of Non-Salient PM Machines,” *IEEE Trans. Energy Conv.*, vol. 31, no. 3, pp. 1179-1191, Sept. 2016.

[20] K. Chen, Y. Sun and B. Liu, “Interior Permanent Magnet Synchronous Motor Linear Field-Weakening Control,” *IEEE Trans. Energy Conv.*, vol. 31, no. 1, pp. 159-164, March 2016.

[21] M. S. Huang and C. M. Liaw, “Improved field-weakening control for IFO induction motor," *IEEE Trans.*

Aeros. Electron. Syst., vol. 39, no. 2, pp. 647-659, April 2003.

[22] J. Liu, X. Ding and C. Mi, "Effectively dealing with uncontrolled generation of traction motors in hybrid electric vehicles," *Int. Conf. Electr. Mach. Syst.*, Beijing, 2011, pp. 1-4.

[23] J. Liu, X. Ding and C. Mi, "Effectively dealing with uncontrolled generation of traction motors in hybrid electric vehicles," *Int. Conf. Electr. Mach. Syst.*, Beijing, 2011, pp. 1-4.

[24] T. M. Jahns and V. Caliskan, "Uncontrolled generator operation of interior PM synchronous machines following high-speed inverter shutdown," *IEEE Trans. Ind. Appl.*, vol. 35, no. 6, pp. 1347-1357, Nov/Dec 1999.

[25] Chong-Zhi Liaw, W. L. Soong, B. A. Welchko and N. Ertugrul, "Uncontrolled generation in interior permanent-magnet Machines," *IEEE Trans. Ind. Appl.*, vol. 41, no. 4, pp. 945-954, July-Aug. 2005.

[26] J. Appelbaum and R. Weiss, "An Electrical Model of the Lead-Acid Battery," in *Proc. IEEE INTELEC'82*, Washington, DC, USA, 1982, pp. 304-307.

[27] Y. M. Pok and J. X. Xu, "An analysis of fuzzy control systems using vector space," *Proc. IEEE Int. Conf. Fuzzy Syst.*, San Francisco, CA, 1993, pp. 363-368 vol.1.

[28] H. K. Kim, J. H. Park and J. Hur, "Comparison Analysis of Demagnetization and Torque Ripple in Accordance With Freewheeling Current in PM BLDC Motor," *IEEE Trans. Magnetics*, vol. 51, no. 11, pp. 1-4, Nov. 2015.

[29] T. S. Mundra and A. Kumar, "An Innovative Battery Charger for Safe Charging of NiMH/NiCd Batteries," *IEEE Trans. Consum. Electron.*, vol. 53, no. 3, pp. 1044-1052, Aug. 2007.

[30] E. Schmidt and M. Sušić, "Parameter evaluation of permanent magnet synchronous machines with tooth coil windings using the frozen permeabilities method with the finite element analyses," *Proc. IEEE CCECE'12*, Montreal, QC, 2012, pp. 1-5.

[31] W. Dai, J. Zhang, "Synchronous motor design," in *Motor Design*, 1st ed. Beijin, China: Tsinghua Univ. Press & Springer, 2010, cha. 3, sec. 2, pp.198-200.

[32] Chao Gong, Jinglin Liu, Zexiu Han and Haozheng Yu, "Analysis on uncontrolled generation in electrical vehicles and a battery protection method," *Proc. IEEE IFEEC'17-ECCE Asia*, Kaohsiung, 2017, pp. 1606-1610.

Chapter 5 **Reliable DC-bus Capacitor Discharge Strategy for PMSM based Battery EVs**

By contrast with the previous chapter that focuses on the UCG problem which only arises when an EV is in the post-fault conditions, this chapter considers a harsher scenario. Pitiful car accidents are inevitable and beyond control on the roads. Fortunately, the passengers are able to survive in virtue of the robust passive safety devices (safety belts and airbags, etc.). Otherwise, some potential risks still exist even though the car is stopped, constantly threatening the safety of passengers. For example, the energy stored in the electrical components (machine and capacitor) is likely to cause electric shock if they cannot be released in time. In order to dissipate the residual energy in the IPMSM drive systems when an emergency happens to EVs, this chapter develops a winding-based discharge strategy. The winding-based method needs to control the *d, q*-axis current in the motor and it requires accurate position information during the whole discharge process. Whereas, the position sensor installed in the motor is likely to fail due to the violent vibration and impact in the emergency. Considering the position sensor faults, this chapter presents a position estimator based on sliding mode theory to endow the discharge algorithm with fault tolerance capacity firstly. The proposed discharge strategy treats the machine as a generator to regulate the DC-bus voltage and takes advantage of the maximum discharge capacity of the drive system. By quickly discharging the DC-bus capacitor voltage, the safety of the system can be ensured.

5.1 Introduction

Considering the emergency situations, the breaker on the DC bus should be taken into account. With reference to Fig.4-1 (a), the EV IPMSM drive topology used for analysis in this chapter is shown in Fig. 5-1. Once the EV crashes, the circuit interrupter will be tripped immediately. As for the capacitor voltage V_C, it is required to decrease to 60 V within 5 s to avoid electric shock risk according to the United Nation Vehicle Regulation ECE R94 [1].

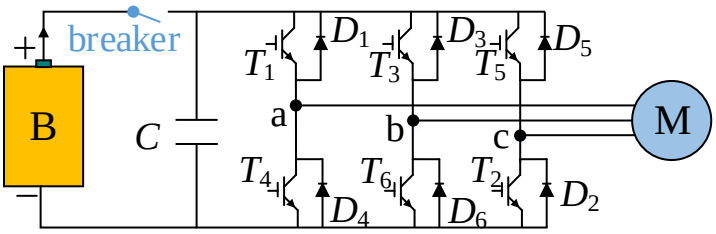

Fig. 5-1. Topology of EV PMSM drive system.

It is hard to quickly reduce the capacitor voltage to the safe level because the machine still rotates at high speed after an accident and the residual mechanical energy will be converted to electrical energy, recharging the capacitor continuously. Usually, an external circuit composed of a power resistor and a switch is employed to expend the residual energy in the PMSM drive system [2]. Although this method is effective and the bus voltage can be quickly reduced, the use of extra circuits increases the size, weight and cost of the EV drive systems. Besides, the reliability of the discharge system is low when extra devices are incorporated.

Because the machine windings made of copper and aluminum have resistance, they can be functioned as the bleeder load to consume the residual energy in the system [3]. In this case, the external emergency will not trigger a protection regime immediately, shutting off all of the transistors in the power converter. Instead, an active discharge operating mode that the machine is driven to operate normally launches before it. During the discharge process, the clutch in the vehicle has to disconnect the wheels from the traction motor first and then the motor just rotates with no load [4]. In order to quicken the discharge speed, this kind of DC-bus capacitor energy consumption method needs to properly control the current (both the *d*- and *q*-axis current) in the PMSM [5-6].

As a practical matter, the implementation of the winding-based discharge algorithm must use accurate machine rotor position which is usually provided by an external position sensor (eg., rotary transformer). However, it is highly possible for the rotating part of the sensor that is installed in the machine to malfunction due to the violent vibration and collision impact when emergency occurs, leading to the fact that a winding-based discharge strategy relying on the position sensor is not reliable in reality. Considering position sensor fault, an efficient position fault controller for position estimation is more reliable to bleed the bus voltage by the use of machine windings. Before the DC-bus voltage is discharged under 60 V, a PMSM usually

works in the relatively high-speed range and the voltage fluctuates while declining (disturbance factors). Hence, in order to obtain the accurate position, a robust position tracking algorithm based on back electromotive force (EMF) like sliding mode (SM) sensorless control strategy is needed [7-15]. Yet there are no studies about the more reliable winding-based discharge control algorithm which is based on that kind of fault tolerant control technique.

This chapter firstly introduces the traditional position observer based on SM principle. Then, an improved sliding mode observer of which chartering effect can be attenuated without using low pass filter is proposed. On this ground a winding-based capacitor discharge strategy with position sensor fault tolerance capacity is proposed to quickly and safely dissipate the bus capacitor voltage. By applying nonzero *d*- and *q*-axis currents to the machine, the capacitor voltage can be regulated to remain under 60 V during the whole bleeding process, and the discharge period can satisfy the requirement so as to keep the passengers from the danger of electric shock.

5.2 Design of Position Observer based on SM Theory

5.2.1 Traditional Position Observer based on SM Theory

a) Machine modelling

In order to design a SM observer, the IPMSM model that reveals the current dynamics in the two-phase stationary reference frame (α, β) rather than the three-phase stationary axis reference frame is needed. Hence, before establishing the required model, the procedures of coordinate transformation for stator current and voltage should be explained firstly.

The three-phase stator current performance of an IPMSM in the stationary axis reference frame is depicted in Fig.5-2 (a), where F_A, F_B and F_C are the magnetomotive forces in the direction of phase axis. F represents the synthetic magnetomotive force. i_A, i_B and i_C are the three-phase currents. φ is the angle between F_A and F. Then, assuming that the number of winding turns is N_a, it can be obtained that:

$$\begin{cases} F_A = N_a i_A \\ F_B = N_a i_B \\ F_C = N_a i_C \end{cases} \tag{5.1}$$

The current performance of the IPMSM in the stationary axis reference frame is depicted in Fig.5-2 (b). Assume that the number of winding turns is N_b, F_α and F_β are the α, β-axis magnetomotive forces, and it can be obtained that:

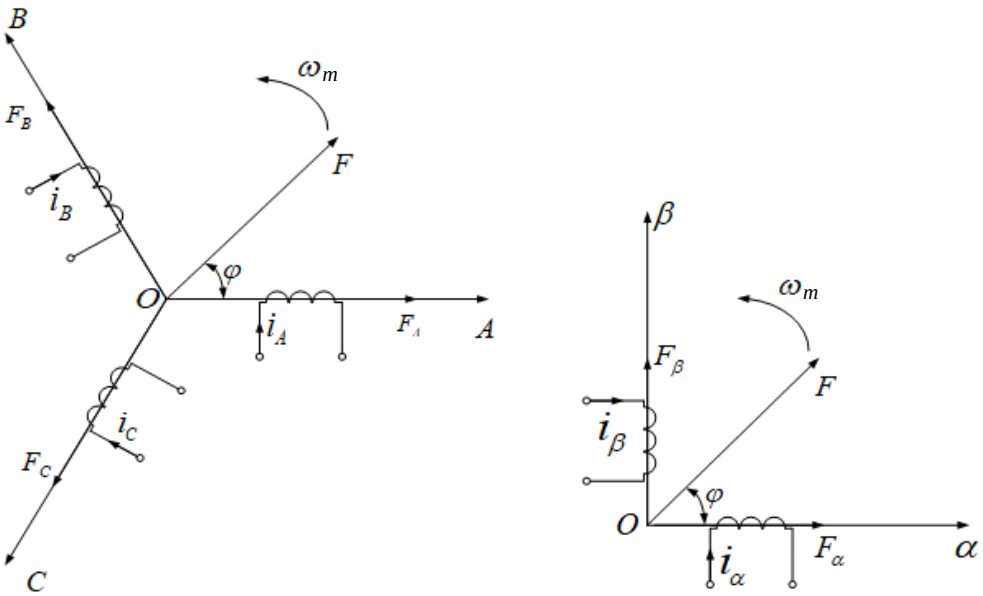

(a) (b)

Fig. 5-2. PMSM model. (a) Model in the three-phase stationary axis reference frame. (b) Model in two-phase stationary reference frame.

$$\begin{cases} F_\alpha = N_b i_\alpha \\ F_\beta = N_b i_\beta \end{cases} \tag{5.2}$$

where i_α, i_β are the α, β-axis currents. Because the magnetomotive forces do not shift after the transformation of coordinates, we can get that:

$$\begin{cases} N_b i_\alpha = N_a i_A \cos 0 + N_a i_B \cos\dfrac{2\pi}{3} + N_a i_C \cos\dfrac{4\pi}{3} \\ N_b i_\beta = N_a i_B \sin\dfrac{2\pi}{3} + N_a i_C \sin\dfrac{4\pi}{3} \end{cases} \tag{5.3}$$

And the relationship between the phase currents and the α, β-axis currents is as follows:

$$\begin{cases} i_\alpha = \dfrac{N_a}{N_b}(i_A \cos 0 + i_B \cos\dfrac{2\pi}{3} + i_C \cos\dfrac{4\pi}{3}) = \dfrac{N_a}{N_b}(i_A - \dfrac{1}{2} i_B - \dfrac{1}{2} i_C) \\ i_\beta = \dfrac{N_a}{N_b}(i_B \sin\dfrac{2\pi}{3} + i_C \sin\dfrac{4\pi}{3}) = \dfrac{N_a}{N_b}(\dfrac{\sqrt{3}}{2} i_B - \dfrac{\sqrt{3}}{2} i_C) \end{cases} \tag{5.4}$$

In order to obtain a square matrix which is simple to analyse, we manually add a zero magnetomotive force in the two-phase stationary reference frame, that is,

$$i_0 = \frac{N_a}{N_b}(k i_A + k i_B + k i_C) \tag{5.5}$$

Denote (5.4) and (5.5) in the form of matrix, we can obtain that:

$$\begin{bmatrix} i_\alpha \\ i_\beta \\ i_0 \end{bmatrix} = \frac{N_a}{N_b} \begin{bmatrix} 1 & -\dfrac{1}{2} & -\dfrac{1}{2} \\ 0 & \dfrac{\sqrt{3}}{2} & -\dfrac{\sqrt{3}}{2} \\ k & k & k \end{bmatrix} \begin{bmatrix} i_A \\ i_B \\ i_C \end{bmatrix} \tag{5.6}$$

The Clarke transformation matrix can be extracted from (5.6):

$$C_{clarke} = \frac{N_a}{N_b} \begin{bmatrix} 1 & -\dfrac{1}{2} & -\dfrac{1}{2} \\ 0 & \dfrac{\sqrt{3}}{2} & -\dfrac{\sqrt{3}}{2} \\ k & k & k \end{bmatrix} \tag{5.7}$$

In the constant power conditions, the product of Clarke transform matrix and its transposed matrix should equal **E**, that is:

$$C_{Clarke}\cdot C^{T}{}_{Clarke}=\frac{N_a}{N_b}\begin{bmatrix}1 & -\frac{1}{2} & -\frac{1}{2}\\ 0 & \frac{\sqrt{3}}{2} & -\frac{\sqrt{3}}{2}\\ k & k & k\end{bmatrix}\cdot\frac{N_a}{N_b}\begin{bmatrix}1 & 0 & k\\ -\frac{1}{2} & \frac{\sqrt{3}}{2} & k\\ -\frac{1}{2} & -\frac{\sqrt{3}}{2} & k\end{bmatrix}=\frac{N_a{}^2}{N_b{}^2}\begin{bmatrix}\frac{3}{2} & 0 & 0\\ 0 & \frac{3}{2} & 0\\ 0 & 0 & 3k^2\end{bmatrix}=\mathbf{E} \tag{5.8}$$

Therefore, it can be derived that:

$$\frac{N_a}{N_b}=\sqrt{\frac{2}{3}},\ k=\frac{1}{\sqrt{2}} \tag{5.9}$$

So far, the three-phase currents can be transformed into the variables in the α,β reference frame. Take the magnetic field generated by permanent magnet into account, and the physical machine model can be illustrated in Fig.5-3, where Ψ_f is the permanent magnet flux and θ is the rotor position.

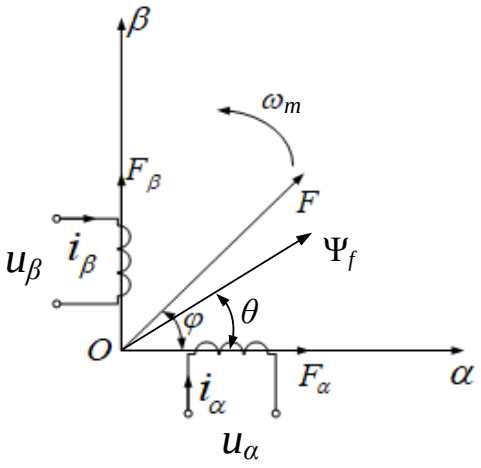

Fig. 5-3. Physical IPMSM model considering magnetic field generated by permanent magnet in two-phase stationary reference frame.

According to Fig.5-3, the voltage equations can be obtained as:

$$\begin{cases} u_\alpha = i_\alpha R_\alpha + \dfrac{\mathrm{d}(L_\alpha i_\alpha + \Psi_f \cos\theta)}{\mathrm{d}t} \\ u_\beta = i_\beta R_\beta + \dfrac{\mathrm{d}(L_\beta i_\beta - \Psi_f \cos\theta)}{\mathrm{d}t} \end{cases} \tag{5.10}$$

where L_α and L_β are the inductance and R_α and R_β are the resistance. For the sake of simplicity, assume that $L_s=L_\alpha=L_\beta$ and $R_s=R_\alpha=R_\beta$. Then, the current dynamics can be derived according to (5.10) as follows:

$$\begin{bmatrix} \dfrac{\mathrm{d}i_\alpha}{\mathrm{d}t} \\ \dfrac{\mathrm{d}i_\beta}{\mathrm{d}t} \end{bmatrix} = \begin{bmatrix} -\dfrac{R_s}{L_s} & 0 \\ 0 & -\dfrac{R_s}{L_s} \end{bmatrix} \begin{bmatrix} i_\alpha \\ i_\beta \end{bmatrix} + \begin{bmatrix} \dfrac{1}{L_s} & 0 \\ 0 & \dfrac{1}{L_s} \end{bmatrix} \begin{bmatrix} u_\alpha \\ u_\beta \end{bmatrix} + \begin{bmatrix} -\dfrac{1}{L_s} & 0 \\ 0 & -\dfrac{1}{L_s} \end{bmatrix} \begin{bmatrix} e_\alpha \\ e_\beta \end{bmatrix} \tag{5.11}$$

where e_α and e_β represent the back electromotive force (EMF) which can be denoted as:

$$\begin{bmatrix} e_\alpha \\ e_\beta \end{bmatrix} = \begin{bmatrix} -\Psi_f p\omega_m \sin\theta \\ \Psi_f p\omega_m \cos\theta \end{bmatrix} \tag{5.12}$$

where ω_m is rotor mechanical angular speed, p is the number of pole pairs. It can be seen that the back EMF of the motor contains the position information, which is the prerequisite to calculate the rotor position by the use of SM observer.

b) Traditional position observer

According to the SM controller construction method [16], The SM observer for back EMF estimation of the PMSM system (5.11) can be represented as:

$$\begin{bmatrix} \dfrac{\mathrm{d}i_\alpha^*}{\mathrm{d}t} \\ \dfrac{\mathrm{d}i_\beta^*}{\mathrm{d}t} \end{bmatrix} = \begin{bmatrix} -\dfrac{R_s}{L_s} & 0 \\ 0 & -\dfrac{R_s}{L_s} \end{bmatrix} \begin{bmatrix} i_\alpha^* \\ i_\beta^* \end{bmatrix} + \begin{bmatrix} \dfrac{1}{L_s} & 0 \\ 0 & \dfrac{1}{L_s} \end{bmatrix} \begin{bmatrix} u_\alpha \\ u_\beta \end{bmatrix} - \begin{bmatrix} \dfrac{k_c}{L_s} & 0 \\ 0 & \dfrac{k_c}{L_s} \end{bmatrix} \begin{bmatrix} F(\overline{i_\alpha}) \\ F(\overline{i_\beta}) \end{bmatrix} \tag{5.13}$$

where i_α^*, i_β^* are the estimated current in the stationary reference frame. k_c is a constant,

representing the on-off gain and in order to keep the SM observer stable. $\overline{i_\alpha}$ and $\overline{i_\beta}$ represent the errors between the estimated currents and the real currents, that is,

$$\begin{aligned}\overline{i_\alpha} &= i_\alpha^* - i_\alpha \\ \overline{i_\beta} &= i_\beta^* - i_\beta\end{aligned} \tag{5.14}$$

And the sliding surfaces **S** are defined as:

$$\mathbf{S} = \begin{bmatrix} S_\alpha \\ S_\beta \end{bmatrix} = \begin{bmatrix} \overline{i_\alpha} \\ \overline{i_\beta} \end{bmatrix} = 0 \tag{5.15}$$

For the traditional SM observer, $F(\overline{i_\alpha})$ and $F(\overline{i_\beta})$ are signum functions of which performance is shown in Fig.5-4.

$$\begin{bmatrix} F(\overline{i_\alpha}) \\ F(\overline{i_\beta}) \end{bmatrix} = \begin{bmatrix} sign(\overline{i_\alpha}) \\ sign(\overline{i_\beta}) \end{bmatrix} \tag{5.16}$$

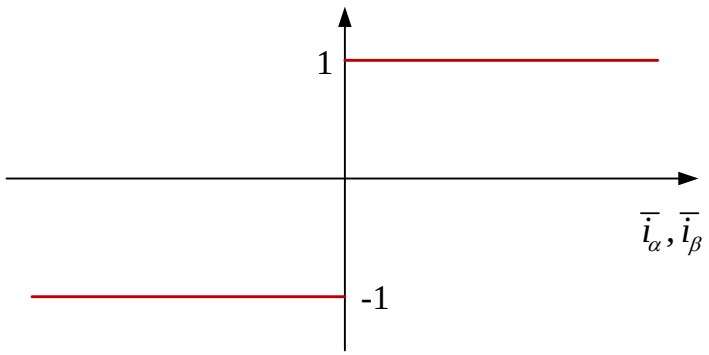

Fig. 5-4. Properties of signum functions.

According to the equations (5.11) and (5.13), if the system is able to reach a stable state [17], the estimated back EMF e_α^* and e_β^* can be written as:

$$\begin{bmatrix} e_\alpha^* \\ e_\beta^* \end{bmatrix} = k_c \cdot \begin{bmatrix} F(\overline{i_\alpha}) \\ F(\overline{i_\beta}) \end{bmatrix} \tag{5.17}$$

c) Stability analysis

According to the Lyapunov stability criterion, the following equation is necessary to be analyzed for stability analysis:

$$V = \frac{1}{2} \cdot \mathrm{S}^T \cdot \mathrm{S} = \frac{1}{2} \bar{i}_\alpha^{\,2} + \frac{1}{2} \bar{i}_\beta^{\,2} \tag{5.18}$$

Obviously, $V > 0$. So only when $\frac{\mathrm{d}V}{\mathrm{d}t} < 0$ will we conclude that the SM observer is stable. Take the time derivative of equation (5.18):

$$\frac{\mathrm{d}V}{\mathrm{d}t} = \mathrm{S}^T \cdot \frac{\mathrm{dS}}{\mathrm{d}t} = \bar{i}_\alpha \frac{\mathrm{d}\bar{i}_\alpha}{\mathrm{d}t} + \bar{i}_\beta \frac{\mathrm{d}\bar{i}_\beta}{\mathrm{d}t} \tag{5.19}$$

Substitute (5.11) and (5.13) into (5.19), it can be further deduced:

$$\frac{\mathrm{d}V}{\mathrm{d}t} = \begin{bmatrix} \bar{i}_\alpha & \bar{i}_\beta \end{bmatrix} \begin{bmatrix} -\frac{R_s}{L_s} \bar{i}_\alpha + \frac{1}{L_s}(e_\alpha - k_c F(\bar{i}_\alpha)) \\ -\frac{R_s}{L_s} \bar{i}_\beta + \frac{1}{L_s}(e_\beta - k_c F(\bar{i}_\beta)) \end{bmatrix} \tag{5.20}$$

And the polynomial expression of (5.20) is:

$$\frac{\mathrm{d}V}{\mathrm{d}t} = \underbrace{[-(\frac{R_s}{L_s} \bar{i}_\alpha^{\,2} + \frac{R_s}{L_s} \bar{i}_\beta^{\,2})]}_{\text{term1}} + \underbrace{[\frac{1}{L_s}(e_\alpha - k_c F(\bar{i}_\alpha))\bar{i}_\alpha + \frac{1}{L_s}(e_\beta - k_c F(\bar{i}_\beta))\bar{i}_\beta]}_{\text{term2}} \tag{5.21}$$

Obviously, the first term of the equation is less than 0. To keep the SMO stable, the second term should also be less than 0, that is,

$$\begin{cases} (e_\alpha - k_c F(\bar{i}_\alpha))\bar{i}_\alpha < 0 \\ (e_\beta - k_c F(\bar{i}_\beta))\bar{i}_\beta < 0 \end{cases} \tag{5.21}$$

Since the signum function is either -1 or 1, it can be further deduced that:

$$\begin{cases} e_\alpha < k_c \\ e_\beta < k_c \end{cases} \text{when } \bar{i}_\alpha, \bar{i}_\beta > 0$$
$$\begin{cases} -e_\alpha < k_c \\ -e_\beta < k_c \end{cases} \text{when } \bar{i}_\alpha, \bar{i}_\beta < 0 \quad \textbf{(5.22)}$$

Therefore, the observer gain that meets the following criteria must keep the observer stable:

$$k_c > \max(|e_\alpha|, |e_\beta|) \quad \textbf{(5.23)}$$

d) Chattering effect attenuation

The conventional SM observer uses the signum function as the switching function, leading to inevitable chattering phenomenon when the system states go through the sliding surface from one side to another. In order to attenuate the adverse effect of chattering on the accuracy of position calculation, a low pass filter (LPF) is commonly adopted to filter the estimated back EMF signals [18-20]. The LPF can be described as:

$$G_{LPF}(s) = \frac{\omega_c}{s + \omega_c} \quad \textbf{(5.24)}$$

where ω_c is the cutting-off frequency. However, the inherent delay attribute of an LPF might bring about errors between the real and estimated values. At the moment, an additional position compensator which is related to the rotating speed should be designed, as in Fig.5-5. Overall, the main defect of this method is that the sensorless control topology becomes more complex. Currently, it is proven that the LPF can be eliminated by replacing the discontinuous signum function with a continuous saturation function for chattering reduction depending on the boundary layer law [21-22]. However, literature [23] indicates that this method is not very satisfying because the chattering might still exist with large uncertainties, and a fuzzy system which acts like a saturation function with a nonlinear slope inside the boundary is presented to tackle the problem. But in practice, it is usually tedious to tune the parameters of the fuzzy system.

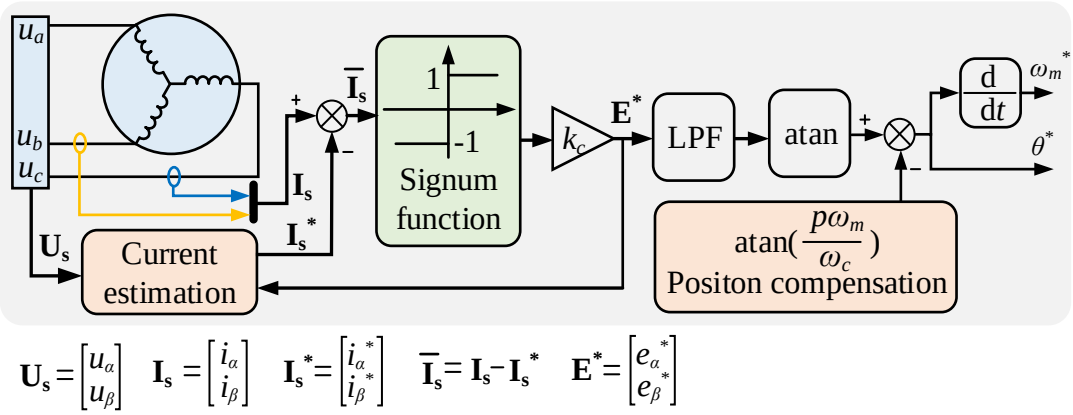

Fig. 5-5. Traditional SM observer structure.

5.2.2 Improved SM Observer for Position Estimation

Fundamentally, the LPF delay issue of the classic SM observer arises from the chattering effect disposition method, so an effective solution is to reduce the undesirable chattering without using an LPF. This section proposes a novel SM observer which utilizes a sigmoid function as the switching function, requiring neither an LPF nor an extra compensator any longer.

With reference to literature [23], this research aims to reduce the chattering phenomenon of SMO by smoothing out the control discontinuity and the step change within a boundary layer near the sliding surface. To achieve it and gain better performance, the switching function should satisfy the following requirements: a) The function is continuous. b) Referring to the saturation function, the upper and lower limit are 1 and -1. c) The slope within the boundary is nonlinear. d) The function has no time-delay characteristic.

A sigmoid function with the expression of (5.25) is totally qualified, so it will be used to replace the signum function for the new SM observer in this chapter.

$$\begin{bmatrix} F(\bar{i}_\alpha) \\ F(\bar{i}_\beta) \end{bmatrix} = \begin{bmatrix} \dfrac{2}{1+\exp(-\bar{i}_\alpha)} - 1 \\ \dfrac{2}{1+\exp(-\bar{i}_\beta)} - 1 \end{bmatrix} \tag{5.25}$$

Since a new switching function is adopted in the SM observer, it is crucial to reappraise the stability of the observer. The same to the traditional method, the expression of (5.21) can be

obtained, too. But different from the signum function in the traditional method, the sigmoid function is in a range of (-1, 1) rather than -1 or 1. Then, in order to keep the observer stable, , the observer gain will be derived to meet the following criteria:

$$k_c > \max(|\frac{e_\alpha}{F(\bar{i}_\alpha)}|,|\frac{e_\beta}{F(\bar{i}_\beta)}|) \quad \textbf{(5.26)}$$

Clearly, the stability condition differs from (5.23), and it can be noted that k should be much larger because $|F|$ is less than 1 over the boundary layer range. In practice, $\bar{i}_\alpha$ and $\bar{i}_\beta$ are the estimation errors, and referring to the sliding mode theory, they will fluctuate mostly around the sliding surfaces with small variations with the range of tolerance. Manually define the lower tolerance as ξ, which is:

$$\min(|\bar{i}_\alpha|,|\bar{i}_\beta|) = \xi \quad \textbf{(5.27)}$$

And the minimum $|F|$ can be rewritten as:

$$\min|F| = |\frac{2}{1+\exp(-\xi)} - 1| \quad \textbf{(5.28)}$$

Then, the observer gain can be derived as:

$$k_c > \max((|\frac{e_\alpha}{\min|F|}|,|\frac{e_\beta}{\min|F|}|)) \quad \textbf{(5.29)}$$

So, in this research, the observer gain can be selected as:

$$k_c = \frac{2U_{dc}}{\min|F|} \quad \textbf{(5.29)}$$

where U_{dc} is the DC-bus voltage.

The structure of the improved SM observer without using LPF is shown in Fig.5-6. And the estimated position θ^* of the rotor will be calculated from:

$$\theta^* = -\arctan(\frac{e_\alpha^*}{e_\beta^*}) \tag{5.30}$$

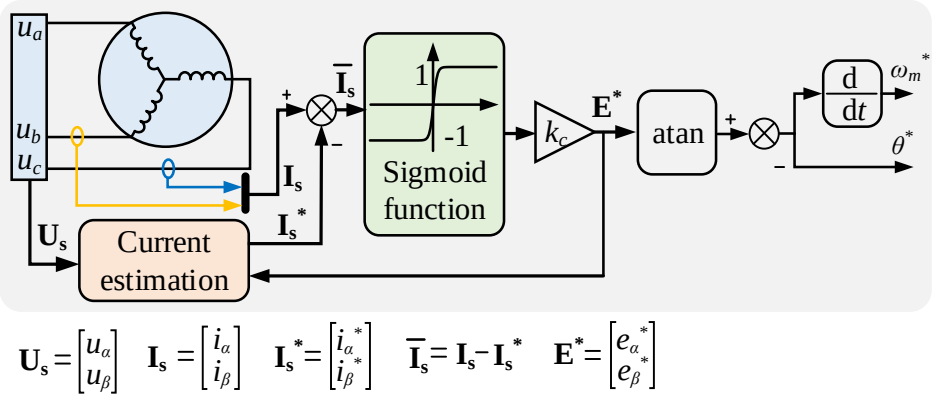

Fig. 5-6. Improved SM observer structure.

5.3 Reliable Winding-based Discharge Algorithm Using Position Estimated by Improved SM Observer

After calculating the rotor position, the winding-based discharge strategy with position sensor fault tolerance capacity can be achieved as in Fig.5-7. Four programmatic virtual switches are utilized to select the operating state of the system. When the system works normally, port 1 is connected and the PMSM drive system is controlled by a double closed-loop speed regulation strategy [24-26]. In this case, the rotor position (θ) used for coordinate transformation is detected by a position sensor. Once an emergency occurs, port 2 is connected and the winding-based discharge algorithm starts to be implemented. At the moment, the rotor position (θ^*) is calculated by the improved SM controller.

During the energy dissipation period, the bus voltage is mainly controlled by a voltage control algorithm, and the detailed discharge process and mechanism are as follows. After an active discharge is requested, a dc bus voltage regulation algorithm is activated to maintain the bus voltage ten percent lower (U_{ref}) than the safe voltage until the machine speed decreases under the threshold ω_{th} where the machine back-EMF is equal to 60 V. In detail, a voltage controller is adopted to produce the d-axis reference current i_{d_ref} which can regulate the magnitude of the air-gap magnetic field of the IPMSM according to the error between U_{ref} and the capacitor

voltage U_c. Although all of the residual energy stored in the system can be consumed in the form of winding loss by only injecting d-axis current to the machine, the rotor speed declines slowly because the rotor inertia is usually large and no braking torque is produced, and thus the discharge time will still be very long (dozens of seconds). In this research, in order to take full advantage of the maximum discharge capacity of the drive system so as to shorten the discharge time, the current is expected to be controlled to maintain at the system safe current I_{max} in this stage, that is,

$$i_{q\_ref} = -\sqrt{I_{max}{}^2 - i_{d\_ref}{}^2} = -\sqrt{I_{max}{}^2 - i_d{}^2} \tag{5.31}$$

where i_{q_ref} is the q-axis reference current. In this case, a negative q-axis current is used to accelerate the discharge rate.

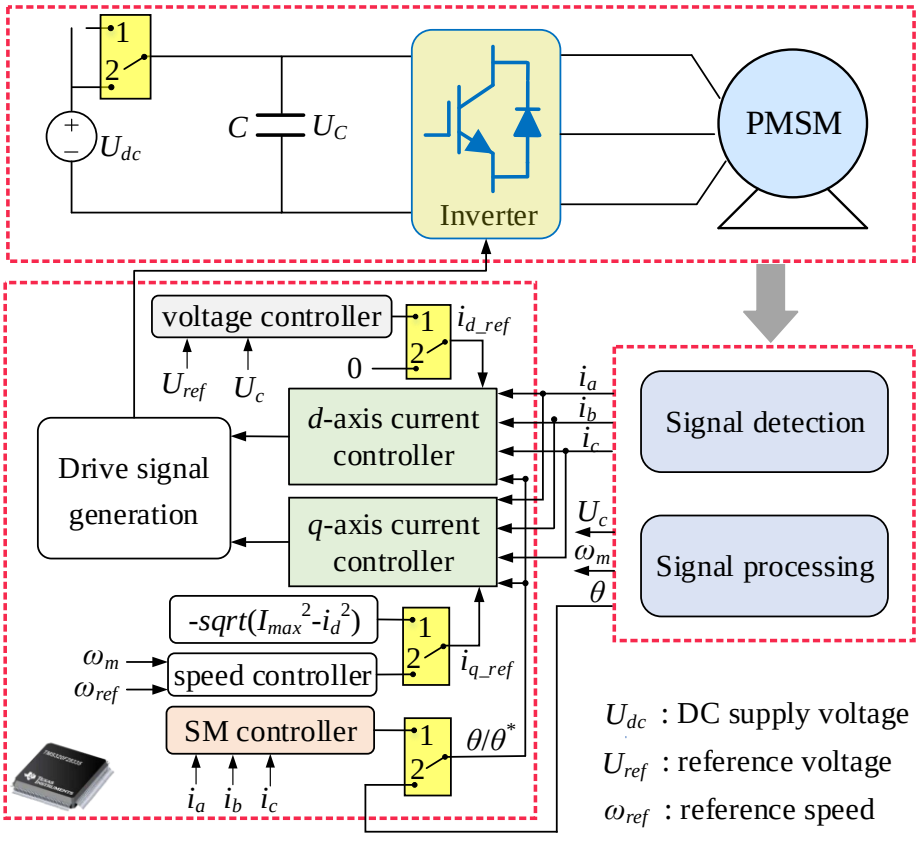

Fig. 5-7. Block diagram of the reliable discharge method using estimated position information.

5.4 Simulation and Experimental Verifications

Simulation and experiments are conducted on a three-phase IPMSM whose parameters are consistent with those in chapter 4. Differently, without using battery pack for source, a DC power supply which is available at 310 V is employed. Four thin-film capacitors, DHF DAWNCAP 140 μF, are connected in parallel to compose the desired 560 μF DC-bus capacitor. The proposed discharge algorithm is implemented on DSP TMS320X28335 controller board. The real rotor position is detected by a rotary transformer. Hall current sensors, HNC-100LT, are used to measure three-phase currents while the motor *d*, *q*-axis currents are calculated by the digital controller. The DC-bus voltage is measured by a voltage transducer LV25-P. Using the USB-RS485 communication interface, the collected data are transmitted to and further recorded by the host computer.

The active discharge starts when the motor speed is at the rated value ω_{rated} from 0.5 s. Both the simulation and experimental results in Fig.5-8 show that when the voltage regulation algorithm is started, the capacitor voltage drops under 60 V quickly and levels off until about 3.2 s (discharge time is 2.7 s). After then, the voltage and speed fall to zero soon. As in Fig.5-9, a *d*-axis current of about -65 A and a gradually increased *q*-axis current are applied to maintain the bus voltage at 54 V when the *d*, *q*-axis currents are relatively low. As the rotor speed goes down to a very low level, the *q*-axis current will rise sharply (relatively high voltage range), trying to hold the voltage at the reference value. Although the maximum discharge capacity of the system is not exerted completely, and only a small negative *q*-axis current is produced without tracking the prescribed trajectory, the overall discharge time (from 310 V to 0) has been limited within 2.8 s.

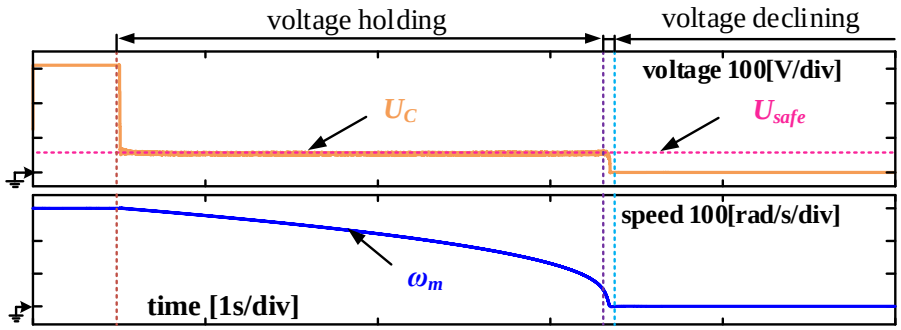

(a)

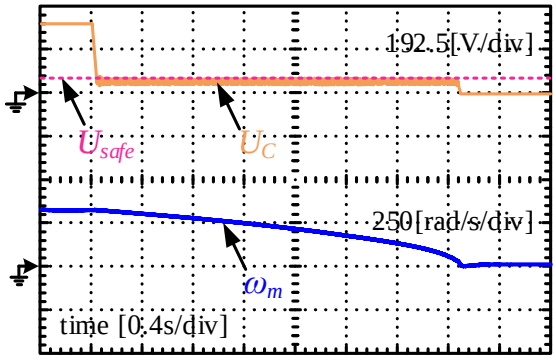

(b)

Fig. 5-8. Discharge characteristics of DC-bus capacitor voltage and machine speed. (a) Simulation results. (b) Experimental results.

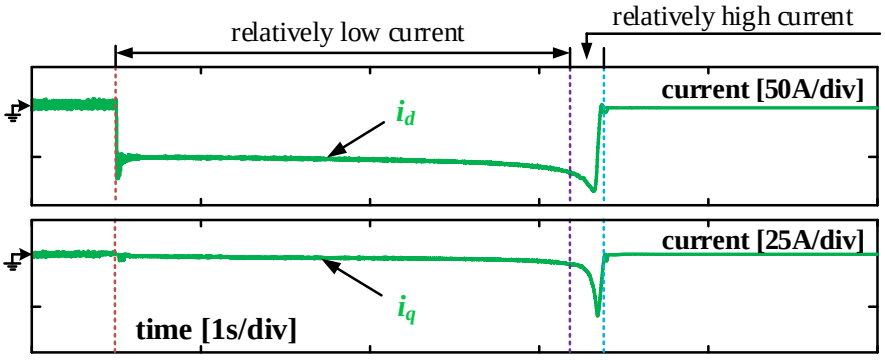

(a)

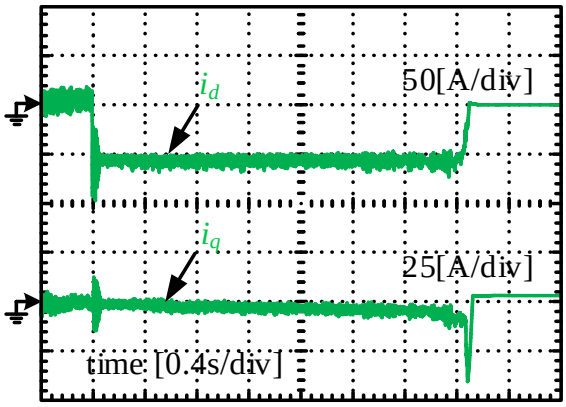

(b)

Fig. 5-9. Discharge characteristics of *d*, *q*-axis currents. (a) Simulation results. (b) Experimental results.

The estimated rotor position and the transient estimation error between 1.1 s and 1.13 s are

illustrated in Fig.5-10. From the figure, it can be noticed that the proposed back EMF sliding mode observer can track the actual position with small estimation error that is within ±10 degree (all angles are electrical angles) in the capacitor voltage bleeding course, and the chattering phenomenon is not visible at all.

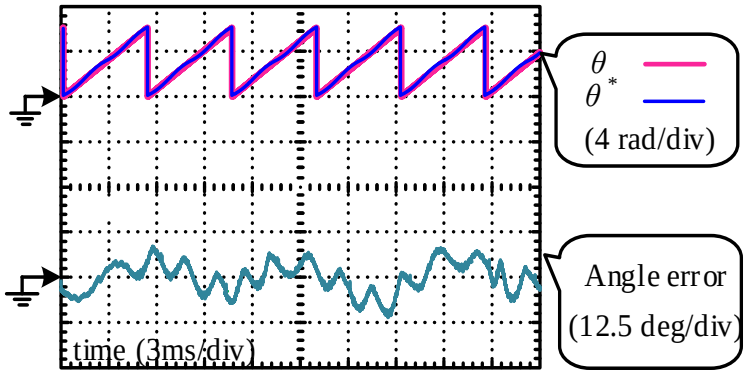

Fig. 5-10. Experimental results of position estimated by the improved sliding mode controller during discharge process.

5.5 Summary

This chapter proposes a more reliable winding-based discharge algorithm based on sensorless control technique. This topic is related to the EV safety improvement in the post-crash situations. In the first place, the principle of the traditional signum-function based SM observer is introduced. In order to attenuate the chattering effect of SM observer without using an LPF, an improved SM controller that adopts a sigmoid function as the switching function is presented to calculate the rotor position. The stability of the improved observer is analyzed in an innovative way according to the Lyapunov criterion. Then, the high-reliability discharge algorithm using estimated position is introduced. The algorithm has considered the PMSM as a generator and regulated its output voltage by applying nonzero *d*, *q*-axis currents using a voltage control algorithm. Both the simulation and experimental results prove that the proposed position sensor fault handling strategy and the discharge method are effective.

5.6 References

[1] United Nation Economic Commission for Europe Vehicle Regulation, No.94 (ECE R94), Unifrom provisions concerning the approval of vehicles with regard to the protection of the occupants in the event of a frontal collision, Rev. 2, Annex 11, Aug. 2013.

[2] K. Benson, "Regeneration for AC drive systems," Proceedings of 1994 IEEE/IAS Annual Textile, Fiber and Film Industry Technical Conference, Greenville, SC, 1994, pp. 1-3.

[3] C. Gong, Y. Hu, G. Chen, H. Wen, Z. Wang and K. Ni, "A DC-Bus Capacitor Discharge Strategy for PMSM Drive System with Large Inertia and Small System Safe Current in EVs," in *IEEE Transactions on Industrial Informatics*. doi: 10.1109/TII.2019.2895317

[4] T S. Ashida, K. Yamada, M. Nakamura, T. Shimana, and T. Soma, "Electric vehicle, and control apparatus and controlmethod for electric vehicle," U.S. Patent 8631894 B2, Jan. 21, 2014.

[5] Z. Ke, J. Zhang and M. W. Degner, "DC Bus Capacitor Discharge of Permanent-Magnet Synchronous Machine Drive Systems for Hybrid Electric Vehicles," in *IEEE Transactions on Industry Applications*, vol. 53, no. 2, pp. 1399-1405, March-April 2017.

[6] T. Goldammer, T. Le, J. Miller, and J. Wai, "Active high voltage bus bleed down," U.S. Patent 20120161679 A1, Jun. 28, 2012

[7] S. Chen, G. Liu and L. Zhu, "Sensorless Control Strategy of a 315 kW High-Speed BLDC Motor Based on a Speed-Independent Flux Linkage Function," in *IEEE Transactions on Industrial Electronics*, vol. 64, no. 11, pp. 8607-8617, Nov. 2017.

[8] D. Nguyen, R. Dutta, M. F. Rahman and J. E. Fletcher, "Performance of a Sensorless Controlled Concentrated-Wound Interior Permanent-Magnet Synchronous Machine at Low and Zero Speed," in *IEEE Transactions on Industrial Electronics*, vol. 63, no. 4, pp. 2016-2026, April 2016.

[9] W. Li, J. Fang, H. Li and J. Tang, "Position Sensorless Control Without Phase Shifter for High-Speed BLDC Motors With Low Inductance and Nonideal Back EMF," in *IEEE Transactions on Power Electronics*, vol. 31, no. 2, pp. 1354-1366, Feb. 2016.

[10] M. Seilmeier and B. Piepenbreier, "Sensorless Control of PMSM for the Whole Speed Range Using Two-Degree-of-Freedom Current Control and HF Test Current Injection for Low-Speed Range," in *IEEE Transactions on Power Electronics*, vol. 30, no. 8, pp. 4394-4403, Aug. 2015.

[11] E. Al-nabi, B. Wu, N. R. Zargari and V. Sood, "Sensorless Control of CSC-Fed IPM Machine for Zero- and Low-Speed Operations Using Pulsating HFI Method," in *IEEE Transactions on Industrial*

Electronics, vol. 60, no. 5, pp. 1711-1723, May 2013.

[12] S. K. Kommuri, S. B. Lee and K. C. Veluvolu, “Robust Sensors-Fault-Tolerance With Sliding Mode Estimation and Control for PMSM Drives,” in *IEEE/ASME Transactions on Mechatronics*, vol. 23, no. 1, pp. 17-28, Feb. 2018.

[13] T. Bernardes, V. F. Montagner, H. A. Gründling and H. Pinheiro, “Discrete-Time Sliding Mode Observer for Sensorless Vector Control of Permanent Magnet Synchronous Machine,” *in IEEE Transactions on Industrial Electronics*, vol. 61, no. 4, pp. 1679-1691, April 2014.

[14] Q. Yuan, H. Wu, J. Qian and B. Zhang, "Research on Sensorless Control of Permanent Magnet Synchronous Motor Based on Novel Sliding Mode Observer," *2018 Asia-Pacific Magnetic Recording Conference (APMRC)*, Shanghai, 2018, pp. 1-2.

[15] D. FEREKA, M. ZERIKAT and A. BELAIDI, "MRAS Sensorless Speed Control of an Induction Motor Drive based on Fuzzy Sliding Mode Control," *2018 7th International Conference on Systems and Control (ICSC)*, Valencia, 2018, pp. 230-236.

[16] Y. Jie, W. Qing-Lin and L. Yuan, "Sliding mode variable structure control theory: A survey," *Proceedings of the 31st Chinese Control Conference*, Hefei, 2012, pp. 3197-3202.

[17] M. Cui, C. Zhang, and J. Zhu, "Realization of PMSM adjustable speed system based on sliding mode control," *2012 24th Chinese Control and Decision Conference (CCDC)*, Taiyuan, 2012, pp. 435-438.

[18] Y. Fan, L. Zhang, M. Cheng and K. T. Chau, “Sensorless SVPWM-FADTC of a New Flux-Modulated Permanent-Magnet Wheel Motor Based on a Wide-Speed Sliding Mode Observer,” in *IEEE Transactions on Industrial Electronics*, vol. 62, no. 5, pp. 3143-3151, May 2015.

[19] Q. Lu, X. Zhu, L. Quan, Y. Zuo and S. Du, “Rotor position estimation scheme with harmonic ripple attenuation for sensorless controlled permanent magnet synchronous motors,” in *IET Electric Power Applications*, vol. 12, no. 8, pp. 1200-1206, 9 2018.

[20] Y. Feng, J. Zheng, X. Yu and N. V. Truong, “Hybrid Terminal Sliding-Mode Observer Design Method for a Permanent-Magnet Synchronous Motor Control System,” in *IEEE Transactions on Industrial Electronics*, vol. 56, no. 9, pp. 3424-3431, Sept. 2009.

[21] Y. K. Kim and C. H. Paek, “Position Error Reduction of the Actuator Using the Sliding Mode Controller with Variable Boundary Layer Thickness,” *2006 SICE-ICASE International Joint Conference*, Busan, 2006, pp. 4905-4910..

[22] X. Zhang, “Sensorless Induction Motor Drive Using Indirect Vector Controller and Sliding-Mode Observer for Electric Vehicles,” in *IEEE Transactions on Vehicular Technology*, vol. 62, no. 7, pp. 3010-

3018, Sept. 2013.

[23] A. Saghafinia, H. W. Ping, M. N. Uddin and K. S. Gaeid, “Adaptive Fuzzy Sliding-Mode Control Into Chattering-Free IM Drive,” in *IEEE Transactions on Industry Applications*, vol. 51, no. 1, pp. 692-701, Jan.-Feb. 2015.

[24] L. Sun, X. Wang, Z. Deng and Q. Ding, “Research on stable regions of double-closed loop system for PMSM with low-pass filters,” 2014 17th International Conference on Electrical Machines and Systems, Hangzhou, 2014, pp. 1150-1156.

[25] C. Gan, Q. Sun, J. Wu, W. Kong, C. Shi, and Y. Hu, “MMC-based SRM drives with decentralized battery energy storage system for hybrid electric vehicles,” in IEEE Transactions on Power Electronics, vol. 34, no. 3, pp. 2608-2621, Mar. 2019.

[26] C. Gan, J. Wu, M. Shen, S. Yang, Y. Hu, and W. Cao, “Investigation of skewing effects on the vibration reduction of three-phase switched reluctance motors,” in IEEE Transactions on Magnetics, vol. 51, no. 9, pp. 1-9, Sep. 2015.

Chapter 6 High-Reliability Multi-Objective Model Predictive Control Strategy for PMSM based EVs

Chapter 2 has illustrated that the reliable control strategies are very important to the functional safety of EVs. Because the MPC algorithms have very simple structure and comply with the optimal control principle, they have high reliability to maintain the system to operate safely. This chapter proposes a new finite control set model predictive control (FCS-MPC) strategy that simultaneously evaluates two targeting control objectives (TCOs) including speed and currents in a single cost function, achieving high-performance single-closed-loop (simpler than the traditional double-closed loop FCS-MPC methods) control structure. In this chapter, a machine model that is specially designed for the multi-objective FCS-MPC operation is illustrated at first. Then, a new cost function which can evaluate the tracking performance of speed and *d*-axis current and steady-state performance of *q*-axis current is developed. Compared to the conventional FCS-MPC approaches, extra speed controllers are not needed so that the proposed control topology becomes simpler. The proposed multi-objective FCS-MPC approach is verified by both simulation and experiments.

6.1 Introduction

Since permanent magnet machines (PMSMs) have been heavily adopted in EVs, good operation properties (e.g., high dynamic and steady-state characteristics, low current and torque ripple) are highly required in these applications, placing intensive demands upon high-performance control strategies [1-5].

Due to the merits of quick response, excellent constraint handling capability and optimum control principle, model predictive control (MPC) which was proposed in 1970s has been developed significantly in the field of motor drive [6-7]. For example, MPC-based controllers have been designed to achieve various functions in the machine control systems. In [8] and [9], MPC is incorporated into the direct torque control (DTC) methods, predicting and regulating

the electromagnetic torque and flux of the PMSMs. Paper [10] proposes a model predictive power control (MPPC) method for a permanent magnet synchronous generator (PMSG) to enhance the steady-state performance of the system. In addition, a new model predictive speed controller (MPSC) endowed with the function of constrained state feedback is introduced to achieve modest speed control dynamic in [11]. Another popular application is model predictive current control (MPCC), in which the currents are set as the targeting control objectives (TCO) [12-15]. In comparison with MPSC, the current ripples of the MPCC become lower without markedly sacrificing the dynamic performance. The above-mentioned MPC algorithms can be classified into two generic groups [16]. One extends on the conventional proportional-integral (PI) based vector control by replacing the PI controllers with one or more MPC-based controllers but still retaining a modulator to generate pulse width modulation (PWM) signals, like [12-13]. The other totally discards the modulator and directly uses the output of the cost function to determine the optimal converter switching states, as in [14]-[15]. Comparatively speaking, the latter scheme, known as finite control set MPC (FCS-MPC), is much easier to implement, benefiting from a voltage vector look-up table which can be obtained off-line. At present, the FCS-MPC strategies are attracting increasing attention in the PMSM drive applications [17-21].

Concerning the different TCOs included in the cost functions, there exist two types of commonly used FCS-MPC techniques: multi-objective FCS-MPC and single-objective FCS-MPC. The FCS model predictive torque control (FCS-MPTC), whose TCOs are the torque and flux, is the typical application of the multi-objective FCS-MPC theories [17-18]. In the FCS-MPTC-based control systems, extra speed controllers (e.g., PI controller) are required for tracking the reference speed ω_m^* and generating the reference torque. When it comes to the single-objective FCS-MPC approaches, the MPCC-based controller in which the current is the only TCO is the most intensively studied topic [19-20]. Similar to the FCS-MPTC method, the speed regulators cannot be eliminated either because they should be used for q-axis reference current i_q^* generation, as shown in Fig.6-1. Unluckily, the speed controllers contribute much to the complexity of the drive topology, and it is an uphill task to tune the parameters of them because of lacking theoretical design procedures for the multi-type-controller based systems. In order to simplify the control topology, [21] develops a new single-objective MPC method by only using one FCS-MPSC-based controller. This method only contains the speed control

loop in the topology, resulting in that neither the steady-state nor dynamic characteristics of the other machine states (e.g., current and torque) will be evaluated simultaneously. Overall, there are few studies focusing on controlling the whole PMSM system by just using one multi-objective FCS-MPC-based controller.

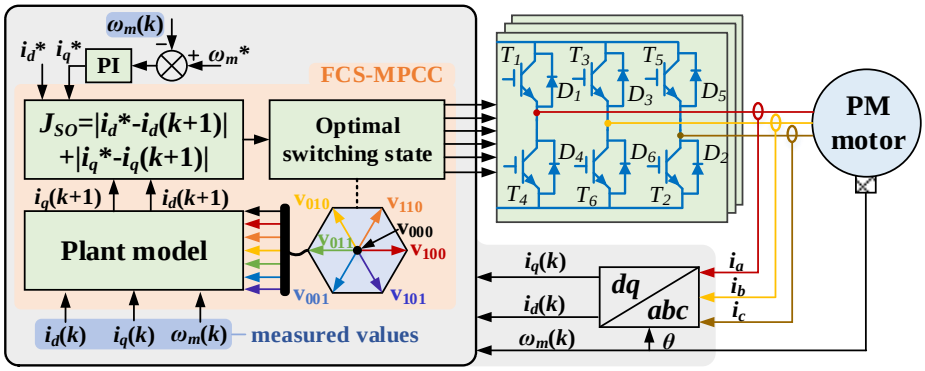

$i_{d,q}$: d, q-axis currents, $i_{d,q}^*$: reference d, q-axis currents, **v**: candidate voltages
ω_m: speed, ω_m^*: reference speed, θ: position, i_a, i_b, i_c: phase currents

Fig. 6-1. Structure of an FCS-MPCC-based drive system.

A main purpose of this chapter is to design an FCS-MPC-based controller that can meanwhile take multiple TCOs (speed and current) into account, achieving high-performance single-closed-loop control structure. A hybrid cost function, which is based on speed and current errors is developed to select the best control voltage vector. In comparison with traditional single-objective FCS-MPC, no extra speed controllers are employed in the new method. Hence, the proposed control scheme becomes simpler and more reliable.

6.2 Model for Multi-objective FCS-MPC

State-space model which comprises no less than one differential equation is capable of accurately reflecting the transient behaviors of a multivariable system, making itself well-suited for PMSM MPC applications with further reference to the non-linearization and strong coupling properties. The state-space model which describes the electrical and mechanical dynamics of a PMSM in the direct-quadrature (dq) rotating frame is as follows, where the iron saturation and hysteresis loss are assumed negligible [16]:

$$\frac{\mathrm{d}i_d}{\mathrm{d}t} = -\frac{R_s}{L_d} i_d + \frac{L_q}{L_d} p\omega_m i_q + \frac{u_d}{L_d} \tag{6.1}$$

$$\frac{\mathrm{d}i_q}{\mathrm{d}t} = -\frac{L_d}{L_q} p\omega_m i_d - \frac{R_s}{L_q} i_q + \frac{u_q}{L_q} - \frac{\Psi_f}{L_q} p\omega_m \tag{6.2}$$

$$\frac{\mathrm{d}\omega_m}{\mathrm{d}t} = \frac{1}{J}(1.5p(\Psi_f i_q + (L_d - L_q) i_d i_q) - T_l) \tag{6.3}$$

where i_d, i_q are stator dq-axis currents and u_d, u_q are dq-axis the control voltages. L_d, L_q are dq-axis inductance, and L_d=L_q for a surface-mounted PMSM. The stator winding resistance is R_s. T_l and ω_m are the load torque and rotor mechanical angular speed, respectively. Then, p represents the number of pole pairs and Ψ_f is flux linkage. J is the rotor inertia.

In order to predict the future states, the continuous domain model must be discretized in a time step of T (switching period). When the forward Euler discretization is applied to (6.1) and (6.2), the predicting plant model (PPM) can be expressed as:

$$i_d(k+1) = \frac{L_d - TR_s}{L_d} i_d(k) + \frac{TL_q p}{L_d} \omega_m(k) i_q(k) + \frac{T}{L_d} u_d(k) \tag{6.4}$$

$$i_q(k+1) = -\frac{TL_d p}{L_q} \omega_m(k) i_d(k) + \frac{L_q - TR_s}{L_q} i_q(k) + \frac{T}{L_q} u_q(k) - \frac{T\Psi_f p}{L_q} \omega_m(k) \tag{6.5}$$

where i_d (k), i_q (k) and $\omega_m(k)$ are the states at the kth sampling instant. i_d (k+1) and i_q (k+1) are the predicting values at the (k+1)th period (t_{k+1}). The discretization operation cannot be applied to (6.3) because the speed alteration within the kth period is not directly determined by the manipulated variables $u_d(k)$ and $u_q(k)$, but it is a direct consequence of the overall currents in the cycle rather than just the initial currents at t_k. Considering this, take definite integral of (6.3) between t_k and t_{k+1} and the PPM for speed estimation turns:

$$\omega_m(k+1) = \frac{1.5p\Psi_f}{J} \int_{t_k}^{t_{k+1}} i_q \mathrm{d}t + \frac{L_d - L_q}{J} \int_{t_k}^{t_{k+1}} i_d i_q \mathrm{d}t - \frac{1}{J} \int_{t_k}^{t_{k+1}} T_l \mathrm{d}t + \omega_m(k) \tag{6.6}$$

where $\omega_m(k+1)$ is the speed at t_{k+1}. Usually, the switching period T is very short, so an

appropriate equivalence that i_q and $i_d i_q$ experience linear changes under the control of $u_d(k)$ and $u_q(k)$, and the external load torque T_l remains constant at $T_l(k)$ over the period can be made. In this case, (6.6) can be rewritten as:

$$\begin{aligned}\omega_m(k+1) = &\frac{3p\Psi_f T}{4J}(i_q(k+1)-i_q(k)) - \frac{T_l(k)T}{J} + \omega_m(k) \\ &+ \frac{(L_d - L_q)T}{2J}(i_d i_q(k+1) - i_d i_q(k))\end{aligned} \tag{6.7}$$

Obviously, when predicting the speed state, the future currents should be calculated by (6.4) and (6.5) in advance. It should be addressed that only by doing this can $\omega_m(k+1)$ be associated with the manipulated voltages.

As for the candidate control voltages, in practice, a total of seven phase voltage vectors ($\mathbf{v}_{000}$, $\mathbf{v}_{100}$, $\mathbf{v}_{110}$, $\mathbf{v}_{010}$, $\mathbf{v}_{011}$, $\mathbf{v}_{001}$, $\mathbf{v}_{101}$) are among the alternatives for a two-level inverter:

$$\mathbf{v}_{s_a s_b s_c} = \begin{bmatrix} v_a \\ v_b \\ v_c \end{bmatrix} = \frac{V_{dc}}{3}\begin{bmatrix} 2 & -1 & -1 \\ -1 & 2 & -1 \\ -1 & -1 & 2 \end{bmatrix}\begin{bmatrix} s_a \\ s_b \\ s_c \end{bmatrix} \tag{6.8}$$

where $[s_a, s_b, s_c]^T$ consisting of $[0, 0, 0]^T$, $[1, 0, 0]^T$, $[1, 1, 0]^T$, $[0, 1, 0]^T$, $[0, 1, 1]^T$, $[0, 0, 1]^T$ and $[1, 0, 1]^T$ are the switching states. V_{dc} is the DC-link voltage. $[v_a, v_b, v_c]^T$ are the terminal phase voltages. By means of *abc*/*dq* transformation, the control voltage sets to be substituted into PPM for prediction can be expressed as:

$$\begin{bmatrix} u_d(k) \\ u_q(k) \end{bmatrix} = \frac{2}{3}\begin{bmatrix} \cos\theta & \frac{\sqrt{3}\sin\theta - \cos\theta}{2} & \frac{-\sqrt{3}\sin\theta - \cos\theta}{2} \\ -\sin\theta & \frac{\sin\theta + \sqrt{3}\cos\theta}{2} & \frac{\sin\theta - \sqrt{3}\cos\theta}{2} \end{bmatrix} \cdot \mathbf{v}_{s_a s_b s_c} \tag{6.9}$$

6.3 Multi-Objective FCS-MPC Algorithm

6.3.1 Implementation of Single-Objective FCS-MPC Method

For the sake of comparison, the implementation of single-objective FCS-MPC method is illustrated firstly. The implementation procedures of an FCS-MPC algorithm can be summarized as follows: the measured currents and speed as well as the seven manipulated voltages are substituted into the PPM to predict the next step's states, and then the predicted values are evaluated by a cost function so as to select the optimal control voltage to be applied. In this process, the cost function serves as the key component for optimizing calculation, and it determines whether an FCS-MPC-based controller is a so-called single-objective or multi-objective scheme. In order to clearly compare the differences between a single-objective controller and the proposed approach, the cost function of an FCS-MPCC-based controller (as in Fig.1), which only regards the current as the control target, is demonstrated.

$$J_{SO} = | i_d^* - i_d(k+1) | + | i_q^* - i_q(k+1) | \tag{6.10}$$

where i_d^* is the d-axis reference current and it can be set to 0 if flux-weakening operation is not required. i_q^* is the q-axis reference current.

6.3.2 Structure of Multi-Objective FCS-MPC Method

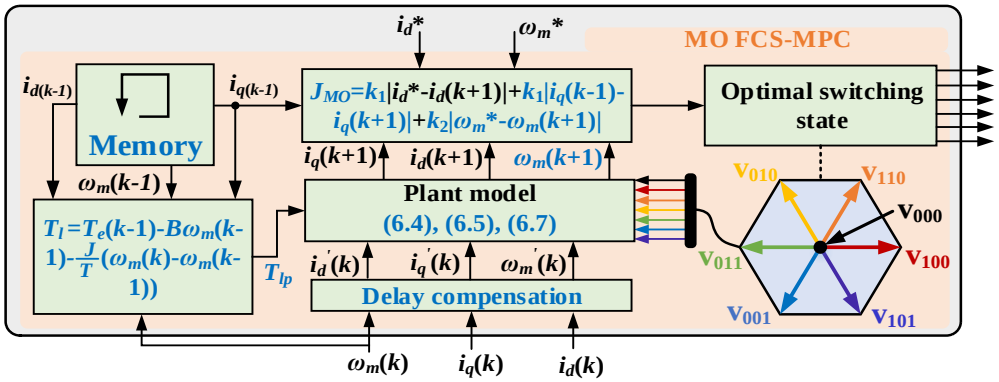

Fig. 6-2. Structure of multi-objective FCS-MPC-based controller.

Fig.6-2 depicts the structure of a dual objective (speed and current) FSC-MPC strategy. In comparison with the single-objective FCS-MPCC method, the explanations of the new algorithm are detailed as follows.

Most crucially, the speed and current performance is assessed by a novel multi-objective cost function:

$$J_{MO} = k_1 | i_d^* - i_d(k+1) | + k_1 | i_q(k-1) - i_q(k+1) | + k_2 | \omega_m^* - \omega_m(k+1) | \quad \textbf{(6.11)}$$

It can be noted that the proposed algorithm aims to track the *d*-axis current and speed references (i_d^* and ω_m^*), but an extra term of absolute error between the previous *q*-axis current $i_q(k\text{-}1)$ and $i_q(k+1)$ is also incorporated into the cost function. The reason for this configuration includes that it is impossible to simultaneously and precisely compel the rotating speed and *q*-axis current to track the manually set references in a PMSM by one sole MPC-based controller, and hence $|i_q^* - i_q(k+1)|$ cannot be integrated into the cost function. But from another point of view, when the machine reaches the equilibrium state in the control process, the *q*-axis current ripples are expected to be furthest reduced so as to improve the steady-state performance of the PMSM. Practically, this performance characteristic can be evaluated by the variations in the adjacent intervals. For the purpose of lowering the fluctuations of the *q*-axis current which is directly related to the output electromagnetic torque, we import $|i_q(k\text{-}1) - i_q(k+1)|$ into the multi-objective cost function. It should be mentioned that because the cost function is able to evaluate both the current and speed characteristics, it is unnecessary to track a *q*-axis reference, so the speed controller is eliminated in the multi-objective FCS-MPC control structure.

Secondly, a load torque observer is integrated into the proposed controller. In equation (6.7), the real-time load torque should be used for predicting the future speed information. But a physical load torque sensor is usually not installed in the PMSM for the sake of cost reduction. In this case, a new issue that how to determine $T_l(k)$ arises. [23] presents a theoretical solution to the problem by designing an observer to estimate T_l, but it does not explain the explicit discretization procedures. In this research, considering that the sampling period *T* is short (typically 0.2 ms), we make an appropriate assumption that the contemporary load torque is equal to that in the (*k*-1)th cycle. Then, a discrete torque estimator can be deduced by applying backward Euler technique to the mechanical dynamic equation, that is:

$$T_{lp}(k) = T_e(k-1) - \frac{J}{T}(\omega_m(k) - \omega_m(k-1)) \quad \textbf{(6.12)}$$

where T_{lp} is the observed load torque, and T_e is the output electromagnetic torque of the machine,

$$T_e(k-1) = 1.5p(\Psi_f i_q(k-1) + (L_d - L_q) i_d(k-1) i_q(k-1)) \quad \textbf{(6.13)}$$

So far, the system control structure becomes simple by using a single multi-objective FCS-MPC-based controller to simultaneously control speed and currents. However, the weighting factors k_1 and k_2 must be adopted to balance the differences between the two kinds of control targets. According to [24], they can be determined using empirical procedures.

6.4 Verifications

The performance of the proposed multi-objective FCS-MPC is tested by the means of simulation and experiments. The motor and control parameters of the PMSM prototype are listed in Table 6-1.

TABLE 6-1
PROTOTYPE SYSTEM PARAMETERS

Parameters	Value	Parameters	Value
motor phase resistance (Ω)	0.6383	rotor inertia (kg·m^2)	0.013
d-axis inductance (mH)	2	DC-link voltage (V)	310
q-axis inductance (mH)	2	sampling time (ms)	0.1
number of pole pairs	4	safety current (A)	20
PM magnetic flux (Wb)	0.085	rated torque (Nm)	5
EMF constant	1.7	rated power (kW)	1.5

6.4.1 Simulation Results

For the sake of comprehensive discussion, the verification procedures for the new method are as follows: the machine speeds up from standstill to 100 rad/s at first, after which it will stabilize until 1.0 s when a constant load of 5 Nm is suddenly applied. From 1.5 s, the reference speed is set as 200 rad/s, while the motor begins to slow down from 2.5 s. After removing the external load at 3.0 s, the rotating speed of the machine continues to decline until it reaches zero. Fig.6-3 illustrates the control performance of the proposed multi-objective FCS-MPC algorithm.

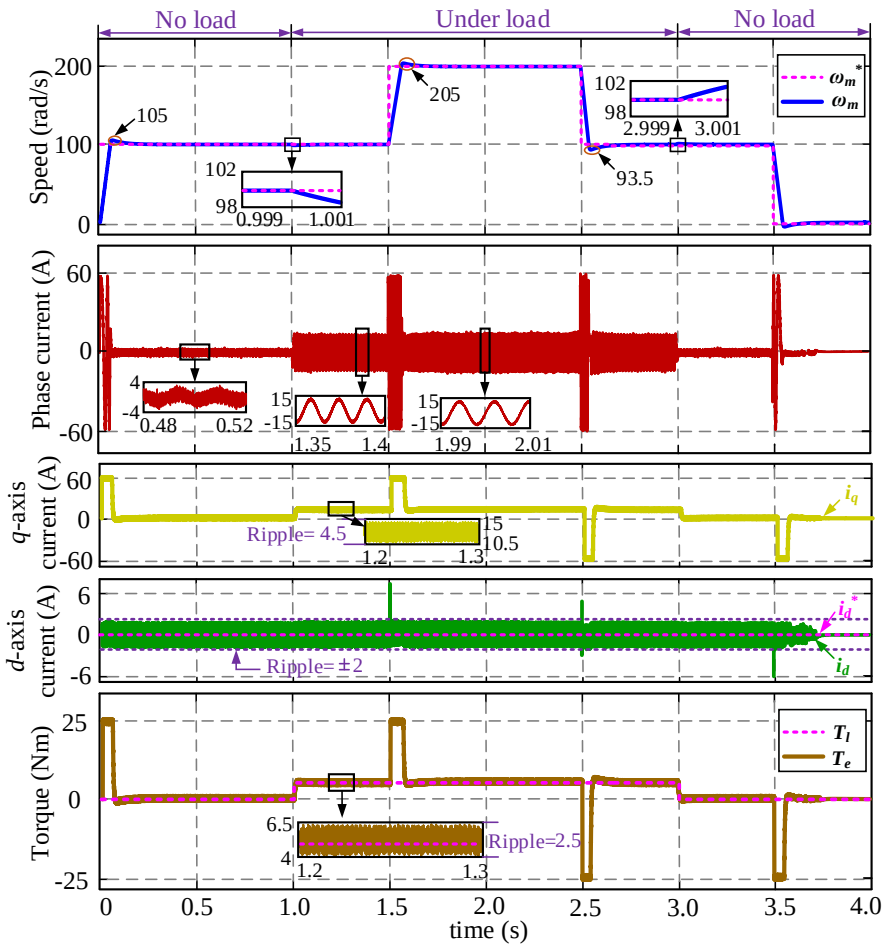

Fig. 6-3. Performance of the proposed multi-objective FCS-MPC algorithm.

***a*) Analysis on steady-state performance**

It can be noted that the motor speed remains stable after it arrives at the setpoint no matter whether the machine is loaded or not during the whole test range. Besides, the average value of the *d*-axis current can level off at zero. These indicate that the proposed multi-objective FCS-MPC has marked speed and current tracking capability without steady-state errors. However, visible current and torque ripples can be witnessed in Fig.6-3. Under load conditions, the peak-to-peak ripple of *q*-axis is 4.5 A, equaling nearly 37.5% of the average value (12 A). The *d*-axis current and torque ripples are about 4 A and 2.5 Nm, respectively. As for the no-load cases, the magnitude of the current and torque ripples stands at very similar position with load conditions. The good steady-state performance of the system shows that the proposed multi-objective FCS-MPC-based controller is totally qualified for regulating speed as well as current without using a speed controller to generate *q*-axis reference current.

***b*) Analysis on dynamic performance**

Dynamic performance evaluation of the control system needs to consider the following aspects, namely, settling time, speed and current overshoot and robustness to abrupt load variation.

During acceleration, the rise time of the proposed MPC algorithm is about 0.1 s regardless of load and no-load conditions. A slight speed overshoot of 5 rad/s can be witnessed, accounting for 5% and 2.5% at 0 and 1.5 s, respectively. Because we use current constraint method which is detailed in [16], both the phase and *q*-axis currents just jump to the safety level during acceleration. When the *q*-axis current reaches 60 A, the maximum output electromagnetic torque is about 25 Nm. Besides, the *d*-axis current fluctuates clearly at 1.5 s, which is caused by cross-coupling effect.

In terms deceleration, the settling time is also about 0.1 s and the speed overshoot is 6.5 rad/s (6.5%) at 2.5 s. In this process, the largest phase and *q*-axis currents are nearly -60 A and -25 Nm, which stands the opposite position with acceleration. Similarly, the *d*-axis current witnesses some fluctuations at 2.5 and 3.5 s.

When the load is imposed and removed on the motor, only a speed deviation of 2 rad/s appears, and the output electromagnetic torque quickly reaches expected level. This illustrates that the proposed multi-objective FCS-MPC algorithm is strongly robust to torque variation.

6.4.2 Experimental Results

The experimental equipment is shown in Fig.6-4. The system parameters are consistent with Table I as well. A common DC power supply is available at 310 V. Insulated gate bipolar transistor (IGBT) modules, FP25R12KT3, constitute the voltage inverter with the switching frequency of 10 kHz. The proposed SMO algorithm and the VC control algorithm are implemented on a DSP TMS320F28335 control board. The real rotor position can be detected by a rotary encoder. Hall current sensors, HIOKI 3275 Clamp On Probe, are used to measure the phase currents while the motor *d*, *q*-axis currents are calculated and recorded by the digital controller. An induction motor driven by an Automation Drive FC 301 with torque control mode, is coupled to the test machine, providing the required load torque.

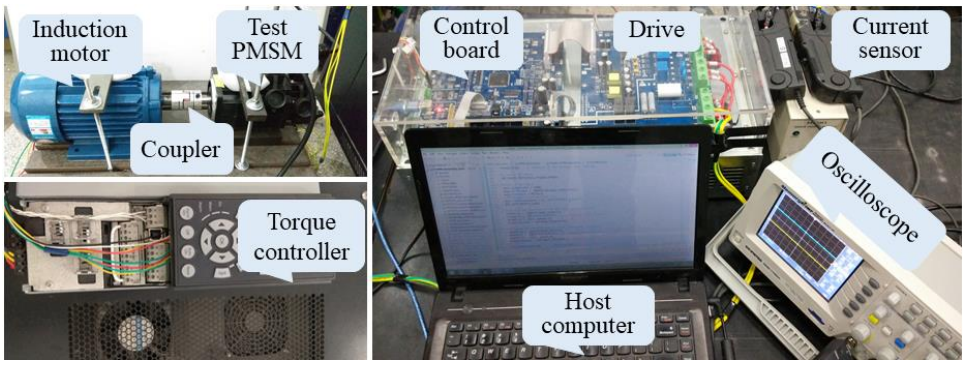

Fig. 6-4. Experimental equipment.

The experimental setup is as follows: the machine speed is set as 100 rad/s under no-load condition at first, after which it will maintain constant until 4.0 s when the rated load of 5 Nm is applied. From 6.0 s, the machine speed rises to 200 rad/s, while the motor decelerates at 10.0 s. At 12.0 s, the load is removed, and then the reference speed is set as 10 rad/s (ultra-low speed).

Similar to the simulation results, Fig.6-5 illustrates that the proposed method has good steady-state performance regardless of the machine speed and load conditions. Firstly, the machine speed can level off at the targeted values with small fluctuations (less than 2 rad/s) in the stable states. Then, the average value of the *d*-axis current is zero, and the *q*-axis current is slightly higher than zero under the no-load conditions, which is caused by the friction, while it levels off at nearly 12 A with small fluctuations under load cases. Thirdly, the output electromagnetic torque of the machine is consistent with the external load, indicating that the PMSM drive system can work normally under the rated load conditions. When it comes to the phase currents, they have shown symmetrical characteristics.

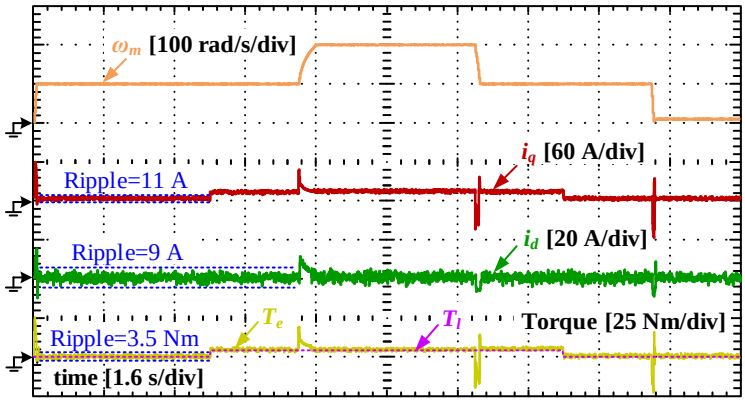

(a)

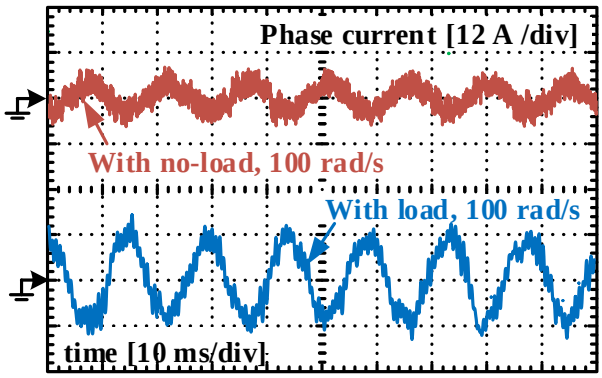

(b)

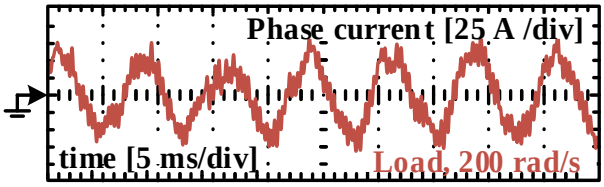

(c)

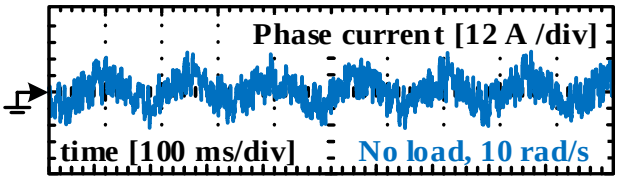

(d)

Fig. 6-5. Experimental performance of the proposed multi-objective FCS-MPC algorithm. (a) Speed, d-axis current, q-axis current and torque. (b) Phase currents under no-load and load conditions at 100 rad/s. (c) Phase current under load condition at 200rad/s. (d) Phase current under no-load condition at 10 rad/s.

As for the dynamics, different from the simulation results, it can be seen that the rise time over the low-speed range (0-100 rad/s) is about 0.1 s while it is about 0.3 s over the higher speed range. This happens because a relatively smaller *q*-axis current has been generated during acceleration from 100 to 200 rad/s in the experiment. But the deceleration characteristics show pretty similar trend to the simulation results. Interestingly, no speed overshoot is witnessed in Fig.6-5, and the machine speed can remain stable even if the load is suddenly imposed or removed. Finally, when the *q*-axis current reaches ±60 A in the transient process, the output electromagnetic torque increases to about ±24.5 Nm and the *d*-axis current shows visible

changes as well.

6.5 Summary

In this chapter, a simple multi-objective (speed and current) FCS-MPC strategy is proposed for the PMSMs used in EVs (regardless of EV types), achieving simple single-closed-loop control topology. Because the method is easy to implement and complies with the optimal control rules, it is obviously endowed with high reliability so as to improve the system safety. This topic is related to the system reliability and safety improvement in the normally running cases. Compared to the traditional single-objective FCS-MPC algorithms, both speed and current are included into the cost function of the proposed FCS-MPC controller as the TCOs. By doing this, the speed controller is no longer needed. When designing the algorithms, an improved PMSM model which contains not only differential but also integral equations is established. The experimental results illustrate that the proposed algorithm is effective.

6.6 References

[1] Z. Q. Zhu and Y. Liu, "Analysis of Air-Gap Field Modulation and Magnetic Gearing Effect in Fractional-Slot Concentrated-Winding Permanent-Magnet Synchronous Machines," in *IEEE Transactions on Industrial Electronics*, vol. 65, no. 5, pp. 3688-3698, May 2018.

[2] J. Lu, X. Zhang, Y. Hu, J. Liu, C. Gan and Z. Wang, "Independent Phase Current Reconstruction Strategy for IPMSM Sensorless Control Without Using Null Switching States," in *IEEE Transactions on Industrial Electronics*, vol. 65, no. 6, pp. 4492-4502, June 2018.

[3] C. Gong, Y. Hu, G. Chen, H. Wen, Z. Wang and K. Ni, "A DC-Bus Capacitor Discharge Strategy for PMSM Drive System with Large Inertia and Small System Safe Current in EVs," in *IEEE Transactions on Industrial Informatics*. doi: 10.1109/TII.2019.2895317

[4] A. D. Alexandrou, N. K. Adamopoulos and A. G. Kladas, "Development of a Constant Switching Frequency Deadbeat Predictive Control Technique for Field-Oriented Synchronous Permanent-Magnet Motor Drive," in *IEEE Transactions on Industrial Electronics*, vol. 63, no. 8, pp. 5167-5175, Aug. 2016.

[5] Y. Zhang and J. Zhu, "Direct Torque Control of Permanent Magnet Synchronous Motor With Reduced Torque Ripple and Commutation Frequency, " in *IEEE Transactions on Power Electronics*, vol. 26, no.

1, pp. 235-248, Jan. 2011.

[6] G. Wang, J. Qi, J. Xu, X. Zhang and D. Xu, “Antirollback Control for Gearless Elevator Traction Machines Adopting Offset-Free Model Predictive Control Strategy,” in *IEEE Transactions on Industrial Electronics*, vol. 62, no. 10, pp. 6194-6203, Oct. 2015.

[7] Y. Zhang, H. Yang and B. Xia, “Model-Predictive Control of Induction Motor Drives: Torque Control Versus Flux Control,” in *IEEE Transactions on Industry Applications*, vol. 52, no. 5, pp. 4050-4060, Sept.-Oct. 2016.

[8] M. Preindl and S. Bolognani, “Model Predictive Direct Torque Control With Finite Control Set for PMSM Drive Systems, Part 1: Maximum Torque Per Ampere Operation,” in *IEEE Transactions on Industrial Informatics*, vol. 9, no. 4, pp. 1912-1921, Nov. 2013.

[9] A. Mora, Á. Orellana, J. Juliet and R. Cárdenas, “Model Predictive Torque Control for Torque Ripple Compensation in Variable-Speed PMSMs,” in *IEEE Transactions on Industrial Electronics*, vol. 63, no. 7, pp. 4584-4592, July 2016.

[10] S. Kwak, U. Moon and J. Park, “Predictive-Control-Based Direct Power Control With an Adaptive Parameter Identification Technique for Improved AFE Performance,” in *IEEE Transactions on Power Electronics*, vol. 29, no. 11, pp. 6178-6187, Nov. 2014.

[11] E. Fuentes, C. A. Silva and R. M. Kennel, “MPC Implementation of a Quasi-Time-Optimal Speed Control for a PMSM Drive, With Inner Modulated-FS-MPC Torque Control,” in *IEEE Transactions on Industrial Electronics*, vol. 63, no. 6, pp. 3897-3905, June 2016.

[12] M. Yang, X. Lang, J. Long and D. Xu, “Flux Immunity Robust Predictive Current Control With Incremental Model and Extended State Observer for PMSM Drive,” in *IEEE Transactions on Power Electronics*, vol. 32, no. 12, pp. 9267-9279, Dec. 2017.

[13] Y. A. I. Mohamed and E. F. El-Saadany, “Robust High Bandwidth Discrete-Time Predictive Current Control with Predictive Internal Model—A Unified Approach for Voltage-Source PWM Converters,” in *IEEE Transactions on Power Electronics*, vol. 23, no. 1, pp. 126-136, Jan. 2008.

[14] X. Zhang, L. Zhang and Y. Zhang, “Model Predictive Current Control for PMSM Drives With Parameter Robustness Improvement,” in *IEEE Transactions on Power Electronics*, vol. 34, no. 2, pp. 1645-1657, Feb. 2019.

[15] W. Wang, Y. Fan, S. Chen and Q. Zhang, “Finite control set model predictive current control of a five-phase PMSM with virtual voltage vectors and adaptive control set,” in *CES Transactions on Electrical*

Machines and Systems, vol. 2, no. 1, pp. 136-141, March 2018.

[16] J. Liu, C. Gong, Z. Han and H. Yu, "IPMSM Model Predictive Control in Flux-Weakening Operation Using an Improved Algorithm," in *IEEE Transactions on Industrial Electronics*, vol. 65, no. 12, pp. 9378-9387, Dec. 2018.

[17] W. Xie et al., "Finite-Control-Set Model Predictive Torque Control With a Deadbeat Solution for PMSM Drives," in *IEEE Transactions on Industrial Electronics*, vol. 62, no. 9, pp. 5402-5410, Sept. 2015.

[18] F. Ban, G. Lian, J. Zhang, B. Chen and G. Gu, "Study on a Novel Predictive Torque Control Strategy Based on the Finite Control Set for PMSM," in *IEEE Transactions on Applied Superconductivity*, vol. 29, no. 2, pp. 1-6, March 2019, Art no. 3601206.

[19] Y. Yan, S. Wang, C. Xia, H. Wang and T. Shi, "Hybrid Control Set-Model Predictive Control for Field-Oriented Control of VSI-PMSM," in *IEEE Transactions on Energy Conversion*, vol. 31, no. 4, pp. 1622-1633, Dec. 2016.

[20] W. Tu, G. Luo, R. Zhang, Z. Chen and R. Kennel, "Finite-control-set model predictive current control for PMSM using grey prediction," *2016 IEEE Energy Conversion Congress and Exposition (ECCE)*, Milwaukee, WI, 2016, pp. 1-7.

[21] M. Preindl and S. Bolognani, "Model Predictive Direct Speed Control with Finite Control Set of PMSM Drive Systems," in *IEEE Transactions on Power Electronics*, vol. 28, no. 2, pp. 1007-1015, Feb. 2013.

[22] X. Zhang and B. Hou, "Double Vectors Model Predictive Torque Control Without Weighting Factor Based on Voltage Tracking Error," in *IEEE Transactions on Power Electronics*, vol. 33, no. 3, pp. 2368-2380, March 2018.

[23] J. Guzinski, H. Abu-Rub, M. Diguet, Z. Krzeminski and A. Lewicki, "Speed and Load Torque Observer Application in High-Speed Train Electric Drive," in *IEEE Transactions on Industrial Electroni*cs, vol. 57, no. 2, pp. 565-574, Feb. 2010.

[24] P. Cortes *et al*., "Guidelines for weighting factors design in Model Predictive Control of power converters and drives," *2009 IEEE International Conference on Industrial Technology*, Gippsland, VIC, 2009, pp. 1-7.

Chapter 7 **Conclusions and Future Work**

7.1 Summary

In this thesis, several EV safety improvement techniques have been introduced in detail. As an environmentally friendly transport option, EVs are endowed with the characteristics of low fossil energy consumption, pollutant emissions as well as lower cost, making them a promising substitute for the conventional gasoline vehicles. There are hundreds of scholars and engineers investigating the EV-related technologies worldwide to improve the qualities of vehicles. Unluckily, there is still a long way to go before the EV technologies become totally mature, especially the fatal safety issues that most of the ordinary people worry about. The recently emerged crash and battery fire cases have hindered the promotion of EVs. On this ground it is very crucial to study the safety improvement techniques at present. Actually, the particular EV risks that are different from the traditional gasoline vehicles mainly come from its high-voltage and high-power powertrain. Therefore, this research mainly focuses on the problems arising from different types of EV powertrains. Firstly, in order to explain the reasons why the EV safety problems come from their powertrain systems, a comprehensive review on EV classifications and powertrain components is done. This illustrates that in spite of the EV types, the powertrain components usually operate under the high-voltage and high-power situations, posing potential electrical threats to the occupants. Besides, according to the UN regulations, the EV safety considerations should be demonstrated at length, which will provide guidelines for the relevant researches and help the ordinary people have a better understanding of EV safety issues. Then, DC-DC converters are necessary for some EV models when the voltage in the powertrain must be transferred from one level to another. Traditionally, the unidirectional and bidirectional converters are adopted in most of the existing vehicle models. But for HEVs, if these two kinds of converters are used, there should be at least two sets of them, sacrificing the volume and cost of the powertrain. Simultaneously, the system reliability will get reduced due to the use of more power electronic devices. Hence, this research designs a tri-port converter to combine the generator, battery bank and motor in one converter to improve the safety and reliability of the SRM-based HEVs by reducing the use of power electronics and

endowing it with fault-tolerance capability. In terms of the PMSM based BEVs, this research introduces two seldom considered safety problems, one of which (UCG) arises in the post-fault condition and the other (DC-bus voltage discharge) is in the post-crash condition. Aiming at these two problems, specially designed solutions are proposed in this research, which contributes to enhance the safety of both the powertrain components and the occupants. Finally, a traction motor is the heart of an EV powertrain, the system reliability level as well as the performance is closely related to the machine control algorithms. Considering that the traditional methods are usually complicated, the software reliability will degrade the hardware safety. Therefore, the new control algorithms with simple structure and complying with the optimal control rule are highly demanded in practice. This research proposes a multi-objective FCS-MPC controller for the PMSMs used in EVs (regardless of the EV types), achieving simpler single-closed-loop control topology so as to improve the system reliability.

In Chapter 2, an in-depth literature review has been presented introducing the EV categories, components constituting the powertrains and the safety problems considering the regulatory activities. This research categorizes the EVs into three types, namely, BEV, HEV and PHEV according to their structures and features. Regardless of EV types, the basic powertrain of them are comprised of battery, DC-DC converter, DC-bus capacitor, inverter and traction motor. Because these equipment have to work under the high-voltage and high-power conditions, the electrical safety problems of EVs deserve much more attentions. Finally, from a professional perspective, the EV safety is discussed according to the UN Regulations. The work in this chapter indicates that firstly, there are dozens of EV models based on different components, and each of them deserves further investigation. Secondly, it is of great value to provide guidelines for the future researches about EV safety improvement techniques following the international standards.

Chapter 3 presents the novel tri-port DC-DC converters used for SRM based HEVs. Compared to the traditional unidirectional and bidirectional converters, this kind of converter requires less power electronics to achieve complicated energy conversion functions in the powertrain and it is easy for the converter to achieve fault-tolerance operations. Consequently, the tri-port converter is highly reliable. In this chapter, the structure of the converter is introduced firstly. Then, the six working modes of the tri-port converter are explained in detail, and aiming at the different working modes, the corresponding control strategies are developed. Finally, the fault-

tolerance ability of the converter is demonstrated. Both the simulation and experiments have been carried out to verify the functions of the proposed tri-port converter. Honestly, this technology proposed for HEVs can be applied to the other applications, such as airplanes and more-electric ships, in which high reliability and safety, high density and flexible energy flow are required.

Chapter 4 introduces the UCG problems for the PMSM based BEVs in the post-fault conditions. This problem is seldom discussed previously but closely related to the health of the electrical components in the powertrains and system safety. When the traction motor is driven by the flux weakening algorithms to operate in the high0speed situations, the faults might happen inevitably, triggering the system protection mode. In this case, the traction motor will serve as a generator, charging the battery. However, the charge current is inclined to be large due to the small battery resistance. Considering this problem, this chapter firstly establishes a UCG model for the PMSM based EV powertrain systems. Secondly, the parameter dependencies of the UCG phenomenon are analyzed. It needs to be mentioned that instead of just considering the saliency ratio in the previous studies, this chapter also takes the motor inductance, phase resistance, magnetic flux and battery internal resistance into account, and a crucial conclusion that the proper *d*-axis inductance is contributive to the charge current suppression in the UCG situations is drawn. On this ground an IPMSM design and optimization strategy that can suppress the UCG phenomenon is demonstrated. By using this precaution scheme, the recharge current in the post-fault conditions can maintain at the safe level so as to protect the powertrain equipment and enhance the system safety.

Chapter 5 presents a reliable winding-based DC-bus capacitor discharge strategy for PMSM based BEVs. When an EV encounters a pitiful crash, the occupants will suffer from the primary injury such as bump and extruding, but they do not get out danger completely. As suggested in Chapter 2, the electric shock risks become more severe in crash, one of which arises from the residual energy in the machines and DC-bus capacitor. In order to dissipate the residual energy and prevent the occupants and even the rescuers from electric shock, effective and efficient energy discharge measures need to be adopted. Usually, an external bleeding circuit composed of a power resistor and a switch is employed to expend the residual energy, but the use of extra circuits increases the weight and cost but decreases the system reliability. Therefore, the proposed winding-based discharge strategy emerges. The proposed technique aims to avoid

electric shock in the post-crash cases by quickly and safely discharge the residual energy by directly using the machine windings rather than the external circuits. However, this method is achieved relying on accurate position information of the traction motor. Considering that the position transmission lines between the motor and controller might get broken in the crash, a position sensor fault-tolerant strategy based on SM observer is developed to endow the proposed discharge strategy with high fault tolerance ability. According to the simulation and experimental results, the proposed winding-based discharge strategy is able to get the DC-bus voltage down to the safe level within 5 seconds, complying with the UN regulations.

Chapter 6 presents a reliable multi-objective FCS-MPC strategy that combines speed and current control into one single controller for the PMSMs used in EVs (regardless of EV types). This method can achieve high control performance by using the simpler single-closed-loop control topology and the optimal control rules. Thanks to these inherent advantages, the proposed controller is endowed with high reliability and safety. This topic is studied to improve the system reliability and safety level in the normally running cases. In terms of the implementation of the proposed method, both the speed and current are included into one cost function firstly. By doing this, the speed controller is no longer needed. The experimental results illustrate that the new control method is effective. This research complies with the system reliability and safety improvement in the normally running cases, providing guidelines for designing simple control software.

7.2 Future Work

Based on the conclusions above and considering the limitations of the work existed, future research could be carried out in the following areas.

- **Further investigation for more safety problems in different EVs**

  It has been shown in Chapter 2 that there are different types of EVs running on the road and each of them might have different powertrain structure and components. Usually, each system has very specific safety problems and all of them deserves in-depth investigation. Certainly, some potential safety issues have been perfectly solved by the existing techniques. Whereas, there are still hundreds of unsolved problems or even

undiscovered ones. in detail, this research only carries out researches in the areas of highly-reliability converter, UCG, bus voltage discharge and reliable control issues, but for the sake of comprehensive study and as a qualified scholar, more EV safety problems require to be considered, which will greatly improve the safety level of different EVs. Only by making the EV systems more secure and reliable will the applications of them get promoted in the future.

- **High-performance tri-port converter for PMSM based HEVs**

  In this thesis, the tri-port converter is proposed only for the SRM-base HEV. But as suggested, this kind of converter has many advantages, such as avoiding the use of power electronics, achieving six working modes and having high fault tolerance capability, and so on, so it needs to be applied to other kinds of systems. In Chapter 2, it is illustrated that the most commonly used EV systems are based on PMSMs. Hence, I will investigate the tri-port converter for PMSM based HEVs in the near future. Because the connection patterns of the PMSM windings might be different from those of SRM in Chapter 3, the structure and control strategies need to be redesigned completely. Moreover, because the tri-port converter is a new technology for EVs, the performance and topology of it require to be elaborated from all aspects. In other words, instead of focusing on the multi-functions, the better performance required to be studied in the near future.

- **Novel UCG attenuation strategies**

  Chapter 4 illustrates that the proposed UCG suppression approach based on the *d*-axis inductance optimization is achieved by changing the PMSM rotor structure. This is only available at the motor design process, which happens at the very beginning of the EV powertrain design. But there are many fixed PMSM based BEVs running on the road nowadays. It is nearly impossible to redesign the motors for those vehicles and replace them with the new ones. Consequently, the brand-new UCG attenuation strategies for the existing EV models will be discussed in the future. In my mind, there are two candidate schemes. Firstly, a power resistor in series with a diode together with a paralleled switch can be used for reducing the charge current. Secondly, an extra controllable switch can be employed to reduce the average charge voltage and current

by using PWM algorithms. Obviously, these strategies aim to reduce the system current in the post-fault conditions rather than completely eliminate the UCG phenomenon in comparison with the *d*-axis inductance optimization method, but they are effective for the already-existed BEVs.

- **Hybrid DC-bus voltage discharge approach combining the machine windings and external circuits**

  In Chapter 5, the simulation and experimental results show that the discharge time is about 3 s, which complies with the UN regulations. But it deserves to be mentioned that parameters of the test system are not extreme, which means that the rotor inertia and maximum working speed of the machine are not large. It can be imagined that once the initial machine speed at the moment when an active discharge is requested is higher or the rotor inertia is larger, the discharge time will get longer (possibly exceeding 5 s). Consequently, the parameter dependencies of the proposed winding-based discharge method should be investigated in the near future. Moreover, regarding to the EV powertrains of which parameters are not suitable for the proposed winding-based discharge method, a hybrid DC-bus discharge approach combining the machine windings and the traditional external circuits, which has larger discharge capacity, needs to be developed in the near future. Meanwhile, the corresponding discharge algorithms will be designed as well.

- **Reliability improvement for MPSC method**

  Although the proposed MPSC method in Chapter 6 can achieve high control performance, it is only effective without any parameter mismatch problems or faults. But because the MPSC is a model-based strategy, when the parameter values used for prediction do not comply with the real ones, the control performance will be degraded greatly. Moreover, once the inevitable faults such as position sensor faults and current sensor faults occur, the MPSC control algorithm will totally malfunction. Considering these problems, the parameter identification, disturbance compensation and corresponding fault-tolerant control techniques should be incorporated into the MPSC controller to improve its reliability and further the safety of EV powertrains.

END